Coupling of Nanomechanical Resonators to Controllable Quantum Systems
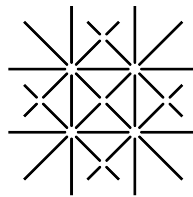
Inauguraldissertation

zur

Erlangung der Würde eines Doktors der Philosophie

vorgelegt der

Philosophisch-Naturwissenschaftlichen Fakultät
der Universität Basel

von

Michele Montinaro

aus Calimera (LE), Italien

UNI
BASEL

Basel, 2014

Genehmigt von der Philosophisch-Naturwissenschaftlichen Fakultät
auf Antrag von

Prof. Dr. Martino Poggio

Dr. Heike Riel

Basel, den 16.9.2014   Prof. Dr. Jörg Schibler
                                                            Dekan

"Kalí nifta! Se finno ce pao;
plaja 'su ti 'vo pirta prikó
ce pu pao, pu sirno, pu steo
'sti kkardía-mu panta sena vastó."

Matinata, V. D. Palumbo
(Calimera, 1854 – 1918)

Contents

Nomenclature

List of Symbols

Symbols used in this dissertation are reported in order of appearance. Those marked in bold fonts represent vectors, those written with multiple indexes (i.e. ε_{ij}) represent tensors (second rank or higher).

Symbol	Units	Description
$\boldsymbol{U}(\boldsymbol{r},\,t)$	m	Displacement function of a resonator
n	–	Index of the vibrational mode
$x_n(t)$	m	Time-dependent displacement function
$\boldsymbol{u}_n(\boldsymbol{r})$	–	Mode shape function
m	kg	Effective mass of a resonator
Γ_n	kg s^{-1}	Intrinsic dissipation
k_n	N m^{-1}	Spring constant
ω_n	Hz	Angular resonance frequency
Q_n	–	Quality factor
$\hat{x}$	–	Direction unit vector
E_Y	Pa	Young's modulus of the material
I_y	m^4	Polar moment of inertia about $\hat{y}$
ρ	kg m^{-3}	Density of the material
A	m^2	Cross-sectional area of a beam
L	m	Length of a beam
x_osc	m	Displacement amplitude
x_rms	m	Root-mean-squared displacement
β_n	–	Parameter characterizing the motion of a resonator
w	m	Width of a beam with rectang. cross-sect.
d	m	Thickness of a beam with rectang. cross-sect.
D	m	Diameter of a cylindrical beam
s	m	Side of a beam with hexagonal cross-sect.
U_pot	J	Potential energy
$\boldsymbol{r}$	–	Generic position vector

V	m^3	Volume
M	kg	Mass
ε_{ij}	–	Strain tensor
$\boldsymbol{F}_i$	N	Force acting on the face i of a cubic element
$\boldsymbol{n}$	–	Normal unit vector
σ_{ij}	Pa	Stress tensor
α_{ijkl}	Pa	Elasticity tensor
ν	–	Poisson's ratio
C_{ijkl}	Pa^{-1}	Compliance tensor
σ_z	Pa	Uniaxial stress along $\hat{z}$
ξ	m	In the cross-sect. of a beam, distance from the center along $\hat{x}$
$\varepsilon_\perp$	–	Strain component in the plane perpendicular to the uniaxial stress direction
$\varepsilon_\parallel$	–	Strain component parallel to the uniaxial stress direction
$\varepsilon_{ij}^{\mathrm{iso}}$	–	Isotropic component of the strain
$\varepsilon_{ij}^{\mathrm{dev}}$	–	Deviatoric component of the strain
η	–	Strain parameter
F_{th}	N	Random thermal force
$\hat{x}_\tau(\omega)$	m Hz$^{-1/2}$	Fourier transform of $x(t)$ over a time τ
$\bar{S}_x(\omega)$	m^2 Hz^{-1}	Spectral density of a signal $x(t)$
$K_x(t)$	m^2	Autocorrelation function of a signal $x(t)$
$S_x(\omega)$	m^2 Hz^{-1}	Single-sided spectral density of a signal $x(t)$
k_{B}	J K^{-1}	Boltzmann's constant
T	K	Temperature of the environment
$S_{x_{\mathrm{n}}}, S_{\xi_{\mathrm{n}}}$	m^2 Hz^{-1}	White noise spectral density
α	V m^{-1}	Transduction coefficient
p	bar	Pressure
T_{eff}	K	Effective temperature of the resonator
E_N	J	Eigenenergy
$\hbar = h/2\pi$	J s	Plank's constant
N	–	Mode occupation number
x_{zpf}	m	Root-mean-squared zero-point fluctuations
$\hat{H}$	J	Hamiltonian operator
$\hat{K}$	J	Kinetic energy operator
$\hat{U}$	J	Potential energy operator
N_{th}	–	Average thermal occupation number
S_x^{zpf}	m^2 Hz^{-1}	Spectral density of the zero-point fluctuations
Δx	m	Standard deviation on the position
Δp	kg m s^{-1}	Standard deviation on the momentum
S_x^{imp}	m^2 Hz^{-1}	Quantum limited measurement sensitivity

S_x^{ba}	$\mathrm{m^2\,Hz^{-1}}$	Spectral density of the back-action force noise
S_x^{SQL}	$\mathrm{m^2\,Hz^{-1}}$	Imprecision at the standard quantum limit
R_1	–	Reflectivity of the cleave-air interface
R_2	–	Reflectivity of the cantilever-air interface
E_i	$\mathrm{N\,m^{-1}}$	Module of the incident electric field
l	m	Cavity length
λ	m	Laser wavelength
ϕ_1	–	Phase shift acquired by the light reflected from the fiber's cleaved facet
ϕ_2	–	Phase shift acquired by the light reflected from the cantilever
P_r	W	Interferometer output power
P_{max}	W	Maximum interferometer output power
P_{min}	W	Minimum interferometer output power
P_{amp}	W	Amplitude of the interferometer output power
P_{avg}	W	Average interferometer output power
$\bar{V}$	–	Visibility of the interferometer
n_{r}	–	Refraction index
S	$\mathrm{A\,W^{-1}}$	Responsivity
I_{shot}	A	Average shot noise current
e	C	Electron charge
$\Delta\nu$	Hz	Detection bandwidth
x_{noise}	m	Equivalent noise displacement
l_ϕ	m	Coherence length
l_e	m	Mean free path
λ_{F}	m	Fermi wavelength
m^*	kg	Electron effective mass
V_0	V	Electrostatic potential
ζ_0	$\mathrm{s^{-1}\,C^{-1/2}}$	Strength of the lateral confinement in a QPC
k_x	$\mathrm{m^{-1}}$	Wave number along x
V_{sd}	V	Source-drain potential
V_{G}	V	Gate potential
$\mu_{\mathrm{s}}, \mu_{\mathrm{d}}$	J	Chemical potentials of source and drain, resp.
v_N	$\mathrm{m\,s^{-1}}$	Group velocity
ρ_N	$\mathrm{(J\,m)^{-1}}$	Density of states
I	A	Electrical current
G	S	Conductance
G_0	S	Quantum of conductance
R_{b}	Ω	Total background resistance in a QPC
T_{mode}	K	Mode effective temperature of the resonator
V_{L}	V	Cantilever potential
g	–	Feedback gain coefficient

x_n, ξ_n	m	Measurement noise on a displacement signal
$\delta(t)$	–	Dirac distribution in the time domain
B	T	Magnetic field
E_C	eV	Charging energy of a confined electron system
C_Σ	F	Self-capacitance of a confined electron system
C_G	F	Capacitance between finger gates and QD
α_G	–	Lever arm of the finger gates
ε_r	F m^{-1}	Dielectric constant of InAs
ε_0	F m^{-1}	Dielectric constant of vacuum
A_osc	m	Positioning stage driven oscillation amplitude
V_PZT	V	PZT excitation amplitude
$|g\rangle$	–	Ground state of a quantum two-level system
$|e\rangle$	–	Excited state of a quantum two-level system
E_ex	eV	Transition energy of a QD exciton
$\hat{\sigma}_z$	–	Pauli operator of a quantum two-level system
n_0	s^{-1}	Intrinsic QD photon counts per unit time
n_d	s^{-1}	QD photon counts with mechanical drive
$\hbar\Gamma$	eV	Intrinsic QD emission linewidth (FWHM)
a	eV	Isotropic deformation potential
d	eV	Deviatoric deformation potential induced by a stress along $\langle 1\,1\,1\rangle$
$\Delta E^\mathrm{C\text{-}HH}$	eV	Energy gap variation between conduction and heavy-hole bands
λ	Hz	Opto-mechanical coupling rate
τ_ex	s	Lifetime of a quantum transition
γ_ex	Hz	Decoherence rate of a quantum transition
Γ_th	Hz	Mechanical heating rate

List of Acronyms

Acronym	Description
QPC	Quantum point contact
FEM	Finite element model
NW	Nanowire
SEM	Scanning electron microscopy
SNR	Signal-to-noise ratio
zpf	Zero-point fluctuations
SQL	Standard quantum limit

MRFM	Magnetic resonance force microscopy
PD	Photodetector
TEC	Thermoelectric cooler
PZT	Piezoelectric transducer
PID	Proportional-integral-derivative controller
FSR	Free spectral range
SET	Single electron transistor
QD	Quantum dot
SGM	Scanning gate microscopy
SQUID	Superconducting quantum interference device
2DEG	Two-dimensional electron gas
MBE	Molecular-beam epitaxy
UVL	Ultra violet lithography
EBL	Electron-beam lithography
FPGA	Field programmable gate array
AFM	Atomic force microscopy
SET	Single-electron transistor
CPD	Critical-point drying
NV	Nitrogen vacancy
NA	Numerical aperture
CCD	Charge-coupled device
FWHM	Full width at half maximum
AOM	Acousto-optic modulator
QND	Quantum non-demolition
QED	Quantum electrodynamics

Introduction

Since the introduction of atomic force microscopy [1], nanomechanical resonators constitute a key component in a wide variety of today's most sensitive experiments. Devices have been proved as ultra-sensitive force probes, able to detect the tiny Casimir interaction arising from the zero-point fluctuations of the electromagnetic vacuum [2], or capable of sensing the magnetic force associated with an individual electron spin [3]. Using a single electron transistor made of a suspended carbon nanotube, scientists were able to detect small changes in the nanotube resonator mass with a resolution down to the single proton level [4]. At the same pace with these achievements, researchers have developed transducers of mechanical motion with resolution approaching the standard quantum limit on position detection [5,6], i.e. the limit set by quantum mechanics to the precision of continuously measuring position [7]. Such exquisite resolution has implications in several precision measurements, including investigation of deviations from Newtonian gravity at short distances [8], or gravitational wave sensing [9]. Moreover, exploring the quantum limit of displacement detection opens up appealing scenarios for the investigation of quantum behavior in mechanical systems as well as for testing the macroscopic manifestation of quantum mechanics itself [10].

Whereas quantum mechanics provides a highly accurate description of a variety of phenomena concerning microscopic systems, its application to macroscopic mechanical objects is still subject of theoretical discussion and inspiration for challenging experiments [11]. Only in the last four years did scientists manage to observe quantum effects in engineered mechanical structures. It is now feasible both to initialize the fundamental vibrational mode of a mechanical resonator into its ground state [12–14] and even to produce non-classical coherent states of motion [15]. The significance of these results lays in the achieved coupling between a mechanical resonator and a controllable quantum system (Fig. 1). Besides reaching quantum control over mechanical motion, a current major challenge is, conversely, to employ mechanical vibrations for probing quantum states, also in a quantum non-demolition scheme [16,17].

Progress in nanotechnology allows the fabrication of mechanical resonators functionalized with electrodes, magnets, or mirrors, thus transforming
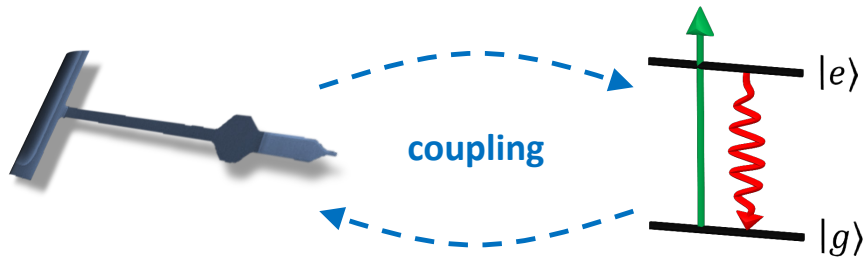
Figure 1 | **Quantum hybrid system.** A nanomechanical resonator is coupled to a controllable quantum system.

motion into the modulation of electric, magnetic, or optical fields [18]. The ease of this process has inspired proposals to use nano-resonators for quantum information processing and networking. The resonator can in fact encode quantum information into a mechanical state and act as a quantum transducer, mediating interactions between different quantum systems [19–22]. Following this route, scientists have demonstrated the coupling of mechanical resonators to a variety of quantum systems, including optical [14] and microwave [23] cavities, superconducting devices [24], laser-cooled atoms [25], quantum dots [26,27], and nitrogen vacancy centers in diamond [28–30].

Quantum control over these coupled quantum systems, or *hybrid* systems, requires the coupling strength to be large compared to the rates at which the coupled systems decohere into their local environments [31]. In addition, for quantum effects to be observable, strong coupling has to be accompanied by the initialization of the resonator into a state of minimum entropy. This is achieved by cooling the resonator close to its quantum ground state of motion, either by cryogenic refrigeration [15] or with the aid of specifically designed cooling techniques [12,32].

With this dissertation, we aim at contributing to the captivating field of hybrid systems from different directions. First, we demonstrate the use of an innovative quantum transducer – a quantum point contact (QPC) – to measure and control the low-temperature thermal motion of a nearby micromechanical cantilever [33]. The QPC is included in an active feedback loop designed to cool the cantilever's fundamental mechanical mode down to the level of the measurement noise. Our system represents the first application of a mesoscopic transducer, such as a QPC, to control and cool by feedback an off-board mechanical resonator and as such serves as an important demonstration experiment. Advantages of our approach include versatility to force-sensing applications, due to the off-board design, applicability to nanoscale oscillators, and the potential to achieve quantum-limited detection and cooling to the ground state of motion.

We further explore the field of nano-electromechanical systems by showing the coupling of an ultra-soft cantilever to a QPC realized via local oxidation lithography, in an ongoing attempt to improve its sensitivity to cantilever motion. In addition, we realize innovative field effect transistors made of nanowires suspended above local electrostatic gates. We show the confinement of quantized electron charge within a nanowire, in an approach aimed at studying the coupling of this charge to the mechanical vibrations of the nanowire itself or to the motion of an off-board cantilever. The electron transport in the nanowire can be localized far closer to the cantilever motion than can the sub-surface transport through a QPC, reasonably resulting in a better transduction efficiency.

Thereafter, we demonstrate a promising hybrid system made of fully self-assembled core-shell nanowire cantilevers embedding optically active quantum dots. The system reveals an unusually strong coupling between the nanowire mechanical vibrations and the quantum dot light emission [34]. Such an opto-mechanical coupling mechanism resides in the oscillation-induced material strain, therefore constituting the experimental implementation after 10 years of the theoretical proposal of Wilson-Rae *et al.* [35]. The relevance of our demonstration is testified by the very recent ferment in the scientific community about strain-mediated coupling in hybrid systems [27, 29, 30]. In particular, the first experiment of this kind by Yeo and coworkers [27], nearly contemporaneous to ours, exploits a different material system to investigate similar physics and obtain a coupling strength comparable to ours. Unlike Yeo *et al.*, we take advantage of the recent developments in the bottom-up growth of radially heterostructured nanowires, which allow for band-structure engineering and positioning of quantum dots within a nanowire structure [36]. As a result, we achieve the first realization of an *as-grown* hybrid system in which multiple quantum systems are coupled to a unique, monolithic mechanical structure. By controlling the nanowire oscillations, we are able to tune the quantum dot emission energies over a broad range exceeding 14 meV. The latter two results pave the way to mechanically induced coupling between different quantum dots within the nanowire.

The recurring theme of the research approaches pursued in this thesis is the preference for systems in which the coupling between the mechanical structure and the quantum partner occurs naturally, without the need for any sophisticated engineering. In fact, the QPC displacement transducer is sensitive to local modifications of the nearby electric field. Since any resonator placed in proximity to the QPC disturbs its potential landscape, not any particular functionalization is required to activate the capacitive coupling. Furthermore, in case of the quantum-dots-in-nanowire structure, its *built-in* nature produces a hybrid system whose inherent coherence is unspoiled by external functionalization. Most other hybrid systems, instead,

require the application to the mechanical resonators of coupling elements or external fields, which tend to compete with the small resonator mass and high quality factor necessary to achieve low thermal noise and high coupling strength [37]. Moreover, the functionalization process often adds additional paths of dissipation and decoherence, reducing the lifetime of the coupled quantum system.

Thesis Outline

The thesis is structured as follows.
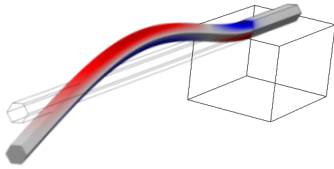
Chapter 1 provides a concise theoretical background of the field of Nanomechanics. Starting from the basic concepts of Euler-Bernoulli beam theory, it illustrates in detail specific cases of interest for this thesis, both analytically and through finite element simulations. It concludes by providing the analytical tools for describing the thermal motion of a mechanical resonator and by considering the quantum effects emerging on it at low temperatures.
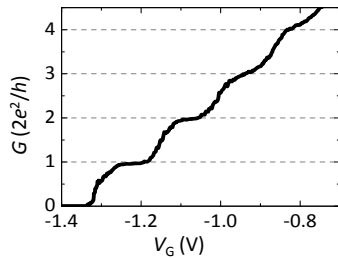
Chapter 2 introduces the experimental techniques used in this thesis to detect the displacement of micro- and nanomechanical resonators and gives an overview of the state of the art of the other main approaches. In particular, it illustrates the physics underlying the working principles of a QPC.
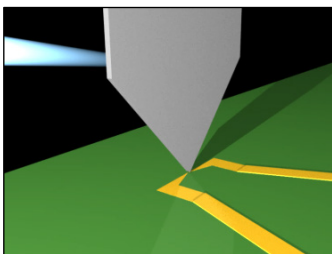
Chapter 3 is devoted to describing the operation of a split-gate QPC fabricated during the work of this thesis. It discusses its performance as a displacement transducer and as a means for damping the motion of a nearby cantilever through active feedback. It also provides a brief description of the other cooling techniques currently in use and an outlook on future improvements of our cantilever-QPC system.
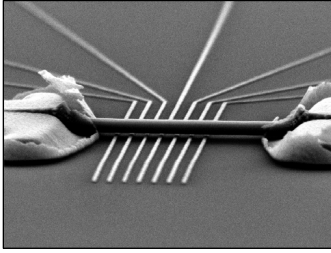
Chapter 4 describes some ongoing efforts to improve the coupling between a cantilever and mesoscopic displacement transducers. In particular, it reports on measurements with a QPC defined via local oxidation lithography and describes an innovative electromechanical system made of a suspended-nanowire single-electron transistor.
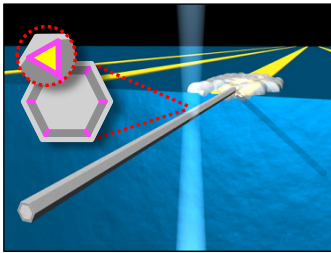
Chapter 5 reports on the demonstration of a novel hybrid system made of optically active quantum dots embedded in fully self-assembled core-shell nanowires. It shows the experimental evidence of an opto-mechanical coupling, the characterization of its strength, and the elaboration of a model to describe its mechanism. The chapter concludes by enlarging the view on several promising prospective studies and applications employing this system.

Chapter 6 provides a conclusion to the thesis, by summarizing its motivation and main results and giving an outlook on the challenges which the reported experiments open on future research.

1 | Nanomechanics

This chapter gives an overview of the fundamental concepts underlying the study of nanomechanical resonators. After providing an analytical model of beam vibrations, we describe in detail two cases of interest for this thesis: the singly and the doubly clamped beam. We introduce the fundamental concept of effective mass of a resonator and present the study of the deformations of a resonator subject to an external load, with particular attention to the case of flexural vibrations. Thereafter, we analyze the motion and deformation of the structures studied in this thesis via finite element calculations. The chapter concludes by introducing the concepts of thermal and quantum noise, and illustrating the limitations imposed by quantum mechanics on the resonator's displacement detection.

1.1 Motion of a Resonator

The motion of a mechanical resonator under an external load is well described by the Euler-Bernoulli theory of beams [38]. Entirely developed by mathematicians from Basel, the theory relies on the early work of Jacob Bernoulli and was later consistently formulated by Leonhard Euler and Daniel Bernoulli around the year 1750 [39]. It covers the case of small deflections of a beam that is subject to lateral loads only. It results most accurate for beams whose cross-section is much smaller than the length [40]. This is typically the case of the nano-sized resonators used in current experiments, due to the general requirements of a low spring constant and a high quality factor.

Within the frame of Euler-Bernoulli beam theory, the complete, three-dimensional motion of a resonator is described by a displacement function $\boldsymbol{U}(\boldsymbol{r}, t)$ which depends on direction ($\boldsymbol{r}$) and time (t) and accounts for an infinite number of independent vibrational modes. Indicating each mode with an index n, the direction and time dependence of the displacement function can be separated as follows:

$$\boldsymbol{U}(\boldsymbol{r}, t) = \sum_n x_n(t)\, \boldsymbol{u}_n(\boldsymbol{r}), \tag{1.1}$$

where $x_n(t)$ is a function describing the time dependence of the motion and $\boldsymbol{u}_n(\boldsymbol{r})$ is the mode shape of the n-th mode. In the following, we adopt the choice described in Ref. [41] to normalize $\boldsymbol{u}_n(\boldsymbol{r})$ so that the maximum value of $|\boldsymbol{u}_n(\boldsymbol{r})|$ is unity. This choice of normalization ensures that $x_n(t)$ has units of distance and is directly related to the resonator's displacement measured experimentally. However, it should be noted that such a normalization breaks the orthonormality between the modes.

In the case of high quality factor resonators, the function $x_n(t)$ can be determined by approximating each of the independent vibrational modes as a damped harmonic oscillator [18,40], whose equation of motion is the following (see Section 1.6):

$$m_n \ddot{x}_n + \Gamma_n \dot{x}_n + k_n x = 0. \tag{1.2}$$

Here m_n, Γ_n and k_n are the effective mass, intrinsic dissipation, and spring constant for the n-th mode of the resonator. The dissipation and the spring constant can be written in terms of the effective mass, the angular resonance frequency ω_n and the quality factor Q_n according to $\Gamma_n = m_n \omega_n / Q_n$ and $k_n = m_n \omega_n^2$. A general expression for m_n and its determination for some cases of interest for this thesis are provided in Section 1.3.

The mode shape function $\boldsymbol{u}_n(\boldsymbol{r})$ can be determined analytically for many simple models of practical interest. In the next section, we analyze the case of a beam subject to a time-varying transverse load, giving rise to *flexural vibrations*. When the resonator's geometry or its boundary conditions are more complicated, the analysis requires a finite element model (FEM) of the structure. In Section 1.5 three such models are described, providing a comparison to the simpler analytical cases.

1.2 Analytical Theory of Beams

Many nanomechanical resonators possess beam-like geometries and their motion, generally expressed through Eq. (1.1), can be reduced to a one-dimensional displacement function:

$$U(z,\,t) = \sum_n x_n(t)\, u_n(z), \tag{1.3}$$

where the one-dimensional mode shape $u_n(z)$ as a function of the position along $\hat{z}$ is normalized, as before, so that the maximum value of $|u_n(z)|$ is unity.

We study in the following the case of a long thin beam of uniform cross-section, subject to flexural vibrations in one dimension. It is not necessary, for the moment, to make the form of the driving load explicit. A coordinate system is defined as in Fig. 1.1, the beam length is L and the oscillation
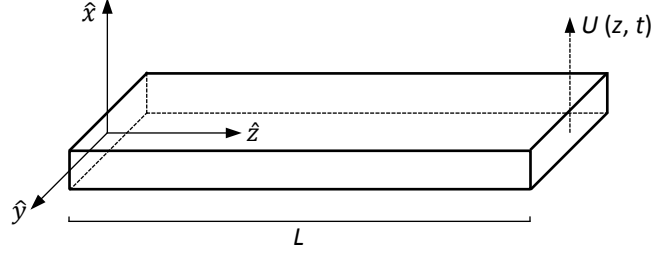
Figure 1.1 | **Reference system for the beam.** A beam of length L is oriented along the $\hat{z}$ axis and displaces along $\hat{x}$. The beam's cross-section is uniform throughout the length and its size, as well as the displacement's amplitude, are much smaller than L.

direction is along $\hat{x}$. Within this frame, the equation of motion can be written as follows [40]:

$$E_{\mathrm{Y}}I_y\frac{\partial^4 U}{\partial z^4} + \rho A\frac{\partial^2 U}{\partial t^2} = 0. \tag{1.4}$$

Here E_{Y} is the Young's modulus of the material, I_y is the polar moment of inertia about $\hat{y}$, ρ is the density, and A is the cross-sectional area of the beam. From the expression of $U(z, t)$ given in Eq. (1.3), it derives that Eq. (1.4) can be solved separately for each of the resonator's n modes. The time dependence of the motion is expressed only through the function $x_n(t)$, governed by the Eq. (1.2). For high-Q resonators, the damping term $\Gamma_n \dot{x}_n$ can be for the moment neglected, letting $x_n(t)$ assume an oscillatory behavior of the kind:

$$x_n(t) = x_{\mathrm{osc},n}\,\mathrm{e}^{-\mathrm{i}\omega_n t}, \tag{1.5}$$

where $x_{\mathrm{osc},n}$ is the oscillation amplitude. Therefore, the n-th mode shape function of the resonator must satisfy:

$$\frac{\mathrm{d}^4 u_n}{\mathrm{d}z^4} - \frac{\beta_n^4}{L^4}\,u_n = 0, \tag{1.6}$$

where $\beta_n = L\left(\rho A\omega_n^2/(E_{\mathrm{Y}}I_y)\right)^{1/4}$ is a dimensionless parameter. This differential equation has the general solution:

$$u_n(z) = A_n \sin\frac{\beta_n}{L}z + B_n \cos\frac{\beta_n}{L}z + C_n \sinh\frac{\beta_n}{L}z + D_n \cosh\frac{\beta_n}{L}z. \tag{1.7}$$

The values of the mode-dependent parameters β_n, A_n, B_n, C_n, and D_n are determined (up to a normalization constant) by setting the boundary conditions for the specific physical problem. Together with the determination of the mode shape of each of the beam's n modes, it is also possible to calculate the corresponding eigenfrequency, using the relation

$$\omega_n = \frac{\beta_n^2}{L^2}\sqrt{\frac{E_{\mathrm{Y}}I_y}{\rho A}}. \tag{1.8}$$

Mode	β_n	ω_n/ω_0
0	1.875	1.000
1	4.694	6.267
2	7.855	17.547
3	10.996	34.386
$n \geq 3$	$(n + 1/2)\pi$	$[(n + 1/2)\pi/\beta_0]^2$

Table 1.1 | **Mechanical parameters of a cantilever.** Values of β_n and of the normalized eigenfrequencies (to the fundamental ω_0). The asymptotic values for $n \geq 3$ are also given. These can be obtained by considering that, for large n, $\cosh \beta_n$ diverges and, in order to satisfy Eq. (1.10), $\cos \beta_n$ has to be close to zero. The values can be found in Refs. [18, 40, 41].

In the following subsections, by solving Eq. (1.7), we determine the dynamic displacement for the specific cases of a singly clamped beam (cantilever) and a doubly clamped beam.

1.2.1 Cantilever

A beam clamped at one end and free at the other, in the so called cantilever configuration, is subject to the following boundary conditions [40]:

$$u_n(0) = \frac{\mathrm{d}u_n}{\mathrm{d}z}(0) = \frac{\mathrm{d}^2 u_n}{\mathrm{d}z^2}(L) = \frac{\mathrm{d}^3 u_n}{\mathrm{d}z^3}(L) = 0. \tag{1.9}$$

Inserting these conditions into Eq. (1.7), we find that β_n must obey the equation:

$$\cos \beta_n \cosh \beta_n + 1 = 0, \tag{1.10}$$

the solutions of which are summarized in Table 1.1. The mode shape of a cantilever is then determined to be:

$$u_n(z) = \frac{1}{K_n} \left[S_n \left(\cosh \frac{\beta_n}{L} z - \cos \frac{\beta_n}{L} z \right) - T_n \left(\sinh \frac{\beta_n}{L} z - \sin \frac{\beta_n}{L} z \right) \right], \tag{1.11}$$

where $K_n = 2(\sin \beta_n \cosh \beta_n - \cos \beta_n \sinh \beta_n)$, $S_n = \sinh \beta_n + \sin \beta_n$, and $T_n = \cosh \beta_n + \cos \beta_n$. The constants K_n, S_n, and T_n have been chosen in order to fulfill the normalization condition that the maximum value of $|u_n(z)|$ is unity. This is equivalent, for a cantilever, to pose $u_n(L) = 1$ [41]. The lowest four normalized mode shape functions of a cantilever are shown in Fig. 1.2.

The analysis illustrated so far is independent on the specific shape of the cantilever cross-section, still maintaining the model general assumptions that this has to be thin and uniform throughout the length. Table 1.1 reports the
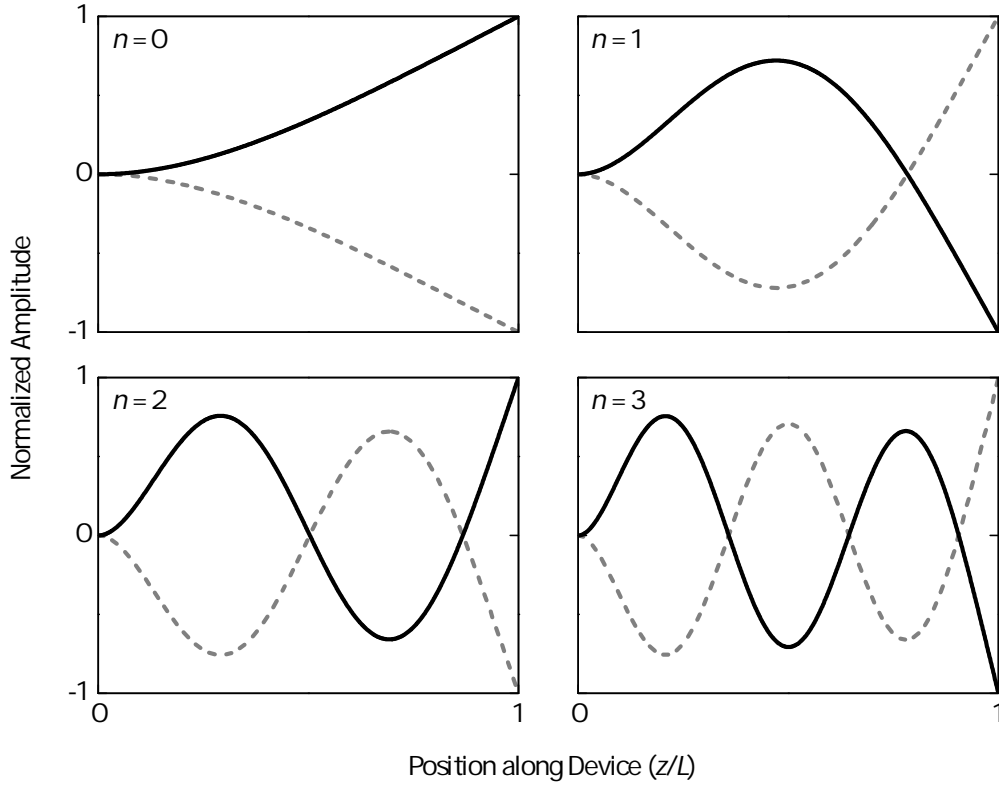
Figure 1.2 | **Mode shape functions of a cantilever.** The normalized functions $u_n(z)$ for the lowest four modes are shown. The corresponding eigenfrequencies are given in Table 1.1.

values of the lowest four eigenfrequencies of a cantilever, calculated according to Eq. (1.8), normalized to the fundamental frequency ω_0. The table also illustrates the asymptotic harmonic behavior for $n \geq 3$ [18, 41].

Now we analyze the specific cases of a few simple geometries. The most discussed one in textbooks deals with a rectangular cross-section of width w and thickness d. Such a geometry is characterized by polar moments of inertia $I_y = wd^3/12$ and $I_x = dw^3/12$ respectively, corresponding to flexural vibrations along the axes $\hat{x}$ and $\hat{y}$. The associated eigenfrequencies are:

$$
\begin{aligned}
\omega_{n,x} &= \beta_n^2 \sqrt{\frac{E_{\mathrm{Y}}}{12\rho}} \frac{d}{L^2}, \\
\omega_{n,y} &= \beta_n^2 \sqrt{\frac{E_{\mathrm{Y}}}{12\rho}} \frac{w}{L^2}.
\end{aligned}
\tag{1.12}
$$

To be noted is the linear dependence of the eigenfrequencies on the cross-section dimensions and the quadratic inverse proportionality on the length. For a squared cross-section ($w = d$), each mode is doubly degenerate. The

same consideration is valid for any other regular polygonal cross-section centered around the cantilever axis. This includes the case of a cylindrical beam of diameter D, for which $I_x = I_y = \pi D^4/64$ and

$$\omega_n = \beta_n^2 \sqrt{\frac{E_{\mathrm{Y}}}{16\rho}} \frac{D}{L^2}, \tag{1.13}$$

and, for example, the case of a cantilever of hexagonal cross-section of side s, for which $I_x = I_y = 5\sqrt{3}\,s^4/16$ and

$$\omega_n = \beta_n^2 \sqrt{\frac{5E_{\mathrm{Y}}}{24\rho}} \frac{s}{L^2}. \tag{1.14}$$

Such a geometry characterizes the self-assembled nanowire resonators studied in detail in Chapter 5 and modeled with a finite element analysis in Section 1.5.

1.2.2 Doubly Clamped Beam

The boundary conditions for a beam clamped and flat at both ends are the following [40]:

$$u_n(0) = u_n(L) = \frac{\mathrm{d}u_n}{\mathrm{d}z}(0) = \frac{\mathrm{d}u_n}{\mathrm{d}z}(L) = 0. \tag{1.15}$$

Inserting these conditions into Eq. (1.7), we obtain that β_n must obey the equation:

$$\cos\beta_n \cosh\beta_n - 1 = 0, \tag{1.16}$$

the solutions of which are summarized in Table 1.2. The mode shape of a doubly beam clamped has then the form:

$$u_n(z) = \frac{1}{K_n}\left[S_n\left(\cosh\frac{\beta_n}{L}z - \cos\frac{\beta_n}{L}z\right) - T_n\left(\sinh\frac{\beta_n}{L}z - \sin\frac{\beta_n}{L}z\right)\right], \tag{1.17}$$

where K_n is a normalization constant determined by the constraint that the maximum value of $|u_n(z)|$ is unity, $S_n = \sinh\beta_n - \sin\beta_n$, and $T_n = \cosh\beta_n - \cos\beta_n$. Equations (1.16) and (1.17) for a doubly clamped beam are then very similar to the corresponding equations (1.10) and (1.11) for a cantilever. However, Table 1.2 shows that the values of β_n for a doubly clamped beam are higher than those of a cantilever with the same dimensions. This is due to the fact that the former has an additional clamping that makes the beam stiffer. Furthermore, in contrast with the case of a cantilever, the position at which $|u_n(z)|$ is maximized is not obvious, except for the

Mode	β_n	ω_n/ω_0
0	4.730	1.000
1	7.853	2.757
2	10.996	5.404
3	14.137	8.933
$n \geq 3$	$(n+3/2)\pi$	$[(n+3/2)\pi/\beta_0]^2$

Table 1.2 | **Mechanical parameters of a doubly clamped beam.** Values of β_n and of the normalized eigenfrequencies (to the fundamental ω_0). The asymptotic values for $n \geq 3$ are also given. They have been obtained by following the consideration given in the caption of Table 1.1. The values can be found in Refs. [18, 40, 41].

fundamental mode, where the maximum displacement is reached at $z = L/2$. Hence the parameter K_n has to be determined numerically [41]. The lowest four normalized mode shape functions of a doubly clamped beam are shown in Fig. 1.3.

1.3   Effective Mass

The application of an external load to a mechanical resonator entails a displacement following a characteristic mode shape. As illustrated in the previous section, the mode shape depends on the mechanical and geometrical properties of the resonator and is in general a non-linear function of position. This means that a volume element in the resonator reacts to the load with an inertia which depends on its specific position. For instance, in a cantilever, volume elements located close to the clamped end react as if the local mass would be higher than the mass around the free-end position. In order to account for this position-dependent inertia when studying the mechanical energy of a resonator, it is very useful to introduce the concept of *effective mass*. Looking in detail, for a generic mechanical resonator, the potential energy dU_{pot} of a volume element dV can be written, according to Hooke's law, as:

$$dU_{\text{pot}} = \frac{1}{2}\rho(\boldsymbol{r})\omega_n^2 |x_n(t)\boldsymbol{u}_n(\boldsymbol{r})|^2 \, dV. \tag{1.18}$$

The total elastic energy associated to the n-th mode is then given by integrating dU_{pot} over the entire volume of the resonator V:

$$
\begin{aligned}
U_{\text{pot}} &= \frac{1}{2}\omega_n^2 |x_n(t)|^2 \int_V \rho(\boldsymbol{r}) |\boldsymbol{u}_n(\boldsymbol{r})|^2 \, dV \\
&= \frac{1}{2}\omega_n^2 |x_n(t)|^2 |\boldsymbol{u}_n(\boldsymbol{r}_0)|^2 \, m_n(\boldsymbol{r}_0). \tag{1.19}
\end{aligned}
$$
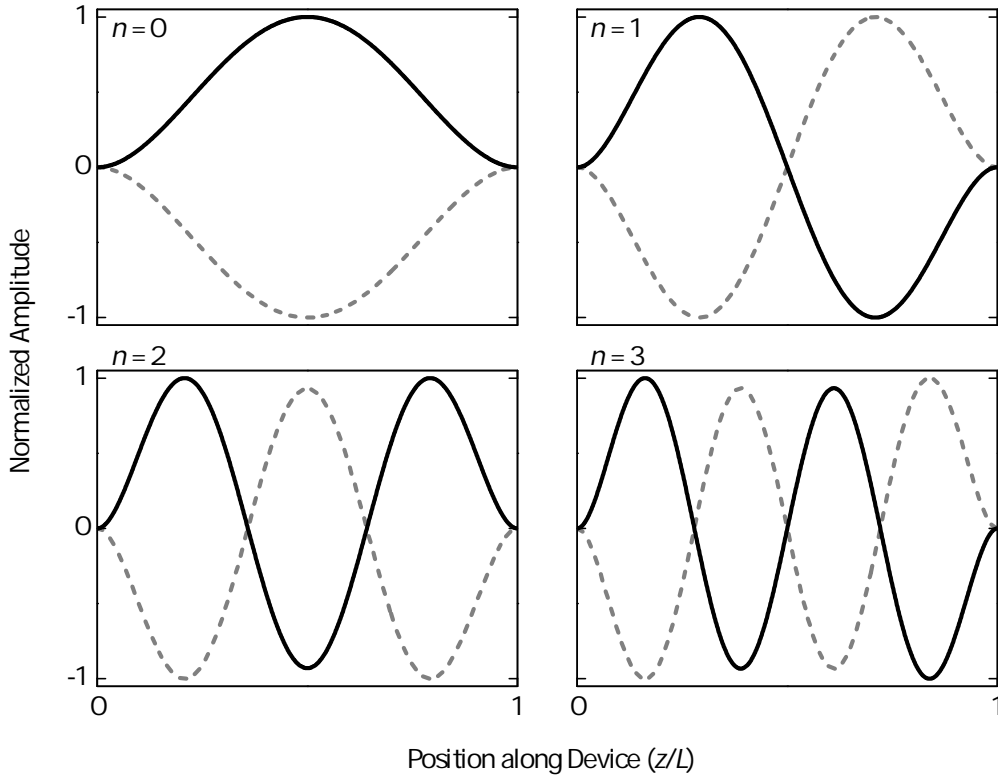
Figure 1.3 | Mode shape functions of a doubly clamped beam. The normalized functions $u_n(z)$ for the lowest four modes are shown. The corresponding eigenfrequencies are given in Table 1.2.

The last equation contains the expression of the effective mass of a mechanical resonator at position $\boldsymbol{r}_0$ [41]:

$$m_n(\boldsymbol{r}_0) \equiv \frac{\int_V \rho(\boldsymbol{r}) \, |\boldsymbol{u}_n(\boldsymbol{r})|^2 \, \mathrm{d}V}{|\boldsymbol{u}_n(\boldsymbol{r}_0)|^2} \tag{1.20}$$

From the definition above, it is evident that the effective mass for a given mode is proportional to the volume of the mode squared inside the resonator. Because of the chosen normalization condition, $|\boldsymbol{u}_n(\boldsymbol{r}_0)| \leq 1$, therefore, when measuring the resonator's motion at some position $\boldsymbol{r}_0$ other than the one of maximum displacement, one has to take into account that the effective mass has increased. The general definition in Eq. (1.20) can be simplified in case of a resonator with uniform density. As mentioned in Section 1.2, the motion of many resonators can be considered as the superposition of one-dimensional displacements. Recalling the initial assumption of resonators with uniform

cross-section, the expression for the effective mass becomes:

$$m_n(z_0) = \frac{\rho A}{|u_n(z_0)|^2} \int_0^L |u_n(z)|^2 \ \mathrm{d}z. \tag{1.21}$$

It is worth emphasizing that the definitions (1.20) and (1.21) depend on the resonator's mode shape, which has been found in the form (1.7). This last expression has been obtained without making any assumption on the specific geometry of the resonator's cross-section. Therefore, maintaining the model's general assumptions of a beam with thin, uniform cross-section, the calculation of the effective mass is valid for a cross-section of any shape.

A useful parameter in nanomechanics is the effective mass ratio, defined as the resonator's effective mass m_n at the position of maximum displacement divided by its total mass M. The effective mass ratio is an intrinsic quantity of a system as it is independent of size or material [41]. In the next subsections, we calculate the effective mass ratio for a cantilever and for a doubly clamped beam.

1.3.1 Effective Mass of a Cantilever

In Section 1.2.1, we have seen that the position of maximum displacement of a cantilever in one dimension is at its free end. At this point, from the normalization condition, $|u_n(L)| = 1$. From the definition of effective mass (1.21), and recalling the expression of $u_n(z)$ (1.11), it follows that, at $z_0 = L$ [41]:

$$\frac{m_n}{M} = \frac{1}{L} \int_0^L |u_n(z)|^2 \ \mathrm{d}z = \frac{1}{4}. \tag{1.22}$$

This result, in its simple form, tells us that the effective mass of a cantilever is constant and equal to 1/4 of its total mass, independently of the mode.

1.3.2 Effective Mass of a Doubly Clamped Beam

Similarly to the case of a cantilever, we calculate the effective mass ratio of a doubly clamped beam at the position of maximum displacement, using the mode shape function $u_n(z)$ expressed in Eq. (1.17). In this case, however, neither the maximum displacement position, nor m_n/M are mode independent. Nevertheless, for $n > 3$, m_n/M saturates to ≈ 0.4372 [41].

1.4 Strain and Stress

The elastic structure of a mechanical resonator implies that its displacement under an external load causes a deformation, or *strain*, of the material. In

order to describe how the material deforms with respect to its relaxed state, the strain is defined as a second-rank tensor of the form [40]:

$$\varepsilon_{ij} \equiv \frac{1}{2}\left(\frac{\partial u_i}{\partial x_j} + \frac{\partial u_j}{\partial x_i}\right), \qquad (1.23)$$

where the x_i, $i = 1$, 2, 3 are the components of the position vector $\boldsymbol{r}$. This definition shows that the strain is symmetric under a reversal of the indices, i.e., $\varepsilon_{ij} = \varepsilon_{ji}$. The diagonal elements ($i = j$) are called normal strains, as they are all related to linear changes in the respective dimensions of the object. The off-diagonal elements ($i \neq j$) are related to angular distortions in the object and are called shear strains.

To deform a material, external forces have to be applied, which in turn give rise to forces inside the material. Each cubic volume element in the material feels the force exerted on its faces by the neighboring elements. The magnitude and direction of this force obviously depend on the location of the element in the material and also on the extension and orientation of its faces [18]. For each face of surface area A, a normal vector $\boldsymbol{n}$ can be defined as the unit vector perpendicular to the surface and having orientation going out from the surface. In condition of static equilibrium, the forces acting on the volume element are assumed equal and opposite on opposite faces. To fully characterize the forces acting on the element, it is then enough to consider only three perpendicular faces, described, as before, by the index $i = 1$, 2, 3. Therefore, a force $\boldsymbol{F}_i$ acting on the face i can be written as:

$$\boldsymbol{F}_i = A\sum_{j=1}^{3} \sigma_{ij}\,\boldsymbol{n}_j. \qquad (1.24)$$

This equation contains an implicit definition of the stress tensor σ_{ij}, which expresses the force per unit surface acting locally on each face of a volume element in the material. The situation is summarized in Fig. 1.4, which shows the role of each of the vectors introduced in this section. It follows from Eq. (1.24) that a positive element of the tensor σ_{ij} corresponds to tensile stress, whereas a negative element corresponds to compressive stress. The condition of static equilibrium applied to the torque requires the stress tensor to be symmetric, i.e., $\sigma_{ij} = \sigma_{ji}$. This property implies that σ_{ij} is guaranteed to have three real eigenvalues σ_x, σ_y, and σ_z, known as the principal values of the stress tensor [40].

To summarize, the strain tensor ε_{ij} describes the local deformation of the material, while the stress tensor σ_{ij} expresses the forces acting inside it. Obviously these two quantities are related to each other. For small deformations, the stress and strain tensors are related linearly via the fourth-
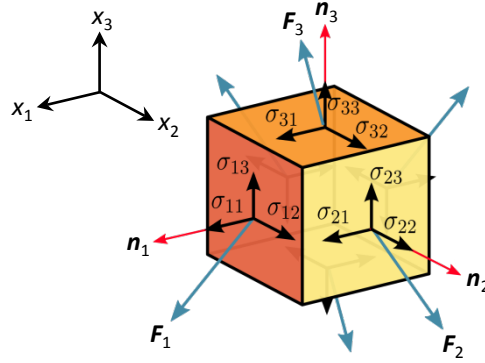
Figure 1.4 │ **Components of the stress tensor.** Adapted from Ref. [42].

rank elasticity tensor α_{ijkl} [18, 40]:

$$\sigma_{ij} = \sum_{k=1}^{3} \sum_{l=1}^{3} \alpha_{ijkl}\, \varepsilon_{kl}. \tag{1.25}$$

The tensor α_{ijkl} has in principle $3^4 = 81$ distinct components. However, the symmetry of both the strain and stress tensors reduces the number of independent components to 36. In general, these components may also vary from point to point within a solid. In this thesis, we assume for simplicity that the studied nanomechanical resonators are made of *homogeneous* and *isotropic* materials. Homogeneous means that the elements of α_{ijkl} are independent of position within the material. Isotropic means that the material is characterized by full rotational and inversion symmetry. This last assumption implies that the elasticity tensor can be described in terms of only two independent material parameters, namely the *Young's modulus* E_{Y} and the *Poisson's ratio* ν [40]. The Young's modulus has units of a pressure, while the Poisson's ratio is dimensionless and, as shown in the next section, expresses the relative strength of the strain tensor components. The relation (1.25) can be inverted, defining the so called compliance tensor C_{ijkl} as the inverse of the elasticity tensor α_{ijkl}:

$$\varepsilon_{ij} = \sum_{k=1}^{3} \sum_{l=1}^{3} C_{ijkl}\, \sigma_{kl}. \tag{1.26}$$

1.4.1 Strain and Stress from Flexural Vibrations

As mentioned earlier, a time-varying transverse load applied to a resonator gives rise to flexural vibrations. In the following, we consider for simplicity a cantilever arranged along $\hat{z}$ and oscillating along $\hat{x}$ only, as in Fig. 1.1. In the

chosen reference system, such a displacement produces, on a long and thin cantilever, a dominant stress component for $(i,\, j) = (3,\, 3)$ and approximately null for the other entries [18]. Such a configuration, corresponding to a stress along only one axis, is called *uniaxial stress*. The stress tensor assumes therefore the simple diagonal form:

$$\sigma_{ij} = \begin{bmatrix} 0 & 0 & 0 \\ 0 & 0 & 0 \\ 0 & 0 & \sigma_z \end{bmatrix}. \tag{1.27}$$

Focusing on the lowest order vibrational mode, the tensor principal value σ_z scales with z and with the distance ξ along $\hat{x}$ from the center of the cross-section, according to [27]:

$$\sigma_z(z,\, \xi) = -E_{\mathrm{Y}} x_{\mathrm{osc}} \xi \, \frac{\mathrm{d}^2 u_0}{\mathrm{d}z^2}. \tag{1.28}$$

Here x_{osc} and u_0 are the oscillation amplitude and the mode shape of the cantilever's fundamental mode, which obey, respectively, Eqs. (1.2) and (1.11). Solving the derivative, it results that the largest stress is obtained at the clamped end of the cantilever ($z = 0$), at the edge of the cross-section ($\xi = \xi^{\mathrm{max}}$), where:

$$\sigma_z^{\mathrm{max}} = E_{\mathrm{Y}} x_{\mathrm{osc}} \beta_0^2 \, \frac{\xi^{\mathrm{max}}}{L^2}. \tag{1.29}$$

For an isotropic material, the application of Eq. (1.26) in case of uniaxial stress of the form (1.27), results in a diagonal strain tensor

$$\varepsilon_{ij} = \begin{bmatrix} -\nu\sigma_z/E_{\mathrm{Y}} & 0 & 0 \\ 0 & -\nu\sigma_z/E_{\mathrm{Y}} & 0 \\ 0 & 0 & \sigma_z/E_{\mathrm{Y}} \end{bmatrix}. \tag{1.30}$$

The first two eigenvalues in the diagonal correspond to linear deformations of the material in the plane perpendicular to the stress direction (xy), and will be called for notation clarity $\varepsilon_\perp$. The third component corresponds instead to a deformation along the stress axis ($\hat{z}$) and will be called $\varepsilon_\parallel$. From the relation (1.30), it is evident the role played by the Poisson's ratio, expressing the relative strength between the strain tensor components:

$$\nu = -\frac{\varepsilon_\perp}{\varepsilon_\parallel}. \tag{1.31}$$

Since in most materials $0 \leq \nu \leq 0.5$ [43], this simple relation indicates that the application of a tensile uniaxial stress produces not only an elongation of the material in the same direction, but also a compression in the perpendicular plane that is ν times smaller. It is important to underline that

a calculation of the strain tensor based on the definition (1.23) and on the initial assumption of cantilever's displacement only along $\hat{x}$ would have not brought to the same result (1.30). The reason is implicit in the assumption, which does not take into account the deformation of the cantilever's cross-section.

Looking at the shape of the strain tensor (1.30) in detail, it is useful to introduce a decomposition into a sum of two different types of deformations: the *isotropic* component $\varepsilon_{ij}^{\text{iso}}$ and the *deviatoric* component $\varepsilon_{ij}^{\text{dev}}$ [44]:

$$\varepsilon_{ij} = \varepsilon_{ij}^{\text{iso}} + \varepsilon_{ij}^{\text{dev}}. \tag{1.32}$$

The component $\varepsilon_{ij}^{\text{iso}}$ describes the isotropic variation of volume of the material, preserving its symmetry. It is also known as hydrostatic component and is proportional to the unitary second-rank tensor:

$$\varepsilon_{ij}^{\text{iso}} = \begin{bmatrix} 1 & & \\ & 1 & \\ & & 1 \end{bmatrix} \eta \varepsilon_{\|}, \qquad \eta \equiv \frac{1 - 2\nu}{3}. \tag{1.33}$$

The deviatoric strain $\varepsilon_{ij}^{\text{dev}}$ describes the distortion of a volume element in the material that occurs without volume variation. It does not preserve the symmetry and is also known as shear strain:

$$\varepsilon_{ij}^{\text{dev}} = \begin{bmatrix} -1/2 & & \\ & -1/2 & \\ & & 1 \end{bmatrix} (1 - \eta)\varepsilon_{\|}, \qquad 1 - \eta = \frac{2(1 + \nu)}{3}. \tag{1.34}$$

To conclude this analysis, it is important to highlight that to the largest stress (1.29), corresponds, in the same point in the cantilever ($z = 0$, $\xi = \xi^{\text{max}}$), also the largest strain, which can be written in terms of the component $\varepsilon_{\|}$ as:

$$\varepsilon_{\|}^{\text{max}} = x_{\text{osc}} \beta_0^2 \frac{\xi^{\text{max}}}{L^2}. \tag{1.35}$$

This relation shows that, for a given displacement amplitude x_{osc}, the value of the maximum strain only depends on the geometry of the beam, and not on any mechanical parameter.

1.5 Finite Element Models

The mechanics of resonators used in experiments are sometimes rather complex for being described by a simple analytical model. Often the geometry of the resonator does not entirely fulfill the general assumptions of Euler-Bernoulli beam theory, or the motion boundary conditions can be non trivial. In these cases, one can resort to a finite element model (FEM). In this
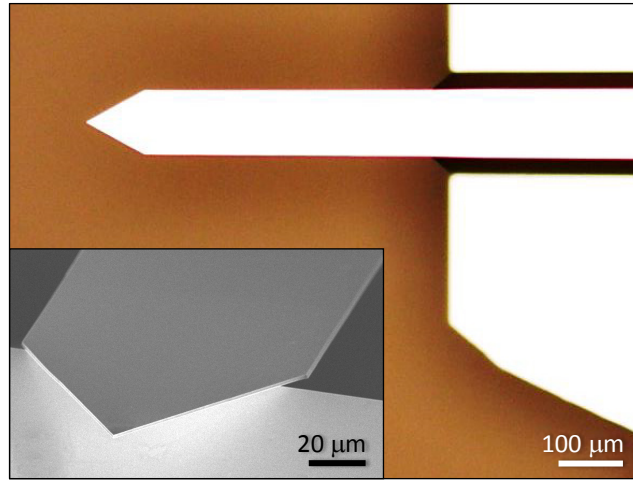
Figure 1.5 | **Commercial cantilever.** Optical micrograph of the Si resonator used in the experiment described in Chapter 3. The inset is a scanning electron micrograph of the cantilever tip.

section, we go through three such models, for resonators involved in the main experiments described in this thesis.

1.5.1   FEM of a Commercial Cantilever

The resonator described in Chapter 3 is a commercial cantilever (Arrow TL1 from NanoWorld AG) made from monolithic highly doped silicon. As shown in Fig. 1.5, it consists of a $(500 \times 100 \times 1)\,\mu\text{m}$ shaft ending with a regular triangular tip, very sharp at the apex (radius of curvature ≈ 10 nm). The cross-section is therefore not uniform across the entire cantilever length, so the mechanics cannot in principle be treated analytically.

As pointed out in the next chapter, it is sometimes not practical to measure the motion of a resonator directly at the location where it matters in the experiment. Nevertheless, it is always possible to retrieve the resonator's displacement at any position by calculating the mode shape function. For this purpose, we realize a FEM of the cantilever. The model, computed on a commercial software (Comsol Multiphisics), provides the mode shapes shown in Fig. 1.6. The eigenfrequency calculated for the fundamental mode matches the experimental finding $\omega_0/(2\pi) = 7.9$ kHz, as mentioned in Section 3.3.1. Due to the large width of the cantilever, compared to its thickness, the mode $n = 2$ is torsional, and for a proper analytical description it would require a two-dimensional analysis. However, the mode shapes of the first two modes overlap with those obtained analytically through Eq. (1.11) and shown in Fig. 1.2, for a cantilever with uniform cross-section and length equal to the
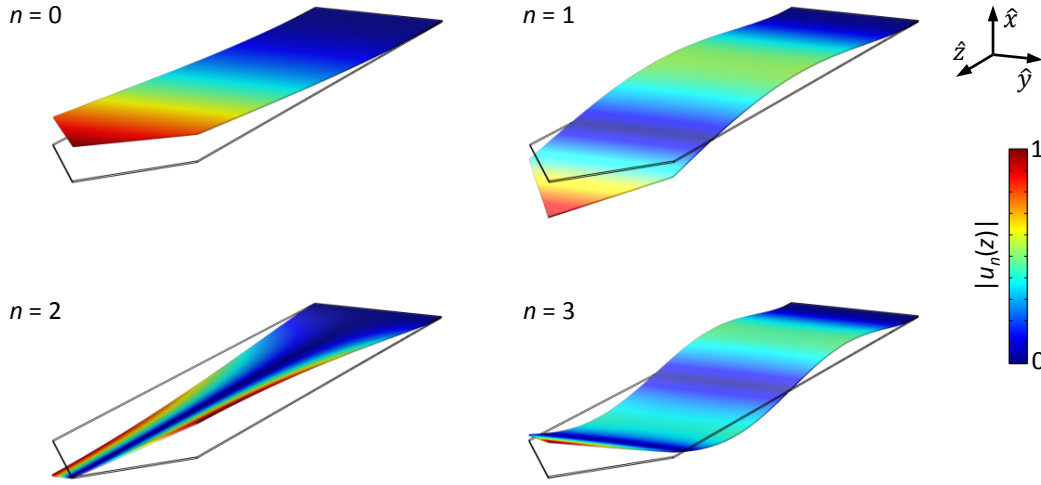
Figure 1.6 | **FEM of the commercial cantilever mode shapes.** The sub-figures display the mode shape of each of the lowest four resonance modes. The color scale is proportional to the amplitude of $|u_n(z)|$, normalized to unity.

total length of the commercial resonator. If the cantilever's displacement in the n-th mode is $U_n(z_0, t)$, measured at some position $z = z_0$, the knowledge of the mode shape function allows the calculation of the time-dependent displacement $x_n(t)$ at the free-end through the following simple equation, which is a direct consequence of the relation (1.3):

$$x_n(t) = \frac{U_n(z_0, t)}{u_n(z_0)}. \tag{1.36}$$

It is important to mention here that the previous expression is related to the normalization choice $|u_n(L)| = 1$, already presented in Sections 1.1 and 1.3.1.

1.5.2 FEM of an Ultra-Soft Cantilever

In the experiment described in the first section of Chapter 4, we study a single-crystal highly doped silicon cantilever, whose ultra-low spring constant makes it ideal for precision sensing. As shown in Fig. 1.7, the cantilever is characterized by a high aspect ratio, with a total length of $180\,\mu\text{m}$, a width of $\approx 4\,\mu\text{m}$ and a thickness of only $100\,\text{nm}$. Close to its free end, the cantilever includes a hexagonal paddle, used for focusing a laser interferometer which measures the displacement (see Chapter 2). The cantilever's tip is loaded with a $1.7\,\mu\text{m}$-thick mass, aimed at repelling high order resonance modes from the fundamental. As in the case previously described, the cross-section is not uniform across the cantilever length, therefore the mechanics are best studied through a finite element model. The computed lowest four mode
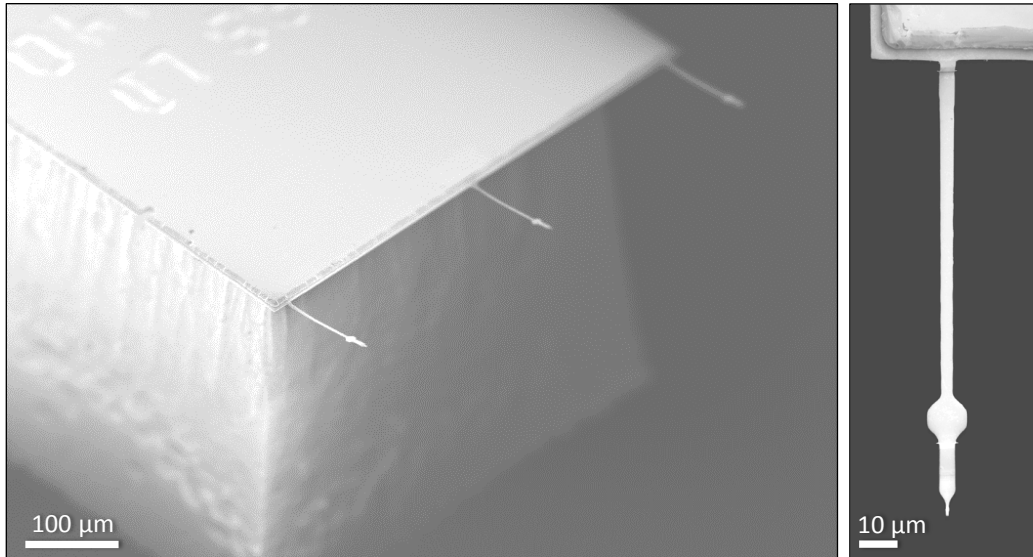
Figure 1.7 | **Cantilever for precision sensing.** SEM images of ultra-soft Si resonators used in the experiment described in Section 4.1. Pictures adapted from Ref. [45].

shape functions are shown in Fig. 1.8. As before, the fundamental eigenfrequency from the FEM matches the experimental result $\omega_0/(2\pi) = 1.9$ kHz, as described in Section 4.1.1. The corresponding mode shape allows the determination of the time-dependent displacement $x_n(t)$ at the free-end from the knowledge of the displacement $U_n(z_0, t)$ measured at the paddle position, by using Eq. (1.36).

1.5.3 FEM of a Nanowire Cantilever

In Chapter 5, the resonator is a GaAs/AlGaAs core-shell nanowire (NW), which is tightly glued to the edge of a Si chip on a lateral facet, in cantilever configuration. The dimensions of the NW and the length of the portion glued to the chip are measured by scanning electron microscopy (SEM), as shown in Fig. 1.9. While its structure is described in detail in Chapter 5, in this section the NW is modeled as an isotropic and homogeneous hexagonal prism of AlGaAs, 20.1 µm long and with the side of the hexagon being $s = 230$ nm. The density is given by the average of the densities of the different GaAs and AlGaAs layers, each weighted according to its thickness.

The FEM provides the mode shapes of the NW flexural vibrations. As explained in Section 1.2.1, a NW of regular hexagonal cross-section clamped at one end possesses doubly degenerate vibrational modes. However, the experimental situation concerns a cantilever clamped with one lateral facet in contact with the substrate. As confirmed by our FEM, such an asymmetric
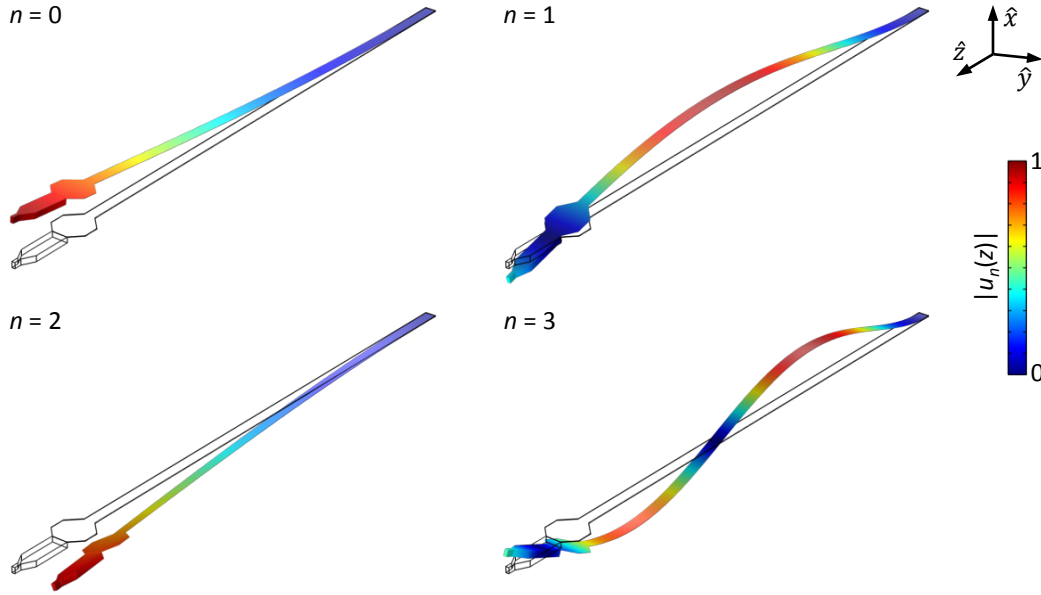
Figure 1.8 │ FEM of the ultra-soft cantilever mode shapes. The sub-figures display the mode shape of each of the lowest four resonance modes. The color scale is proportional to the amplitude of $|u_n(z)|$, normalized to unity.

geometry has the effect of splitting each mode into a doublet of flexural vibrations, oriented either parallel or perpendicular to the Si surface, with the former having the lower eigenfrequency. Figure 1.10 shows the mode shape of the lowest four non-degenerate vibrations. The spectral separation between two non-degenerate modes in each doublet depends, aside from the nature of the clamping, on the symmetry of the NW geometry: a dilatation of the hexagonal cross-section by only 1% along one axis is enough to invert the spectral positions of the two modes.

Despite the asymmetric clamping and the consequent mode splitting, the calculation of the effective mass of the resonator for the lowest four modes, according to the definition (1.21), leads to the same result of the simpler symmetric case. The ratio between the effective mass and the mass of the suspended portion of the NW calculated through the FEM is in fact ≈ 0.25, consistent with the analytical value of $1/4$ (see Section 1.3.1). In detail, it results $m = (3.5 \pm 0.7) \times 10^{-15}$ kg, where the error is dominated by the measurement imprecision on the hexagon side s.

The flexural vibrations produce a time-varying material strain in the NW, which, as shown in Section 1.4.1, translates into a dominant uniaxial stress along the NW growth direction ([$1\bar{1}1$] in crystallographic notation). In order to fully characterize the elastic properties of our resonator, we need to determine the values of the Young's modulus E_Y and of the Poisson's ratio
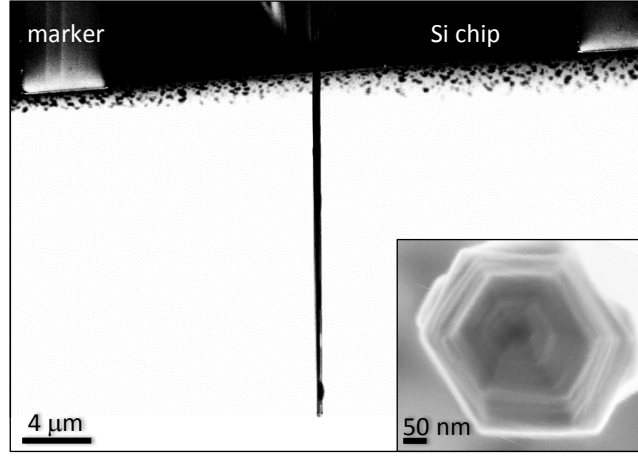
Figure 1.9 | **NW as a cantilever.** SEM image of the NW used as a resonator in the experiment described in Chapter 5. The NW is glued to the edge of a Si chip in a cantilever configuration. The inset shows the NW's hexagonal profile.

ν.

To our knowledge, for a GaAs/AlGaAs nanostructure grown along $\langle 1\,1\,1\rangle$, E_{Y} has not yet been measured. The only reference is the value along this axis measured for bulk GaAs (141.2 GPa) [46]. However, an estimation of E_{Y} for our experimental configuration can be provided by the FEM. Chapter 5 reports that the measured resonance frequency of the lowest perpendicular mode is 795.4 kHz. Since we know the geometric dimensions of the NW, we set E_{Y} as a free parameter in our FEM, while calculating the NW eigen-frequencies. We then tune E_{Y} in the FEM until the calculated resonance frequency of the lowest perpendicular mode matches our experimental finding. The corresponding Young's modulus is then $E_{\mathrm{Y}} = 153$ GPa, which is 8% larger than the aforementioned value measured for bulk GaAs. Possible reasons for this increase of the stiffness of our NW reside in its finite size and in its core-shell structure, which introduces an additional intrinsic material strain.

The Poisson's ratio has been recently measured for Zinc-Blende GaAs/-AlGaAs core-shell NWs grown along $\langle 1\,1\,1\rangle$, as in our case, at a temperature of 100 K [47]. Its value results to be $\nu = 0.16 \pm 0.04$.

Once these fundamental parameters have been inserted into our FEM, we compute the strain distribution along the NW structure. Fig. 1.10 shows in color scale $\varepsilon_{\parallel}$ for the lowest four non-degenerate flexural vibrations, for a NW free-end displacement $x_{\mathrm{osc}} = 1$ nm. The largest strain is obtained at the clamped end of the NW, at the borders of its hexagonal cross-section perpendicular to the oscillation direction, i.e. where $z = 0$ and $\xi = \pm s\sqrt{3}/2$. The value from the FEM for the lowest perpendicular mode is $\varepsilon_{\parallel}^{\mathrm{max}}/x_{\mathrm{osc}} = 1.73 \times$
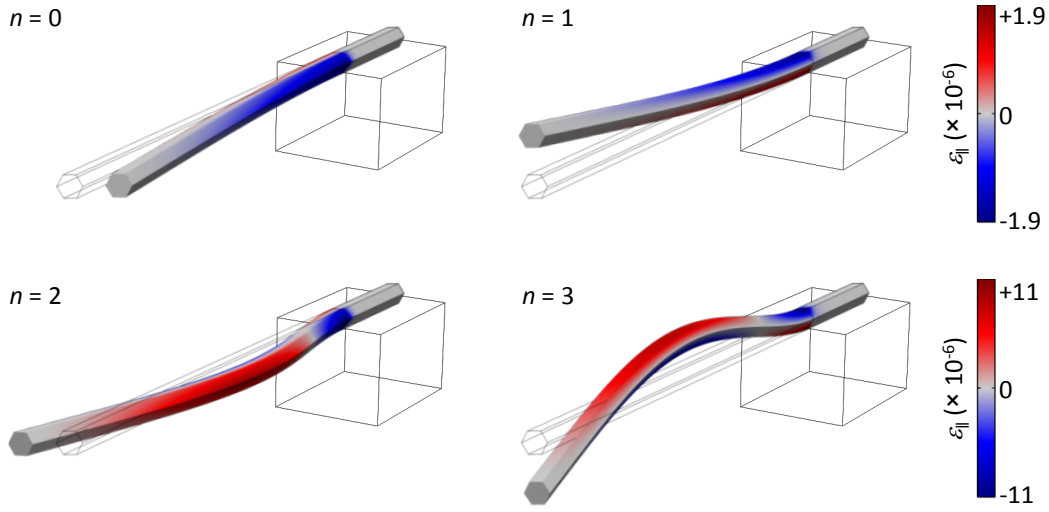
Figure 1.10 │ **FEM of the NW mechanical properties.** The sub-figures show the mode shape of each of the the lowest four non-degenerate vibrations. The color scale is proportional to the component $\varepsilon_\parallel$ of the material strain in the NW, for a 1-nm displacement of its free end.

10^{-6} nm^{-1}, coinciding with the analytical result calculated from Eq. (1.35). The value of the strain scales for higher modes as $(\beta_n/\beta_0)^2$, i.e. as the corresponding eigenfrequencies. Therefore, as confirmed by the FEM analysis, the mode doublet $n = 2$ and 3 results in a maximum strain at the NW's clamped end that is a factor 6 larger than the value of the lowest index doublet (see Table 1.1). However, if the goal is obtaining the largest possible strain in a resonator, one should consider that driving high order modes requires quadratically increasing mechanical excitation. This is due to the fact that the spring constant of a resonator scales as the square of its resonance frequency.

1.6 Thermal and Quantum Noise

In the treatment of mechanical resonators made so far, we have intentionally not mentioned the nature of the forces acting on them. Apart from externally applied forces, ultra-soft micro- and nano-sized resonators interact with the environment with a mutual transfer of energy. The sources of such interaction can be several: for example, the stochastic collisions of the resonator with the molecules of the environment, the phonons in the substrate that couple to the resonator via the clamping points, the motion of charged defects or ions on the surface of the resonator or in its surroundings, etc. [18, 40]. Since all these coupling processes are random and irreversible, they lead to energy

dissipation and to fluctuations in the resonator's vibrations, its so-called *Brownian motion.* In terms of equation of motion, the force exerted by the environment on the resonator can be separated into a *dissipation* term, proportional to the resonator's velocity, and a term due to a random force F_{th}, which constitutes the *thermal noise.* The dynamics of the resonator can therefore be described through the so-called *Langevin equation* [40]:

$$m\ddot{x} + \Gamma\dot{x} + kx = F_{\text{th}}. \tag{1.37}$$

We are here focusing our attention, for simplicity of notation, on only one vibrational mode, but the analysis can be extended to the other modes without losing generality. In the following subsection, we briefly illustrate the equations used to describe the thermal motion of a mechanical resonator. In the next subsection, the limitations imposed by quantum mechanics on the resonator's displacement detection are described.

1.6.1 Displacement Spectral Density

A noisy time-dependent quantity is generally described in terms of its *spectral density* (or power spectrum) $S(\omega)$, which expresses the intensity of the noise at a given frequency [7]. In case of the resonator's displacement $x(t)$, it is first useful to define its Fourier transform over a finite window as follows:

$$\hat{x}_\tau(\omega) \equiv \frac{1}{\sqrt{\tau}} \int_{-\tau/2}^{\tau/2} x(t)\mathrm{e}^{\mathrm{i}\omega t}\,\mathrm{d}t, \tag{1.38}$$

where τ is the sampling time. The definition of spectral density of $x(t)$ is then [7]:

$$\bar{S}_x(\omega) \equiv \lim_{\tau \to \infty} \left\langle |\hat{x}_\tau(\omega)|^2 \right\rangle. \tag{1.39}$$

The last relation can also be inverted, expressing the signal fluctuation as a function of the spectral density. To do so, we first introduce the autocorrelation function $K_x(t)$, which describes how $x(t')$ is related to itself at a later time $t' + t$ [41]:

$$K_x(t) \equiv \lim_{\tau \to \infty} \frac{1}{\tau} \int_0^\tau x(t')x(t' + t)\,\mathrm{d}t'. \tag{1.40}$$

The spectral density is then related to $K_x(t)$ through its Fourier transform [7, 18, 40, 41]:

$$\bar{S}_x(\omega) = \int_{-\infty}^{\infty} K_x(t)\mathrm{e}^{\mathrm{i}\omega t}\,\mathrm{d}t. \tag{1.41}$$

Note that the spectral density $\bar{S}_x(\omega)$ in the definition (1.39) and in the relation above spans both positive and negative frequencies. For real-valued signals, as it is the case in physical situations, $\bar{S}_x(\omega)$ is an even function [7].

For this reason, we adopt in the following the convention for the single-sided spectral density [18, 41]:

$$S_x(\omega) \equiv \bar{S}_x(\omega) + \bar{S}_x(-\omega). \tag{1.42}$$

This definition still allows the conservation of the total power in the signal when $S(\omega)$ is integrated only over positive frequencies. Finally, we show that the fluctuation of a signal $x(t)$ is connected to its autocorrelation function $K_x(t)$. In fact, provided that the sampling time is sufficiently long (i.e. $\tau \gg 2\pi/\omega_0$, ω_0 being the angular resonance frequency), we have:

$$\langle x^2 \rangle \equiv \frac{1}{\tau} \int_0^\tau [x(t)]^2 \, dt = K_x(0). \tag{1.43}$$

Therefore, from the inverse Fourier transform of Eq. (1.41), we get:

$$\langle x^2 \rangle = \frac{1}{2\pi} \int_0^\infty S_x(\omega) \, d\omega. \tag{1.44}$$

Such equation provides a direct connection between the root-mean-squared thermal motion x_{rms} and its spectral density:

$$x_{\mathrm{rms}} = \frac{x_{\mathrm{osc}}}{\sqrt{2}} = \sqrt{\frac{1}{2\pi} \int_0^\infty S_x(\omega) \, d\omega}. \tag{1.45}$$

In the following, we derive an analytical expression for $S_x(\omega)$. The Fourier transform of both members of the equation of motion (1.37) provides the frequency response of the resonator:

$$\hat{x}(\omega) = \frac{1/m}{\omega_0^2 - \omega^2 + i\omega_0\omega/Q} \, \hat{F}_{\mathrm{th}}(\omega), \tag{1.46}$$

where we have replaced the dissipation Γ with the expression containing the quality factor $Q = m\omega_0/\Gamma$. The random nature of the thermal force F_{th} implies that, on a long time scale, F_{th} is uncorrelated from the displacement $x(t)$. From the definition (1.39), we are then able to determine the displacement spectral density [18, 32, 41]:

$$S_x(\omega) = \frac{1/m^2}{(\omega_0^2 - \omega^2)^2 + \omega_0^2\omega^2/Q^2} \, S_{F_{\mathrm{th}}}, \tag{1.47}$$

where $S_{F_{\mathrm{th}}}$ is the spectral density of the thermal noise force, considered white in the bandwidth of the resonator. Recurring to the relation (1.44), and solving the integral, we are then able to directly connect the fluctuation of the Brownian motion with $S_{F_{\mathrm{th}}}$ [41]:

$$\langle x^2 \rangle = \frac{Q}{4\omega_0^3 m^2} \, S_{F_{\mathrm{th}}}. \tag{1.48}$$

In condition of equilibrium, the temperature of the resonator is equal to the environmental temperature T. The equipartition theorem [48] establishes a connection between the energy of the resonator (potential and kinetic) and the equilibrium temperature:

$$\frac{1}{2}k\left\langle x^2\right\rangle = \frac{1}{2}m\left\langle \dot{x}^2\right\rangle = \frac{1}{2}k_{\mathrm{B}}T, \tag{1.49}$$

where k_{B} is the Boltzmann's constant. By combining this relation with Eq. (1.48), we are then able to express the thermal force spectral density as:

$$S_{F_{\mathrm{th}}} = \frac{4k_{\mathrm{B}}T\omega_0 m}{Q} = 4k_{\mathrm{B}}T\Gamma. \tag{1.50}$$

Such a result is known as *fluctuation-dissipation theorem* and has a general validity on systems governed by a *Langevin equation*, as the (1.37) [40]. It shows that the thermal force spectral density can be expressed in terms of the intrinsic properties of the resonator and the environmental temperature, ignoring the microscopic origin of the force. Furthermore, it highlights that the force noise determines the quality factor (or conversely the dissipation) of the resonator [18].

Combining the result (1.50) into Eq. (1.47), we can finally express the spectral density of the resonator's thermal noise as:

$$S_x(\omega) = \frac{4k_{\mathrm{B}}T\omega_0}{mQ\left[(\omega_0^2 - \omega^2)^2 + \omega_0^2\omega^2/Q^2\right]}, \tag{1.51}$$

or, in terms of the spring constant $k = m\omega^2$:

$$S_x(\omega) = \frac{4k_{\mathrm{B}}T\omega_0^3}{kQ\left[(\omega_0^2 - \omega^2)^2 + \omega_0^2\omega^2/Q^2\right]}. \tag{1.52}$$

As illustrated in detail in the next chapter, experimentally the motion of a resonator is transduced by the measurement apparatus into a time-varying electrical signal. Generally this signal is transformed into the frequency domain, for example by means of a spectrum analyzer, thus providing the spectral representation of the resonator's motion. The response of a spectrum analyzer is typically the one-sided spectral density $S_x(\omega)$, combined with other measurement noise sources. Assuming this noise to be white and uncorrelated to the resonator's displacement, the two signals add to each other in quadrature [7], giving a measured voltage spectral density of the form:

$$S_V(\omega) = \alpha^2\left[S_{x_{\mathrm{n}}} + S_x(\omega)\right]. \tag{1.53}$$

Here $S_{x_{\mathrm{n}}}$ represents a constant offset due to the white measurement noise and α is a coupling coefficient which accounts for the transduction of the

resonator's motion into a voltage signal. The graph in Fig. 1.11 shows an experimental displacement spectrum of the fundamental mode of a nanomechanical resonator. By means of the relations (1.51) – (1.53), the function $S_V(\omega)$ can be fit directly to physical data to extract the resonator's mechanical properties. In the figure, the role of such properties on the displacement spectrum is highlighted. As pointed out in the next chapters, in this thesis α is obtained directly from the detector's properties, and not from the fit of the spectrum. Through the relation (1.45), we are now able to determine the displacement of the resonator on resonance. Furthermore, we can express the displacement *sensitivity* of the detector, given by $\sqrt{S_{x_n}}$. Such a parameter is generally used as a figure of merit for a detection system, as it is a measure of the minimum detectable signal for that setup [41]. Note that, being expressed in units of $m/\sqrt{Hz}$, the sensitivity does not depend on the specific measurement bandwidth, nor, conversely, on the wait time. Longer measurements average out the white noise, leading to a reduction of the displacement uncertainty: this bandwidth-dependent parameter is usually referred as the *resolution* of the detector [18]. The signal-to-noise ratio (SNR) is given by the height of the resonance peak divided by the height of the noise floor (i.e. the sensitivity squared). As shown in Fig. 1.11, in order to obtain a large SNR, it results advantageous to have a resonator with high Q and low k.

We have seen that the equipartition theorem connects, in condition of thermal equilibrium, the resonator's temperature to the fluctuation of its Brownian motion, by means of Eq. (1.49). Out of equilibrium, the fluctuation-dissipation theorem no longer holds in the form (1.50) and the temperature of the resonator may be different from the one of the environment [18]. It is then necessary to define an effective temperature of the resonator, as follows:

$$T_{\text{eff}} \equiv \frac{k \langle x^2 \rangle}{k_B} = \frac{k}{2\pi k_B} \int_0^\infty S_x(\omega) \, d\omega. \tag{1.54}$$

In the second passage, we have made use of the relation (1.44), showing that the resonator's effective temperature is proportional to the area under the spectral density, or, in terms of experimental data, to the area between $S_V(\omega)/\alpha^2$ and the noise floor S_{x_n}, as shown in Fig. 1.11. In equilibrium condition, Eq. (1.54) still leads to $T_{\text{eff}} = T$. However, the force noise can be larger or smaller than the equilibrium value expressed in Eq. (1.50), leading to an effective heating or cooling of the resonator. Chapter 3 is mainly devoted to the study of a cantilever whose fundamental mode effective temperature is cooled below T by means of an applied feedback force.

In the analysis made so far, we have neglected the action of the detector on the resonator's motion. As exposed in the next subsection, the role of the detector has to be taken into account when the measurement sensitivity is pushed down to the limits imposed by quantum mechanics.
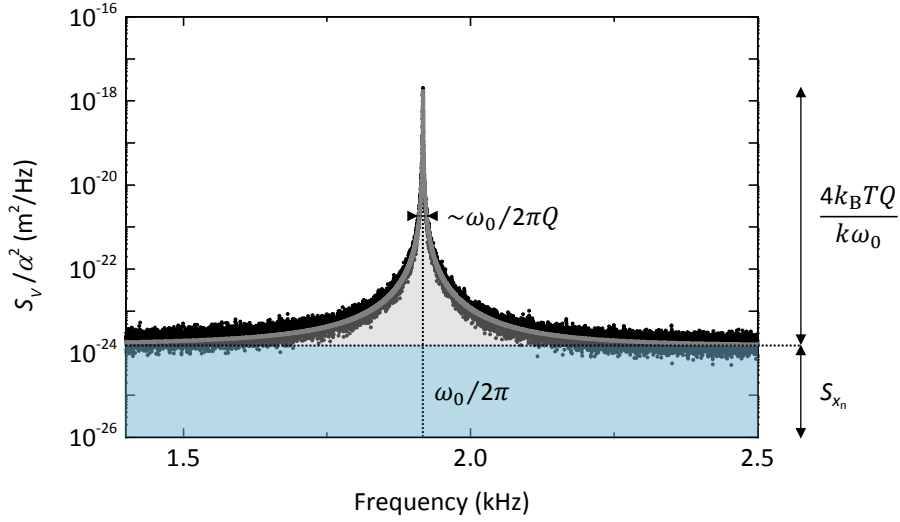
Figure 1.11 | **Thermal noise spectral density.** Plot (in black dots) of the spectrum of a resonator's fundamental mode, measured with a fiber-optic interferometer (see Section 2.1). The resonator is the ultra-soft Si cantilever described in Section 1.5.2. At $T = 4.2$ K and $p < 10^{-6}$ mbar, it has $k_0 = 100\,\mu$N/m and $Q_0 = 10^4$, at (see Chapter 4). The gray curve fits the experimental data according to Eqs. (1.51) – (1.53). The graph highlights the role of the mechanical parameters of the resonator on its displacement spectrum. In particular, the gray area included between the fit and the noise floor S_{x_n} is proportional to the resonator's effective temperature.

1.6.2 The Standard Quantum Limit

When a nanomechanical resonator is cooled to very low temperatures, the classical description fades into a quantized energy-level picture. Each vibrational mode is then characterized by a quantized energy, which, according to the model of a quantum harmonic oscillator, can be written as:

$$E_N = \hbar\omega_n \left(\frac{1}{2} + N\right), \tag{1.55}$$

where $\hbar = h/2\pi$ is the reduced Plank's constant and $N = 0, 1, 2, ...$ is the mode occupation number. The quantum ground state ($N = 0$) has a non-vanishing eigenenergy $E_0 = \frac{1}{2}\hbar\omega_n$, called the *zero-point energy* [18]. From the corresponding wavefunction, it is possible to derive the amplitude of the quantum fluctuations of the resonator's position at the ground-state, the so-called *zero-point fluctuations* [7, 18]:

$$x_\mathrm{zpf} \equiv \sqrt{\langle 0|\,\hat{x}^2\,|0\rangle}, \tag{1.56}$$

$\hat{x}$ denoting here the position operator. However, a more elegant way to find the expression of x_zpf consists in applying the virial theorem [49] to the

Hamiltonian of the quantum harmonic oscillator. Given the Hamiltonian

$$\hat{H} = \frac{\hat{p}^2}{2m} + \frac{m\omega_n^2 \hat{x}^2}{2}, \tag{1.57}$$

($\hat{p}$ is the momentum operator), and calling $\hat{K}$ and $\hat{U}$ the kinetic and the potential energy operators, we can write:

$$\langle N|\,\hat{K}\,|N\rangle = \langle N|\,\hat{U}\,|N\rangle = \frac{1}{2}\,\langle N|\,\hat{H}\,|N\rangle\,. \tag{1.58}$$

From these relations, it results:

$$\frac{1}{2m}\,\langle N|\,\hat{p}^2\,|N\rangle = \frac{m\omega_n^2}{2}\,\langle N|\,\hat{x}^2\,|N\rangle = \frac{1}{2}\,E_N, \tag{1.59}$$

and in particular, for the ground state:

$$x_{\mathrm{zpf}} = \sqrt{\frac{\hbar}{2m\omega_n}}. \tag{1.60}$$

For a quantum harmonic oscillator coupled to a thermal bath, the average mode occupation number N_{th} follows the so-called *Planck distribution*, which is a particular case of Bose-Einstein distribution when the total number of particles is not fixed:

$$N_{\mathrm{th}} = \frac{1}{e^{\hbar\omega_n/k_{\mathrm{B}}T} - 1}. \tag{1.61}$$

The average mode energy is then expressed by:

$$\langle E \rangle = \hbar\omega_n \left(\frac{1}{2} + \frac{1}{e^{\hbar\omega_n/k_{\mathrm{B}}T} - 1} \right) = k_{\mathrm{B}} T_{\mathrm{eff}}, \tag{1.62}$$

where the last passage expresses the relation with the mode effective temperature of the resonator T_{eff}. Equation (1.62) sets the temperature limit for the emergence of quantum effects on the mechanical resonator. For high temperature, i.e. $k_{\mathrm{B}}T \gg \hbar\omega_n$, the expression reduces to the classical equipartition of energy, and $T_{\mathrm{eff}} = T$. The classical description breaks down for $k_{\mathrm{B}}T \approx \hbar\omega_n$. In such a situation, the resonator's temperature differs from the one of the bath and the thermal force spectral density can be written as:

$$S_{F_{\mathrm{th}}} = 4\hbar\omega_n \left(\frac{1}{2} + \frac{1}{e^{\hbar\omega_n/k_{\mathrm{B}}T} - 1} \right) \Gamma, \tag{1.63}$$

which is a generalization of the fluctuation-dissipation theorem (1.50). In the low temperature limit, it becomes $N_{\mathrm{th}} \ll 1$ and the resonator is mostly found

in its ground state. Then $S_{F_{\text{th}}} = 2\hbar\omega_n\Gamma$ and, from Eq. (1.47), the oscillator's displacement spectral density on resonance assumes a value:

$$S_x^{\text{zpf}} = \frac{2\hbar}{\omega_n\Gamma}.$$

(1.64)

In other words, Eq. (1.64) expresses the peak spectral density of the resonator's zero-point fluctuations.

It is known since its discovery in 1927, that the Heisenberg uncertainty principle imposes a limit on the precision with which conjugate observables can be measured [50]. Nevertheless, Heisenberg's relation for position and momentum standard deviations, $\Delta x \cdot \Delta p \geq \hbar/2$, does not forbid the determination of the position with arbitrary accuracy in a single measurement [18]. Most measurements, however, do not consist in a single read-out, but are rather *weak continuous measurements* of the resonator's position. This means that the read-out is sufficiently weak that the position undergoes many cycles of oscillation before significant information is acquired [7]. What is then measured is not the instantaneous position, but rather the overall amplitude and phase. In a weak continuous measurement, the read-out of the position exerts a random force on the resonator which alters its momentum. During the subsequent time evolution, the perturbation introduced by this random force translates into a random fluctuation of the position. This influence of the measurement on the resonator is called *back-action*. Experimentally, back-action results in three different effects on the resonator [18]:

1. a frequency shift;

2. a variation of the dissipation;

3. a change in the resonator's temperature.

In terms of position measurement, let us suppose to have a quantum limited detector available, that is a detector whose measurement sensitivity S_x^{imp} is only limited by shot-noise. S_x^{imp} plays the role of the white noise imprecision S_{x_n} in Eq. (1.53). For a certain signal power, the detector's shot-noise $S_{V_n} = \alpha^2 S_x^{\text{imp}}$ is independent of the position measurement. Therefore an increase of the coupling α between the detector and the resonator causes a quadratic decrease of S_x^{imp}.

As described before, an accurate position measurement results in a back-action force noise, and vice versa. This back-action force increases linearly with α [18], as the influence of the detector on the resonator becomes stronger. Thus the resulting back-action imprecision S_x^{ba} goes as α^2. Since the back-action force is not correlated to the detector's shot-noise, the total measured spectral density S_x includes the noise contributions of both S_x^{imp} and S_x^{ba} as

a simple sum. Given their reciprocal dependence on α^2, when the two noise sources both have an equal contribution, then $S_x(\alpha^2)$ reaches a minimum [7]. According to the Heisenberg uncertainty principle, this happens when the measurement imprecision and the motion resulting from the back-action force each add a noise energy equal to $\hbar\omega_n/4$ [5,7]. This fundamental lower bound for S_x is known as the *standard quantum limit* (SQL) of continuous position detection.

At the SQL, the position noise added by the measurement ($S_x^{\text{imp, SQL}} + S_x^{\text{ba, SQL}}$) has the same energy contribution of the resonator's zero-point fluctuations ($\hbar\omega_n/2$), and the corresponding spectral densities on resonance are also equal:

$$S_x^{\text{imp, SQL}} + S_x^{\text{ba, SQL}} = S_x^{\text{zpf}}. \tag{1.65}$$

Although the total added noise is at a minimum, the uncertainty principle does not forbid the measurement sensitivity S_x^{imp} from becoming arbitrarily small compared to that at the SQL [5].

To summarize, in the limit $k_{\text{B}}T \ll \hbar\omega_n$, the total measured spectral density S_x has three contributions: two are given by the measurement noise, namely S_x^{imp} and S_x^{ba}, the third is the zero-point fluctuations spectrum of the resonator S_x^{zpf}. S_x reaches a minimum at the SQL, whose value, from Eq. (1.64), is:

$$S_x^{\text{min}} = 2 \times S_x^{\text{zpf}} = \frac{4\hbar}{\omega_n\Gamma}. \tag{1.66}$$

Figure 1.12, adapted from Ref. [5], illustrates the concepts described in this section. In order to quantify the noise of a measurement, a natural scale is provided by the imprecision at the SQL, $S_x^{\text{SQL}} = \hbar/(\omega_n\Gamma)$. At the oscillator's resonance frequency, S_x^{SQL} corresponds to the noise energy of $\hbar\omega_n/4$. Note that at finite temperature, a thermal contribution to S_x must be also taken into account, in addition to the three contributions mentioned before.

In the next Chapter, we deal with the detection of a nanomechanical resonator's displacement. In particular, two different schemes employed in the work of this thesis are described in detail, each presenting advantages or limitations in specific applications.
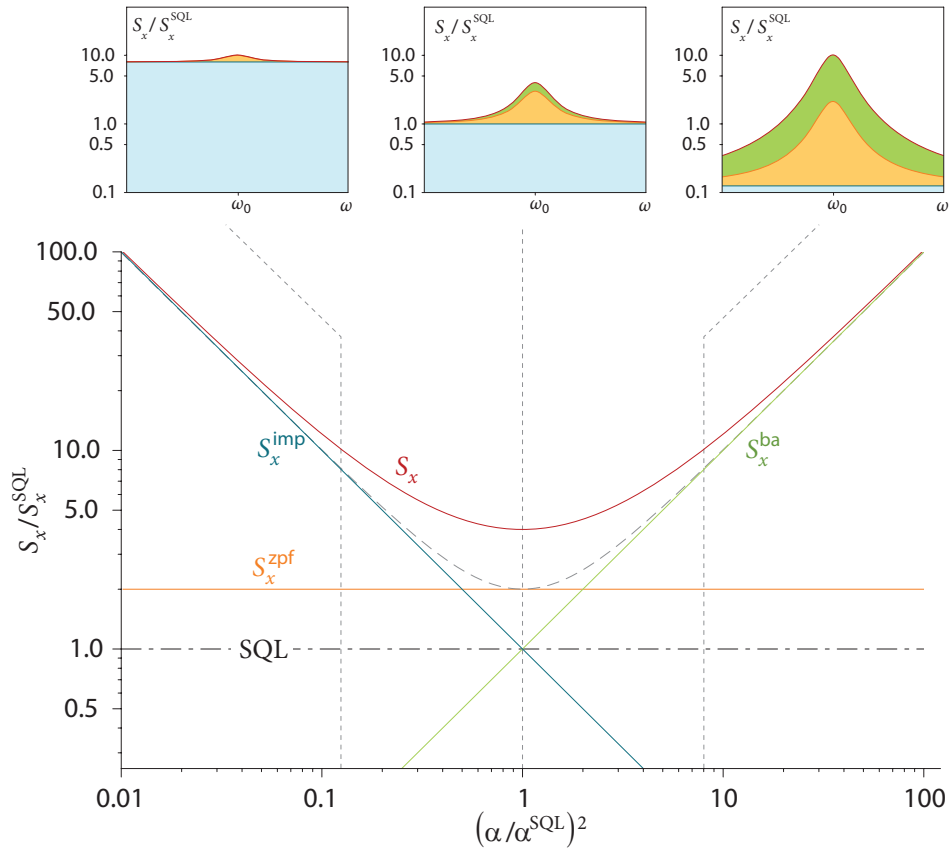
Figure 1.12 | **Displacement detection at the SQL.** A quantum limited displacement detector at $T \approx 0$ measures a spectral density S_x (red curve) given by three different contributions: the shot-noise limited measurement imprecision S_x^{imp} (blue), the back-action noise S_x^{ba} (green) and the resonator's zero-point fluctuations S_x^{zpf} (orange). At the optimal coupling α^{SQL}, S_x^{imp} and S_x^{ba} contribute equally to the measurement noise, each with energy $\hbar\omega_n/4$. In the main graph, S_x/S_x^{SQL} is plotted as a function of $(\alpha/\alpha^{\text{SQL}})^2$, showing its different contributions. In the sub-figures, such contributions are displayed as a function of frequency for three different values of α. Adapted from Ref. [5].

2 | Displacement Detection

The previous chapter shows that the one-sided spectral density $S_x(\omega)$ is commonly used to express the displacement spectrum of a nanomechanical resonator. Experimentally, the resonator's motion is detected by means of a transducer, which converts it into an electrical signal. In this chapter, we illustrate two experimental schemes used in this thesis to detect the displacement of a cantilever with high sensitivity, eventually below the level of thermal motion. Both methods involve a linear displacement detector, i.e. a detector whose output depends linearly on the displacement of the resonator.

The first detector described is the fiber-optic interferometer. This is a well established sensor, used and developed in the last 25 years starting from the works of Drake and Leiner [51], and of Rugar and collaborators [52, 53].

In the second section, we analyze the theory underlying an innovative transducer, consisting of a quantum point contact (QPC), and we compare it to the other schemes developed for detecting motion at the nano-scale. Conceived by Poggio and collaborators [54], the off-board QPC sensor has been further developed and exploited with the work of this thesis. As described in detail in Chapter 3, a QPC has been employed to measure and control the low-temperature thermal motion of a nearby micromechanical cantilever [33].

2.1   Fiber-Optic Interferometer

The fiber-optic interferometer is well suited to detect deflections of micro- and nano-sized cantilevers, thanks to its high sensitivity ($< 10^{-12}$ m Hz$^{-1/2}$ [32]), good low-frequency stability, and compactness [52, 53, 55]. Because of its operability in remote environments, such as in vacuum and/or at low temperatures, it has been adopted in several applications, ranging from sensitive nanomechanics experiments [32, 33, 54, 56] to magnetometry [57, 58] and scanning force microscopy [51–53], in particular magnetic resonance force microscopy (MRFM) [59–61].

In the experiments described in this thesis, two different interferometer setups have been employed, according to the specific needs of the measure-
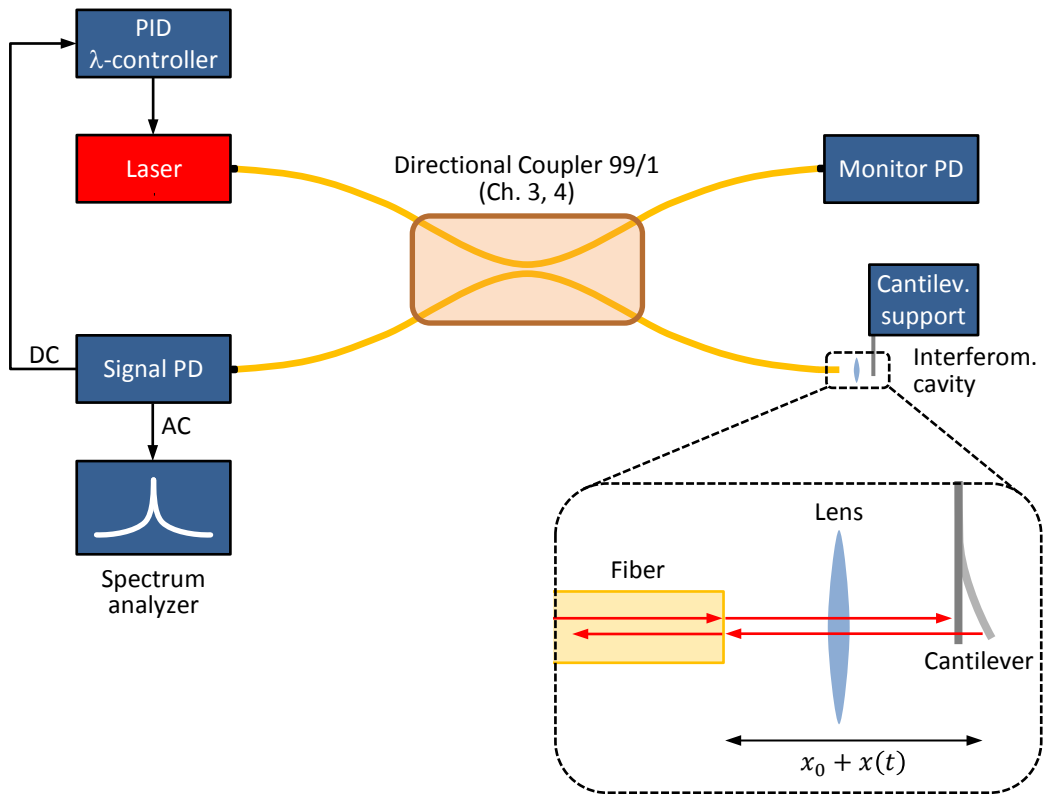
Figure 2.1 | **Scheme of the fiber-optic interferometer.** This arrangement is optimized for maximum displacement sensitivity and is part of the experimental setup described in Chapters 3 and 4.

ments that have been performed. The technical details of each arrangement are specified in Chapters 3 and 5. However, the two configurations share common operation principles. The experimental setup optimized for maximum displacement sensitivity is schematized in Fig. 2.1. Coherent light from a laser diode is coupled into one arm of a 2×2 single-mode directional coupler. The coupler splits the incident optical power between its two outputs with a 99/1 coupling ratio, thereby serving as an interferometric beam splitter [62]. This means that 99% of the light is directed to a power monitor photodetector, while only the remaining 1% is coupled into a sensing fiber terminated with a perpendicular cleaved facet. The cleaved end is typically positioned nearby the cantilever (this is not the case of the interferometer described in Chapter 5), on which the laser beam is focused through a collimating lens. Light reflects from both the cantilever and the cleaved facet, then travels back up the sensing fiber, where it interferes to form a displacement-dependent signal. 99% of this interference signal is then transmitted by the directional coupler to a second photodetector (PD), which produces a voltage

proportional to the signal power. In order to achieve interference, the laser's coherence length has to be longer than at least twice the cavity size, i.e. the distance between the cleaved facet and the cantilever. For better stability and sensitivity, the cavity can be designed in the sub-mm range, thus not requiring a laser with long coherence length. In addition, the use of a short coherence length laser improves the low-frequency stability of the sensor, by eliminating interference effects of stray reflections [53]. Another option, used in the experiments described in Chapters 3 and 4, is to reduce the coherence length to the desired range by modulating the laser power with a suitable radio-frequency signal.

Assuming the reflectivities of the cleave-air interface R_1 and of the cantilever-air interface R_2 to be small ($R_1, R_2 \ll 1$), we can ignore the effects of multiple reflections in the cavity (low-finesse). The interferometer response can thus be modeled simply as the two component interference between reflections from the fiber end and the cantilever [52]. In terms of the electric field E_i incident on the fiber end, the detected optical power P_r can be written as:

$$
\begin{aligned}
P_r &= \left| (E_i \sqrt{R_1}\mathrm{e}^{\mathrm{i}\phi_1} + E_i \sqrt{1 - R_1}\sqrt{R_2}\sqrt{1 - R_1}\mathrm{e}^{\mathrm{i}\phi_2}) \right|^2 \\
&= E_i^2 R_1 + E_i^2 R_2 (1 - R_1)^2 + E_i^2 \sqrt{R_1 R_2}(1 - R_1)\left[\mathrm{e}^{\mathrm{i}(\phi_1 - \phi_2)} + \mathrm{e}^{\mathrm{i}(\phi_2 - \phi_1)} \right] \\
&= E_i^2 R_1 + E_i^2 R_2 (1 - R_1)^2 + 2E_i^2 \sqrt{R_1 R_2}(1 - R_1)\cos\left(\phi_1 - \phi_2\right) \\
&= E_i^2 R_1 + E_i^2 R_2 (1 - R_1)^2 + 2E_i^2 \sqrt{R_1 R_2}(1 - R_1)\cos\frac{4\pi l}{\lambda} \\
&\approx E_i^2 \left(R_1 + R_2 + 2\sqrt{R_1 R_2}\cos\frac{4\pi l}{\lambda} \right),
\end{aligned}
\tag{2.1}
$$

where l is the cavity length, λ is the laser wavelength, ϕ_1 and ϕ_2 are the phase shifts acquired by the light reflected respectively from the fiber end and from the cantilever. In the last passage we have neglected the terms proportional to the reflectivity squared, consistently with the initial hypothesis of $R_1, R_2 \ll 1$. In the subsequent analysis, we make use of the following definitions for the maximum and minimum output powers due to constructive and destructive interference, and to the amplitude and average values of the interference fringe:

$$
\begin{aligned}
P_{\mathrm{max}} &= E_i^2 (R_1 + R_2 + 2\sqrt{R_1 R_2}), \\
P_{\mathrm{min}} &= E_i^2 (R_1 + R_2 - 2\sqrt{R_1 R_2}), \\
P_{\mathrm{amp}} &= \frac{P_{\mathrm{max}} - P_{\mathrm{min}}}{2} = 2E_i^2 \sqrt{R_1 R_2},
\end{aligned}
$$

$$P_{\text{avg}} = \frac{P_{\text{max}} + P_{\text{min}}}{2} = E_i^2(R_1 + R_2),$$

$$\bar{V} \equiv \frac{P_{\text{amp}}}{P_{\text{avg}}} = \frac{2\sqrt{R_1 R_2}}{R_1 + R_2}. \tag{2.2}$$

The last relation is the definition of the *visibility* of the interferometer $\bar{V}$, a parameter related, as we clarify later, to the transduction efficiency and hence to the sensitivity of the interferometer. With the previous definitions, we finally obtain that P_r varies with the average output power P_{avg} as:

$$P_r = P_{\text{avg}}\left(1 + \bar{V}\cos\frac{4\pi l}{\lambda}\right). \tag{2.3}$$

The cavity length l varies in time with the cantilever's displacement. It can be written as the sum of the equilibrium position x_0 and a sinusoidal oscillation $x(t)$, assumed to have an amplitude much smaller than λ. The relation (2.3) then becomes:

$$\begin{aligned}
P_r &= P_{\text{avg}}\left\{1 + \bar{V}\cos\frac{4\pi}{\lambda}[x_0 + x(t)]\right\} \\
&= P_{\text{avg}}\left\{1 + \bar{V}\left[\cos\frac{4\pi}{\lambda}x_0\cos\frac{4\pi}{\lambda}x(t) - \sin\frac{4\pi}{\lambda}x_0\sin\frac{4\pi}{\lambda}x(t)\right]\right\} \\
&\approx P_{\text{avg}}\left\{1 + \bar{V}\left[\cos\frac{4\pi}{\lambda}x_0 - \frac{4\pi}{\lambda}x(t)\sin\frac{4\pi}{\lambda}x_0\right]\right\}. \tag{2.4}
\end{aligned}$$

For maximum sensitivity, we choose x_0 so that $\cos\frac{4\pi}{\lambda}x_0 = 0$, which is verified when $x_0 = \frac{\lambda}{8} + k\frac{\lambda}{4}$, $k \in \mathbb{Z}$. Consequently we obtain a linearized interferometer output of the form:

$$P_r = P_{\text{avg}}\left[1 - \bar{V}\frac{4\pi}{\lambda}x(t)\right]. \tag{2.5}$$

The last expression shows that the maximum output swing as a response to the cantilever displacement $x(t)$ is obtained for optimal visibility $\bar{V}$. This is achieved when $R_1 = R_2$, resulting in $\bar{V}_{\text{max}} = 1$. In order to optimize the interferometer sensitivity, it is then important to match the two reflectivities. One can estimate R_2 from the material and thickness of the cantilever, and adjust R_1 by depositing a thin film of reflective material on the fiber cleave. For the interferometer employed in the experiments described in Chapters 3 and 4, we have deposited a layer of Si by thermal evaporation on the fiber cleaved end. Its reflectivity was monitored in remote during the deposition with a power meter, coupled to the fiber through the directional coupler. In order to match the estimated cantilever reflectivity $R_2 \approx 30\%$ [62], the deposited Si film reached a nominal thickness of 25 nm.

Adjusting the detector for maximum sensitivity involves either mechanically tuning the fiber-cantilever spacing, or, more simply, varying the laser wavelength. In the experiments described in this thesis, we have chosen the second approach, therefore employing wavelength-tunable laser sources. This technique eliminates the need for a mechanical actuator (PZT) to adjust the cavity length, resulting in enhanced stability and compact size [55]. A laser wavelength shift sufficient to center the interferometer fringe has been produced by either controlling the laser temperature with a thermoelectric cooler (TEC) (Chapters 3 and 4), or by fine tuning the laser cavity length (Chapter 5). This is achieved through a piezoelectrically actuated mirror, built in the laser commercial setup. In both cases, the interferometer is calibrated at the maximum sensitivity through the following procedure. From Eq. (2.5), it results that the interferometer response oscillates with a period $\lambda/2$. Therefore, in order to explore the full fringe swing, the laser wavelength is modulated at low frequency to a peak-to-peak amplitude slightly larger than $\lambda/4$. Then the wavelength is tuned in order to center the operating point of the interferometer, until the PD response shows a symmetrical behavior similar to that of Fig. 2.2. Note that the figure results slightly asymmetric because the operating point is not perfectly centered. This is due to a time drift of the laser wavelength or of the cavity size (or both). Such a drift, whatever the origin is, can be suppressed by stabilizing the interferometer operating point around P_{avg}, by means of a proportional-integral-derivative (PID) feedback loop controlling the laser wavelength.

The PD converts the interference signal into a voltage V_r proportional to P_r. Recalling the expression (2.5) for P_r and differentiating in x, we obtain the linearized interferometer gain

$$\left| \frac{\mathrm{d}V_r}{\mathrm{d}x} \right| = \frac{4\pi}{\lambda}\, V_{\mathrm{avg}}\bar{V} = \frac{2\pi}{\lambda}\left(V_{\mathrm{max}} - V_{\mathrm{min}} \right), \tag{2.6}$$

where V_{avg}, V_{max} and V_{min} are voltage signals proportional to the corresponding optical powers. Note that this relation is valid only for a low-finesse cavity ($R_1, R_2 \ll 1$), for a centered interferometer operating point and for small deflections of the cantilever, corresponding to small oscillations of V_r compared to the interference fringe amplitude. Therefore, we would like to emphasize once more the importance of locking the operating point with the PID controller to P_{avg}. In this way, during a displacement measurement, the cantilever modulates the interferometer response at the mechanical resonance frequency in a small range around the fringe average, where, by virtue of Eq. (2.6), the response is linear. Such an interferometer gain is equivalent to the transduction coefficient α introduced in Chapter 1. For an interferometer, α can thus be expressed in terms of the visibility $\bar{V}$, which is measurable directly from the interference fringe. Consequently, it is not necessary to re-
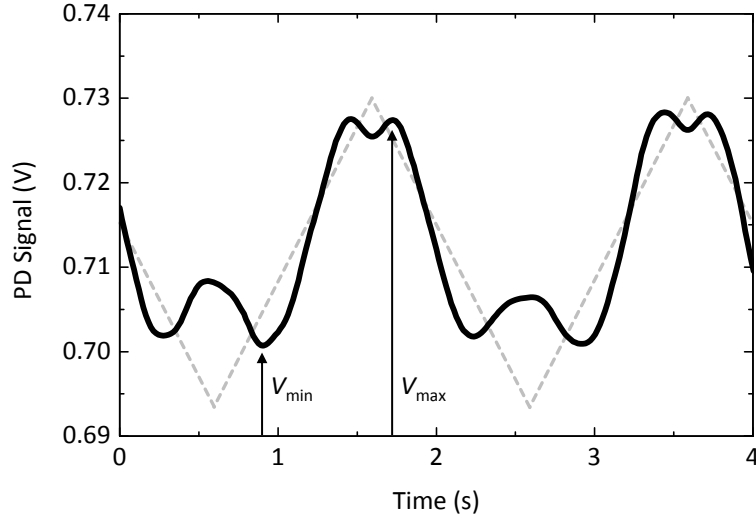
Figure 2.2 | **Interferometer's time trace.** PD response to a low-frequency laser wavelength modulation (dashed gray curve). The wavelength has been tuned in order to roughly center the operating point of the interferometer for maximum sensitivity and linearity. The data have been recorded in the experimental setup described in Chapter 5, which involves an interferometer with poor visibility and relatively high signal noise. Nevertheless, the graph represents an example of a typical interferometer time response.

trieve α as an additional parameter from the fit to the experimental data, of the voltage spectral density $S_V(\omega)$, expressed in Eq. (1.53). Furthermore, the accuracy of a displacement measurement is only limited by the determination of the laser wavelength and of the fringe extremes $V_{\max}$ and $V_{\min}$, and by the stability of the calibration set-point. In the measurements performed during the work of this thesis, the uncertainties on λ and on the set-point position were overtaken by the fluctuations of the PD signal δV. The uncertainty on α can then be written as:

$$\delta\alpha = \frac{2\pi}{\lambda}\left(2\times\delta V\right) = \frac{\alpha}{V_{\mathrm{amp}}}\,\delta V. \tag{2.7}$$

The PD signal $V(t)$ translates into a displacement $x(t) = V(t)/\alpha$, from which we can finally derive the uncertainty

$$
\begin{aligned}
\delta x &= \frac{\delta V}{\alpha} + \frac{|V|}{\alpha^2}\,\delta\alpha \\
&= \frac{\delta V}{\alpha}\left(1 + \frac{|V|}{V_{\mathrm{amp}}}\right) \\
&\approx \frac{\delta V}{\alpha},
\end{aligned}
\tag{2.8}
$$

the last passage relying on the hypothesis of small signal oscillations. This relation acquires particular importance for the interferometer described in

Chapter 5, characterized by a relatively high signal noise δV, which directly affects the uncertainty on the resonator's position δx.

Since the fiber-optic interferometer is a Fabry-Pérot cavity, its response is an oscillating signal not only as a function of the cavity length l, but also as a function of λ, with a period called the *free spectral range* (FSR) of the cavity. From a measurement of the FSR, it is possible to precisely obtain the cavity length, through the following relation [63]:

$$l = \frac{\lambda^2}{2n_{\mathrm{r}}\mathrm{FSR}},\tag{2.9}$$

where n_{r} is the refraction index of the medium in the cavity.

To conclude this section, we would like to remark an important experimental aspect, anticipated in Chapter 1. For practical reasons, it is often not possible to focus the interferometer laser directly on the position of maximum displacement of the cantilever, i.e. at its free end. This is the situation described in Chapters 3 and 4. Therefore, the oscillation amplitude $x_{\mathrm{osc},n}$ cannot be measured directly, but can be retrieved from the knowledge of the cantilever mode shape function $u_n(z)$, through the previously described equation (1.36).

2.1.1 Limits to the Interferometer Sensitivity

The sensitivity of the fiber-optic interferometer as a displacement transducer is ultimately limited by the PD shot noise [52]. The photo-current is proportional to the power P_r incident on the PD through the responsivity S, which is in our case equal to 0.8 A/W. The average shot noise current is then given by:

$$I_{\mathrm{shot}} = \sqrt{2eSP_{\mathrm{avg}}\Delta\nu},\tag{2.10}$$

where e is the electron charge and $\Delta\nu$ is the detection bandwidth. The SNR – between average photo-current and shot noise – thus improves as the square root of the laser power. The root-mean-squared equivalent noise displacement corresponding to a SNR equal to one is

$$\frac{x_{\mathrm{noise}}}{\sqrt{\Delta\nu}} = \frac{\lambda}{2\pi}\sqrt{\frac{e}{2S\bar{V}P_{\mathrm{avg}}}}.\tag{2.11}$$

Assuming optimal visibility ($\bar{V} = 1$) and a laser power $P_{\mathrm{avg}} = 20$ nW at $\lambda = 1550$ nm, the equivalent noise displacement is of the order 10^{-12} m Hz$^{-1/2}$. This value expresses the sensitivity reached by the interferometer realized for the work of this thesis, as shown in Fig. 1.11. A limitation to the maximum power – and then to the sensitivity – comes from the low temperatures often required in ultra-sensitive force microscopy. In fact, for temperatures below 1 K, the interferometer laser has been observed to heat Si

cantilevers through light absorption, presumably due to crystal impurities, even for incident power below 100 nW [64, 65]. Interferometers compatible with ultra-low temperatures have been developed using microwave radiation. In particular, using this approach, Teufel and co-workers have demonstrated a sensitivity below that at the standard quantum limit, in their case of the order 10^{-15} m Hz$^{-1/2}$ [5, 12]. Thereafter, Anetsberger *et al.* have coupled in the near-field an infra-red laser homodyne interferometer to a nanomechanical resonator, achieving sub-SQL imprecision even at room temperature $(< 10^{-15}$ m Hz$^{-1/2})$ [6].

Different interferometric techniques, employing high-finesse cavities, have been able to push the sensitivity down to the impressive value of 10^{-20} m Hz$^{-1/2}$, achieving nearly quantum-limited displacement detection [66, 67]. However, their application to micro- and nanomechanical resonators results challenging [54]. In fact, a fundamental obstacle to interferometric detection is imposed by the optical diffraction limit, which sets a lower bound on the size of the measured resonator to the scale of the used wavelength. In this context, enhanced reflectivity from Si NW cantilevers has been obtained when the incident light is polarized along the NW axis [68]. In addition, a high-finesse cavity requires highly reflective mirrors, typically involving thick substrates and stiff multilayer stacks. Such characteristics compete with the usual requirement of low spring constant of micro- and nanoelectromechanical systems. Another limitation to these approaches comes from the aforementioned resonator heating encountered at low temperatures and high laser power.

2.2 Quantum Point Contact

The perspective of observing the zero-point motion of a resonator and testing quantum laws on a mechanical object has motivated the search for ultra-sensitive displacement detectors, possibly overcoming the limitations of interferometry or offering other advantages in technological applications. Alternative approaches consist in transducers relying on the mechanical modulation of charge flow, through a single electron transistor (SET) [69–71] or an atomic point contact [72]. These devices have reached sensitivities around 10^{-15} m Hz$^{-1/2}$, approaching, in the experiment of LaHaye *et al.*, the SQL [71]. However, all these detectors are integrated into a single unit with the resonator they measure. This aspect strongly limits their versatility for some force-sensing applications.

An innovative scheme was introduced by Poggio and collaborators, where a charge flow sensor and the mechanical resonator modulating this charge are placed off-board [54]. Such an approach is advantageous because it is in prin-

ciple compatible with an arbitrary nano-sized resonator, even smaller than the optical diffraction limit. For instance, this detector could be used in conjunction with sensitive cantilevers in a variety of force-sensing applications, including MRFM.

The detector used by Poggio *et al.* is a quantum point contact [73, 74], a device widely used for high-resolution charge sensing. For example, a QPC had already been used to detect single electrons in gate-defined quantum dots (QDs) [75] and to detect charge motion and controllably introduce quantum decoherence in a *which-path* electron interferometer [76, 77]. A QPC has also been demonstrated as a scanning charge-imaging sensor, enabling the direct observation of coherent electron flow through the QPC. This is conventionally known as scanning gate microscopy (SGM) [78, 79]. Taking advantage of the piezoelectric effect, a QPC has been used to probe vibrational modes of the host substrate, a macroscopic three-dimensional GaAs crystal [80]. Finally, Cleland *et al.* have applied a QPC to measure mechanical motion at the nano-scale, demonstrating a sensitivity of the order 10^{-12} m Hz$^{-1/2}$ [81]. The resonator is a doubly-clamped beam made out of a single-crystal GaAs heterostructure, with a resonance frequency of 1.5 MHz. The coupling mechanism relies again on the piezoelectric effect in GaAs, which translates into a modulation of the current flowing into a QPC integrated within the resonator. This method therefore requires a built-in approach, like the other charge-flow detectors mentioned before. The fabrication of a QPC integrated with a piezoelectric resonator can degrade both the electron mobility in the heterostructure and the quality factor of the resonator. Furthermore, the stiff doubly clamped geometry and the requirement that the resonator has to be made from a single-crystal GaAs heterostructure limit its application as a sensitive force detector.

Another technique to measure the displacement of a nano-resonator with an off-board detector involves the use of a superconducting quantum interference device (SQUID). The SQUID is widely known as a sensitive magnetic field sensor. In this context, a magnetic particle attached to a cantilever in close proximity to the SQUID modulates the magnetic flux in the device as a consequence to the cantilever's vibration. This SQUID-mediated magneto-mechanical coupling allowed Vinante *et al.* to demonstrate a displacement sensitivity of the order 10^{-13} m Hz$^{-1/2}$ [82]. In the same experiment, the coupling mechanism was used to cool the resonator's effective temperature from a bath below 100 mK, down to 160 µK. Limitations of this approach include the need of a cantilever functionalized with a magnet, thus competing with the requirements of low spring constant and high quality factor necessary to achieve quantum limited displacement resolution and ground state cooling.

In the next subsections, we define and develop the key concepts underlying the operation of a QPC and introduce its application to the detection and

control of mechanical motion. The latter is the main topic of Chapters 3 and 4.

2.2.1 Conductance Quantization

A QPC is a mesoscopic electronic device formed by a short one-dimensional channel connected adiabatically to large source and drain reservoirs. The device is realized in the form of a narrow constriction in a two-dimensional electron gas (2DEG), whose width can be adjusted by the application of electrostatic potentials. The QPC represents the first experimental demonstration of *conductance quantization* in one-dimensional electron transport at zero magnetic field, thanks to the contemporary 1988 works of van Wees and collaborators [73] and Wharam and collaborators [74]. In fact, the source-drain conductance in a QPC is a stepwise function of the constriction width, quantized in units of $2e^2/h$, as shown in Fig. 2.3. Conductance quantization requires ballistic quantum transport, which is realized when the width W and the length L of the QPC constriction are much smaller than both the electron coherence length l_ϕ and mean free-path l_e in the 2DEG, and at the same time comparable or a few times larger than the Fermi wavelength λ_F [83]:

$$\lambda_F \leq W, L \ll l_\phi, l_e. \tag{2.12}$$

The condition $W, L \ll l_\phi, l_e$ ensures that the motion of the electrons in the QPC is completely determined by the electrostatic potential applied to the constriction, and no scattering occurs with phonons or impurities [84]. Modern lithographic techniques, together with measurements at cryogenic temperatures and advances in the growth of high-mobility 2DEGs ($l_e > 100\,\mu\text{m}$ [85]) have made this regime easily accessible. On the other hand, the long Fermi wavelength in a 2DEG ($\lambda_F \approx 40$ nm [85]), compared to the one in a metal (order of Å), allows the observation of quantum behavior [83, 84].

Considering a reference system xyz with energy confinement in the z direction (due to the 2DEG), the quantization of conductance can be explained assuming the electrons in the QPC being governed by a model Hamiltonian of the kind:

$$\hat{H} = \frac{\hat{p}_x^2}{2m^*} + \frac{\hat{p}_y^2}{2m^*} + e\left[V_0 + \hat{V}(y)\right], \tag{2.13}$$

where $\hat{p}_x$ and $\hat{p}_y$ are the electron momentum operators along x and y, m^* is the electron effective mass in the 2DEG, V_0 is the electrostatic potential in the QPC, and $\hat{V}(y)$ is the operator of the lateral confining potential of the constriction as a function of the direction y perpendicular to the transport. We do not include in the Hamiltonian the longitudinal potential $\hat{V}(x)$, describing the transition from the wide 2DEG reservoirs to the QPC. The
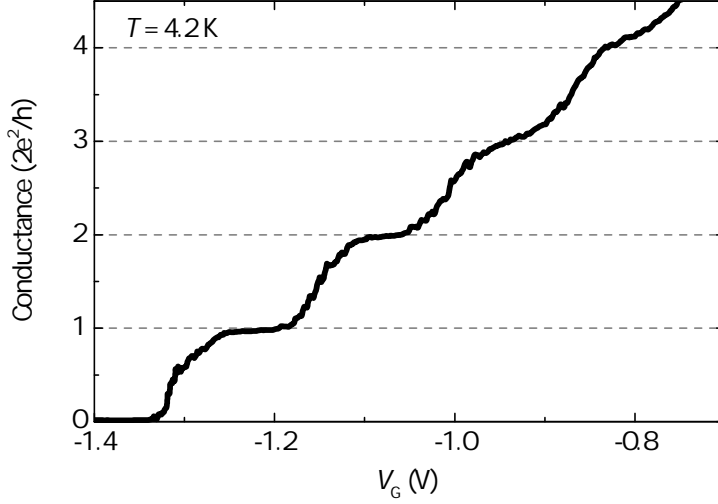
Figure 2.3 | **Quantized conductance in a QPC.** The conductance in a QPC, as a function of the electrostatic potential V_G controlling the constriction width, exhibits a quantized behavior, in steps of $2e^2/h$. The finite temperature $T = 4.2$ K is responsible for the smoothing of the steps. A background series resistance $R_b = 2.7$ kΩ has been subtracted from the raw data, following the procedure described in the text. The data have been recorded from a twin of the device described in Chapter 3.

reason is that $\hat{V}(x)$ can be decoupled from $\hat{V}(y)$ for a smooth (*adiabatic*) transition, on the scale of λ_F, into the wide 2DEG regions [86, 87]. We consider for the lateral direction a parabolic potential $\hat{V}(y) = \frac{1}{2}m^*\zeta_0^2\hat{y}^2$, where ζ_0 indicates the strength of the lateral confinement [84]. This potential leads to the quantization of the lateral motion, and the formation of one-dimensional sub-bands, each corresponding to a different transport channel. In fact, the Hamiltonian (2.13) assumes the form of a harmonic oscillator, with eigenenergies [84]:

$$E_N(k_x) = \frac{\hbar^2 k_x^2}{2m^*} + \hbar\zeta_0\left(N - \frac{1}{2}\right) + eV_0. \qquad (2.14)$$

Here $N = 1, 2, 3, \dots$ is the index of the one-dimensional channels and k_x is the wave number for the propagation across the QPC. Such a dispersion relation is illustrated in Fig. 2.4. In equilibrium and at low temperature, the electron states are occupied up to the bulk Fermi energy E_F. The effect of an electrostatic potential V_G controlling the constriction width is twofold: it raises V_0 and increases the confinement ζ_0 and thus the sub-band energy separation $\hbar\zeta_0$. Both effects result in a reduction of the number of occupied sub-bands, i.e. those with energy below E_F [84].

The application of a weak source-drain potential V_{sd} (below $k_B T/e$ to prevent electron heating) lifts the number of occupied states in the source
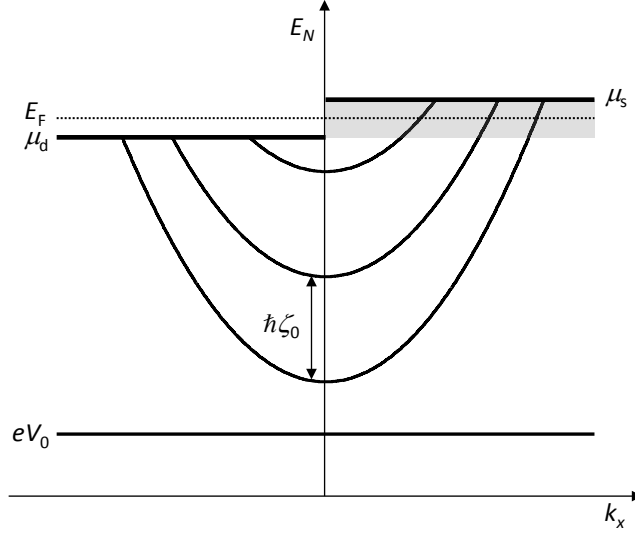
Figure 2.4 | **Energy dispersion of one-dimensional sub-bands in a QPC.** In equilibrium and at low temperature, the sub-bands are occupied up to the bulk Fermi energy E_F. An applied source-drain voltage creates a difference $eV_{sd} = \mu_s - \mu_d$ between the chemical potentials of the reservoirs. This causes a net current, from the states in the shaded area in the figure, to flow across the QPC.

and drain reservoirs up to their respective chemical potentials μ_s and μ_d, so that $\mu_s - \mu_d = eV_{sd}$. We assume that the electron states in the source have positive group velocity $v_N = (1/\hbar)dE_N/dk_x$, while those in the drain have negative group velocity $-v_N$. This is equivalent to assuming that no reflection occurs at both ends of the channel [84]. The source-drain potential causes a net current I to flow across the QPC, carried by the uncompensated states in the energy interval $\mu_s - \mu_d$:

$$I = e \sum_{n=1}^{N_c} \int_{\mu_d}^{\mu_s} \frac{1}{2}\rho_N(E)v_N(E)\,\mathrm{d}E. \tag{2.15}$$

In this formula, the sum runs over the N_c occupied sub-bands, ρ_N is the density of states of a one-dimensional system, and the factor $1/2$ in front of it accounts for considering states propagating in one direction only. Including spin degeneracy, the density of states is $\rho_N = 2\pi \left(dE_N/dk_x\right)^{-1}$. The product of ρ_N and v_N is thus independent of both energy and sub-band index N, and equal to $4/h$. This constitutes the key of conductance quantization in one-dimensional transport. In fact, the conductance $G = I/V_{sd}$ reads:

$$G = \frac{2e^2}{h}N_c. \tag{2.16}$$

In conclusion, this relation means that each occupied sub-band contributes

$G_0 \equiv 2e^2/h \approx (12.9 \text{ k}\Omega)^{-1}$ to the conductance of a one-dimensional system. Finite temperature has the effect of smearing the conductance steps, because of the Fermi-Dirac distribution of the sub-band occupancy index N [88]. Note that, although Eq. (2.16) has been obtained for the special case of a parabolic lateral confinement $\hat{V}(y)$, its validity holds for any shape of the potential [88]. The reason lies in the fundamental cancellation of the energy dependence of the one-dimensional density of states ρ_N with that of the group velocity v_N, regardless of the form of the dispersion relation (2.14).

In the beginning of this sub-section, we have assumed ballistic quantum transport in a QPC device. This would imply that all the electrons injected into a QPC get transmitted with no resistance. Instead, most of them are scattered back from the QPC potential barrier, giving rise to the observed non-zero resistance $1/G_0$. In a real device, however, this is not the only source of resistance. The 2DEG is electrically contacted by means of *ohmic contacts* [89]. These are metallic contacts which are annealed during fabrication in order to diffuse into the heterostructure forming the 2DEG. This has the effect of reducing the Schottky barrier arising from the metal/semiconductor interface, resulting in an ohmic behavior for the contact resistance, even at low temperatures. Such a resistance adds in series to the QPC internal resistance and can be measured directly from the device when the QPC constriction is completely open ($V_G = 0$), or can be excluded in case of a 4-wire measurement [90]. Other sources of resistance depending on the geometry of the QPC are also present, as explained in detail in Ref. [88]. However, these additional series resistances are difficult to isolate and cannot be excluded by a 4-wire measurement. Therefore, a general estimation procedure consists in subtracting from the measured device resistance $R_{\text{QPC}}(V_G)$ the total background resistance R_b, treated as an adjustable parameter [88]. R_b is chosen so that for one constant value, the conductance $G(V_G) = [R_{\text{QPC}}(V_G) - R_b]^{-1}$ matches the quantized plateaus (2.16), as in Fig. 2.3.

The application of an external magnetic field to a QPC does not turn off the quantization. The main effect is to reduce the number of plateaus in a given interval of V_G. This happens because the magnetic field increases the lateral confinement, causing a depopulation of the one-dimensional sub-bands [88]. In addition, the quantization becomes steeper, because the magnetic field spatially separates the electron channels with opposite wave number at opposite edges of the constriction, thus reducing the probability of backscattering. Finally, a strong magnetic field lifts the spin degeneracy of the sub-bands, resulting in additional plateaus at odd multiples of e^2/h (as shown, for example, in Fig. 4.2). Even the formation of Hall states at high field does not alter the quantization, but the resulting oscillations of the longitudinal resistance entail a variation of the background resistance R_b, with respect to the zero-field situation.

2.2.2   QPC as Displacement Transducer

The quantum origin of the non-linear conductance makes a QPC particularly suitable for sensing applications. In fact, when the QPC is biased at the transition between two conductance plateaus, it becomes very sensitive to small perturbations of the local electrostatic potential. If the potential landscape around the QPC is modulated by mechanical vibrations of a nearby resonator, then the QPC can be used as a displacement detector. The current flowing through it will carry a spectral signature of the resonator's vibrational modes. Such a current is proportional to the displacement through the coupling coefficient α, this time expressed in terms of A/m. α follows the derivative of the conductance G with respect to V_{G}, therefore exhibiting an oscillatory behavior as a function of V_{G}, with maxima aligned to the steps in G [54]. Although the performance of QPC transducers is in practice limited by device imperfections, its optimization should fulfill the conditions for reaching quantum limited resolution [91, 92].

In Chapters 3 and 4, we describe the electrical characterization of QPC devices fabricated with two different techniques, and we report on their performance as displacement transducers. Furthermore, the high sensitivity of the QPC in Chapter 3 has been employed to control the motion of an off-board cantilever, achieving a cooling of its fundamental mode effective temperature, several times below the temperature of the bath.

3 | Feedback Cooling of Cantilever Motion Using a Quantum Point Contact Transducer

As reported in the previous chapter, the displacement of a nanomechanical resonator can be measured with an imprecision down to the standard quantum limit of continuous position detection. Such exquisite resolution enables the observation of quantum effects on the resonator [12–15] and the fine control of its motion, by both tuning its linear dynamic range [93] and manipulating its time response [32].

The prospect of quantum control over a mechanical resonator involves its preparation near its quantum ground state. In this chapter, we investigate an innovative displacement detection technique, which makes use of a QPC transducer included in an active feedback loop. Such a loop is designed to cool the fundamental mechanical mode of an off-board micro-sized cantilever. We show that the minimum achieved effective mode temperature of 0.2 K and the displacement sensitivity of 10^{-11} m Hz$^{-1/2}$ are limited by the performance of the QPC as a one-dimensional conductor and by the cantilever-QPC capacitive coupling. The experimental results described in this chapter have been published as:

[33] Montinaro, M., Mehlin, A., Solanki, H. S., Peddibhotla, P., Mack, S., Awschalom, D. D., and Poggio, M. *Applied Physics Letters* **101**, 133104 (2012).

3.1 Cooling a Nanomechanical Resonator

The most direct approach for reaching the quantum ground state of motion consists in cooling a high-frequency resonator ($\omega_0/(2\pi) > 1$ GHz) with a dilution refrigerator ($T \approx 25$ mK) [15]. In this way, the mode thermal occupancy

$N_{\mathrm{mode}} \approx k_{\mathrm{B}}T/\hbar\omega_n$ is reduced below unity, which means that the resonator is mostly found in its ground state. In fact, using this approach, O'Connell and coworkers have been able to cool a 6-GHz resonator to $N_{\mathrm{mode}} < 0.07$ and to controllably create single phonons in the resonator [15]. Alternatively, in case of a lower-frequency resonator, or higher bath temperature, a cooling technique has to be applied in order to reduce the resonator's effective temperature T_{eff} below the one of the bath, or to just control the temperature T_{mode} of a single mode. In this context, experimentalists have developed three different approaches, namely *back-action*, *sideband*, and *active feedback* cooling.

The back-action cooling technique exploits the force noise due to the influence of the detector on the resonator (see Section 1.6.2). The latter is usually included in a resonant optical cavity, where it is subject to radiation pressure, able to damp its motion. In Section 1.6.1, we show that the resonator's temperature is proportional to its Brownian motion. Therefore, reducing that motion is equivalent to cooling the resonator. In a back-action cooling scheme, the cooling efficiency depends on the strength of the coupling between the mechanical object and the optical field in the cavity. This is in turn related to the intensity of the field. Using this method, Arcizet *et al.* have been able to cool a doubly-clamped beam from room temperature down to 10 K [94].

The sideband-cooling scheme also involves an oscillator in a resonant cavity. The oscillator's motion modulates the cavity length, thus mixing its resonance frequency with the optical frequency of the light in the cavity. The spectrum of the transmitted light results then affected by two sidebands centered around the cavity resonance and spaced from it by the oscillator's mechanical resonance. The process is analogous to the generation of Stokes and anti-Stokes sidebands in Raman scattering. A drive field red-detuned below the cavity resonance is able to remove energy from the motion. The mechanical oscillator is then damped and cooled by way of this radiation-pressure force. Using this scheme, Teufel *et al.* have reached $N_{\mathrm{th}} = 0.34$ and have achieved coherent coupling between the microwave photons in the cavity and the phonons in the resonator [12].

Active feedback cooling relies on the fine measurement of the resonator's displacement, realizing a transduced signal which is fed back to the resonator via an external loop. By controlling the phase and amplitude of this signal, the resonator's motion can be amplified or suppressed. Unlike back-action and sideband cooling, feedback cooling is particularly well-suited to the ultra-soft low-frequency cantilevers typically used in sensitive force measurements. The minimum phonon occupation number achieved by this method depends only on the transducer's displacement imprecision and the resonator's thermal noise [32]. As a result, a widely applicable transduction scheme with low

displacement imprecision has the potential to prepare resonators in quantum states of mechanical motion. In addition, feedback cooling allows the regulation of the time response of soft cantilevers [32], and can be used to modify or suppress the non-linearity of resonator's motion [95].

3.2 The QPC Transducer

Fine control of resonator's motion requires sensitive displacement detection. Here we investigate one such technique: the use of a QPC as a detector of cantilever motion and its application to reduce the effective temperature of the cantilever's fundamental mode. As illustrated in Section 2.2, the QPC transducer works by virtue of the strong dependence of its conductance on disturbances of the nearby electric field by an object's motion. In particular, a QPC is advantageous due to its versatility as an off-board detector, its applicability to nanoscale oscillators, and its potential to achieve quantum-limited detection [91,92]. Most other displacement detection schemes require the functionalization of mechanical resonators with electrodes, magnets, or mirrors [18]. These requirements tend to compete with the small resonator mass and high quality factor necessary to achieve low thermal noise and high coupling strength to the detector. Since all resonators disturb the nearby electric field, the QPC transducer, in principle, requires no particular functionalization. The coupling of a mechanical resonator to a QPC device is also interesting as one of a series of new hybrid systems coupling mechanical resonators with microscopic quantum systems, as illustrated also in Chapters 4 and 5. In particular, such a system may be the first step towards coupling a resonator with an off-board quantum dot, in an approach aimed at the quantum control of mechanical objects, precision sensing, and quantum information processing [37].

3.2.1 QPC Fabrication

The QPC employed in this experiment has been fabricated within the work of this thesis. It is made from a GaAs/AlGaAs heterostructure, which has been designed for obtaining a two-dimensional electron gas (2DEG) very close to the wafer surface, still maintaining a high electron mobility. The use of a shallow 2DEG is aimed at achieving a stronger capacitive coupling between the QPC and the cantilever.

The heterostructure has been grown by molecular-beam epitaxy (MBE) on a (001) GaAs substrate; the structure consists of a 600-nm GaAs layer grown on top of the substrate, followed by 20-nm $Al_{0.25}Ga_{0.75}As$, a Si delta-doped layer, 40-nm $Al_{0.25}Ga_{0.75}As$ and finally a 5-nm GaAs cap. The 2DEG
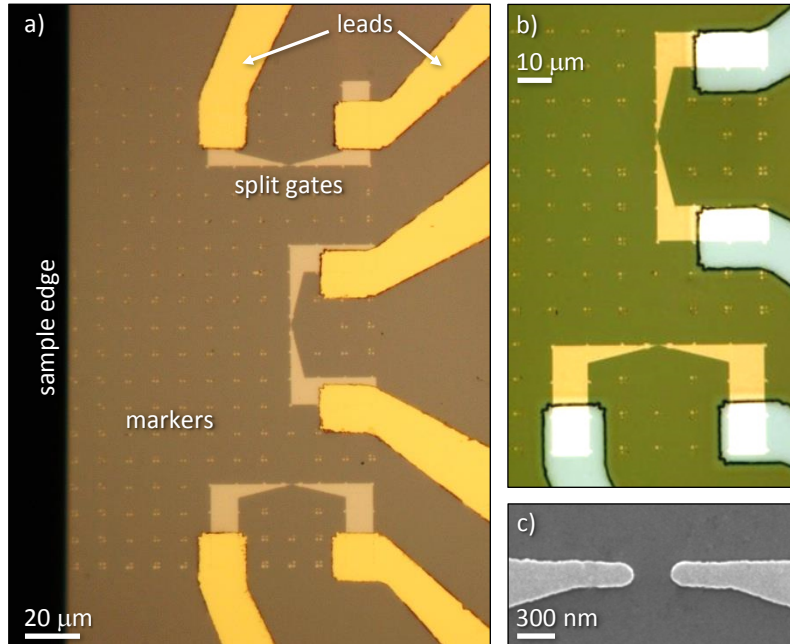
Figure 3.1 | **QPC displacement detector.** (a) Optical micrograph of a sample containing three QPCs in different orientations with respect to the oscillation direction of the cantilever. The sample has been processed in order to obtain devices within $100\,\mu m$ of the sample edge. (b) Optical micrograph showing two QPCs and the markers in binary code used for the alignment of the cantilever. (c) Scanning electron micrograph of the active region of a QPC, showing the split gates separated by a 300-nm gap.

forms at the GaAs/AlGaAs interface, situated only 65 nm below the surface. It is characterized by a carrier density $n = 2.5 \times 10^{11}\ \mathrm{cm}^{-2}$ and mobility $\mu = 10^5\ \mathrm{cm^2V^{-1}s^{-1}}$ at $T = 4.2$ K.

The fabrication of the QPC consists of several lithographic steps, which have been designed in order to obtain a device close to an edge of the sample, as shown in Fig. 3.1(a). The reason is that the cantilever motion is also independently detected via a fiber-optic interferometer, as described later. The cantilever is aligned above the QPC and the interferometer laser is focused through a collimating lens on an area close to the cantilever's tip. Therefore, a QPC close enough to the edge avoids laser light scattering from the sample corner, which would degrade the interferometer visibility.

The detailed fabrication protocol of the QPC is schematized in Appendix A. It is articulated in a succession of process stages summarized in the following.

Mesa. In a first stage, a *mesa* pattern is defined on the sample via ultra violet lithography (UVL). Thereafter, the material outside the mesa pattern

is etched away, thus isolating different devices.

Ohmic Contacts. A second UVL process defines ohmic contacts, which establish an electrical interface between the 2DEG and the measurement apparatus. The contacts are made through the thermal deposition of several metallic layers. The deposition follows a careful removal of organic residuals from the sample surface, by means of oxygen plasma etching, and of the GaAs native oxide, by means of HCl wet etching. Then the contacts are deposited, in the sequence Ni/Ge/Au/Ni, with thickness 2/26/54/15 nm. The first Ni thin film has been demonstrated to improve the consistency and uniformity of the contacts [89]. It reacts with the GaAs of the substrate to form clusters of NiGa and NiAs. These compounds act as a diffusion barrier, preventing the spiking into the sample of excessive Au from the upper layer [96]. The deposition of Au and Ge in this specific thickness ratio allows the formation of an eutectic alloy which melts at lower temperature with respect to other alloy compositions. As mentioned in Section 2.2.1, in fact, a successive annealing stage allows the diffusion of the AuGe alloy into the 2DEG and the formation of the ohmic contacts. The topmost Ni film acts as a wetting layer, facilitating the penetration of AuGe into the sample. Its thickness has to be chosen in a specific ratio with respect to the Ge and Au layers, for lower contact resistance. Optimal results have been obtained with a ratio of 0.25 or lower [97, 98], with a contact resistance below $200\,\Omega$ at 4.2 K, realized during the work of this thesis [99]. The total contact thickness of 97 nm is chosen for being larger than the 2DEG distance from the surface.

Split Gates. In the next stage, electron-beam lithography is used to define split gates, which are the basis for the formation of the QPC constriction within the 2DEG. Thermal deposition of Ti/Au (5/15 nm) and lift-off define a gap between the gates about 300 nm wide. The application of a negative electrostatic potential V_G between the gates and the underlying 2DEG forms a variable-width channel through which electrons flow. An SEM image of this active region of the QPC is shown in Fig. 3.1(c).

Leads. A last UVL stage and thermal deposition are used to pattern Ti/Au (10/130 nm) leads, which electrically connect the split gates to the ohmic contacts.

Cleaving and Bonding. Finally, the sample is carefully cleaved in order to obtain devices within $100\,\mu$m of the sample edge, as in Fig. 3.1(a). Thereafter, the sample is glued to a customized chip-carrier (produced by CMR-Direct), which ensures easy optical access and positioning of the cantilever.
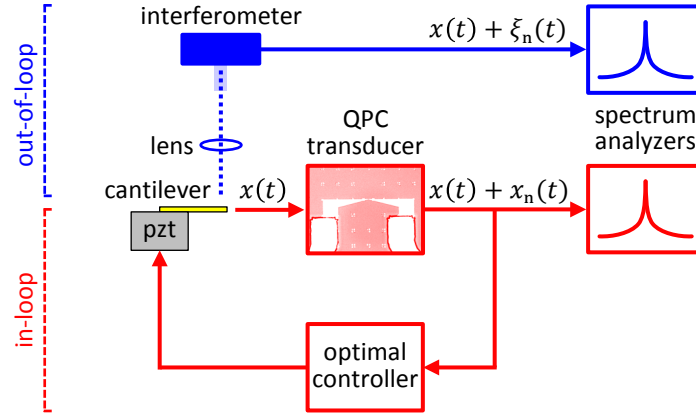
Figure 3.2 | **Schematic diagram of the experimental setup.** In the red loop, the motion of the cantilever is transduced by a QPC and amplified by an optimal controller, before being sent to a piezoelectric element mechanically coupled to the cantilever. The motion is also independently detected by an out-of-loop fiber-optic interferometer, shown in blue.

Au-bonding of the sample contacts to the chip-carrier completes the processing.

3.3 Experimental Setup

The experimental setup designed for this work is shown schematically in Fig. 3.2: the QPC transducer generates an electrical signal proportional to the cantilever displacement; such a signal is then amplified by a digital optimal controller [100, 101] and sent to a piezoelectric element mechanically coupled to the cantilever. We choose the phase of the optimal control feedback such that the cantilever oscillation is damped. We demonstrate the possibility of damping the thermal noise spectrum of the resonator below the QPC measurement noise floor, which is close to the shot noise level. Such an effect has already been demonstrated for an opto-electronic loop [32, 102–104] and is known as intensity noise *squashing*. In such a regime, the effect on the motion of the resonator can be further validated using a second transducer outside the feedback loop. In this work, such an out-of-loop measurement has been carried out by means of a low-power laser interferometer, of the kind described in Section 2.1.

The complete experimental setup is shown in Fig. 3.3. While the QPC is described in detail in Section 3.2.1, in the following subsections the other components of the setup are presented. A scheme of the control and acquisition electronics is provided in Appendix B.
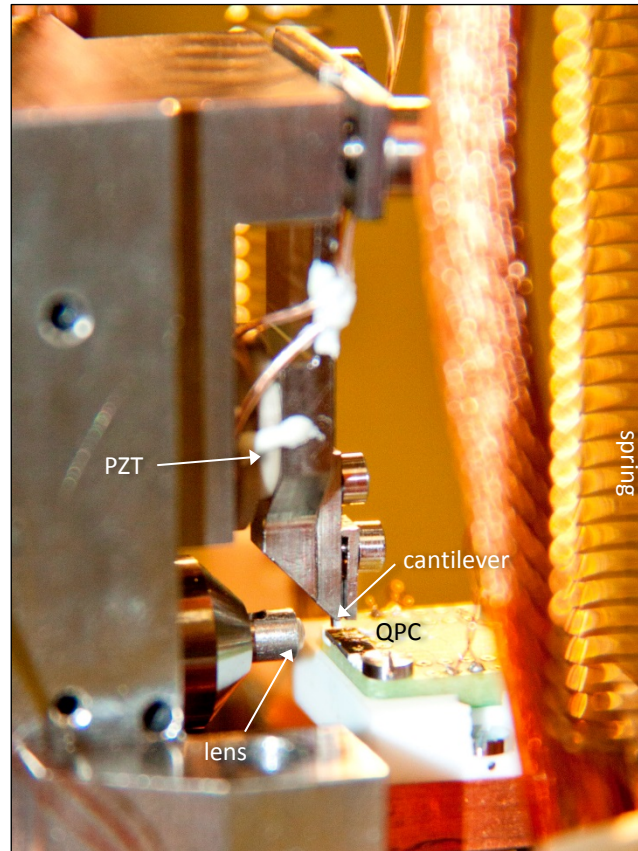
Figure 3.3 | **Experimental setup.** The picture shows part of the interferometer cavity formed between the cleaved facet of an optical fiber and the cantilever. The latter is aligned above a QPC device, fabricated in proximity to the sample edge.

3.3.1 Cantilever

We use a micro-sized cantilever as a mechanical resonator coupled to the QPC detector. It is produced by NanoWorld AG (model Arrow TL1) from monolithic silicon, which is highly doped to make it conductive. The detailed geometry of the cantilever is described in Section 1.5.1, which provides a finite element model of its lowest four mode shape functions. For this experiment, the cantilever tip has been metallized with Ti/Au (10/30 nm), in order to reduce the non-contact friction produced by the interaction with the QPC sample surface [105]. Due to the cantilever conductivity, a voltage V_{L} can be applied to its tip by contacting the base of the cantilever chip.

At $T = 4.2$ K, the cantilever has a fundamental resonance frequency $\omega_0/(2\pi) = 7.9$ kHz. The corresponding quality factor Q_0 has been measured through a *ring-down* technique, which consists in mechanically exciting the

cantilever with a coupled piezoelectric transducer, and measuring the natural decay of its oscillation amplitude. Such a decay follows an exponential behavior, whose argument is inversely proportional to the quality factor. By fitting the data, we find $Q_0 = 2.0 \times 10^5$. In order to determine the cantilever's spring constant k_0, its thermal noise spectrum is measured at several different bath temperatures. Assuming the resonator's effective temperature to be in equilibrium with the bath, k_0 is calculated by inverting Eq. 1.54. The result is $k_0 = 2 \times 10^{-3}$ N/m.

3.3.2 Cryostat and Magnetic Field

The cantilever and QPC are mounted in a vacuum chamber with pressure below 10^{-6} mbar at the bottom of a ^{4}He cryostat ($T = 4.2$ K). To ensure isolation from environmental vibrations, the cryostat is attached to a compressed-air suspended table and the sample stage is suspended on springs (as shown in Fig. 3.3). A three-dimensional positioning stage with nanometer precision and stability (Attocube) moves the QPC relative to the cantilever.

A 2-T magnetic field, perpendicular to the QPC surface, is applied from a superconducting magnet, in order to suppress the backscattering of electrons in the conductance channel. As explained in Section 2.2.1, this precaution provides a steeper conductance quantization, thus improving the sensitivity of the QPC to the cantilever's vibrations.

3.3.3 Interferometer

As mentioned before, the cantilever displacement is detected also outside the QPC feedback loop, by means of a low-power fiber-optic interferometer. The interferometer setup is of the kind described in Section 2.1 and schematized in Fig. 2.1. It essentially consists of a temperature-tuned 1,550-nm distributed feedback laser diode, emitting 20 nW of light, which is focused onto a region at $\approx 90\,\mu$m from the cantilever tip and then reflected back onto the cleaved end of an optical fiber. For matching the cantilever's reflectivity, the fiber end is coated with 25 nm of Si, through the procedure described in Section 2.1.

3.3.4 Optimal Controller

A digital optimal controller amplifies and delays the transduced signal in the feedback loop. Optimal cantilever control has been modeled and developed by the group of J. A. Sidles for improving the time response of force microscopy cantilevers, for application in particular to MRFM [100, 101].

Figure 3.4 | **Scanning probe micrograph of the QPC.** The image shows the QPC split gates and is obtained by using the cantilever as a non-contact AFM probe, situated $z = 80$ nm above the sample surface. Data were processed with WSXM software [106].

In this work, optimal control is used for damping the cantilever motion without affecting its intrinsic properties. The controller is implemented on a field programmable gate array (FPGA), which generates a transfer function based on the measured cantilever characteristics (ω_0, Q_0, k_0, thermal force noise, measurement noise). It offers optimal performance especially at large damping, when the cantilever displacement spectrum gets pushed down to the level of the measurement noise [62].

3.4 Operation

In order to find the optimal operating position, the QPC sample is moved close to the cantilever tip, by controlling the positioning stage. We are able to gently move the sample against the cantilever until touching: thanks to its softness, in fact, the cantilever does not suffer of any damage. Thereafter, retracting the sample, we are able to measure directly its distance from the cantilever tip. The proximity to the sample enables the cantilever to probe the electrostatic force arising from its interaction with the surface, in a similar way to non-contact atomic force microscopy (AFM). This force produces a variation of the cantilever resonance frequency. By recording this frequency shift as a function of position, while scanning the cantilever relative to the sample, we detect the sample topography, as shown in Fig. 3.4. The cantilever is then positioned with its tip about 80 nm above the QPC, as shown schematically in Fig. 3.5. This distance is chosen in order to minimize the electrostatic interaction, which gives rise to non-contact friction [105].
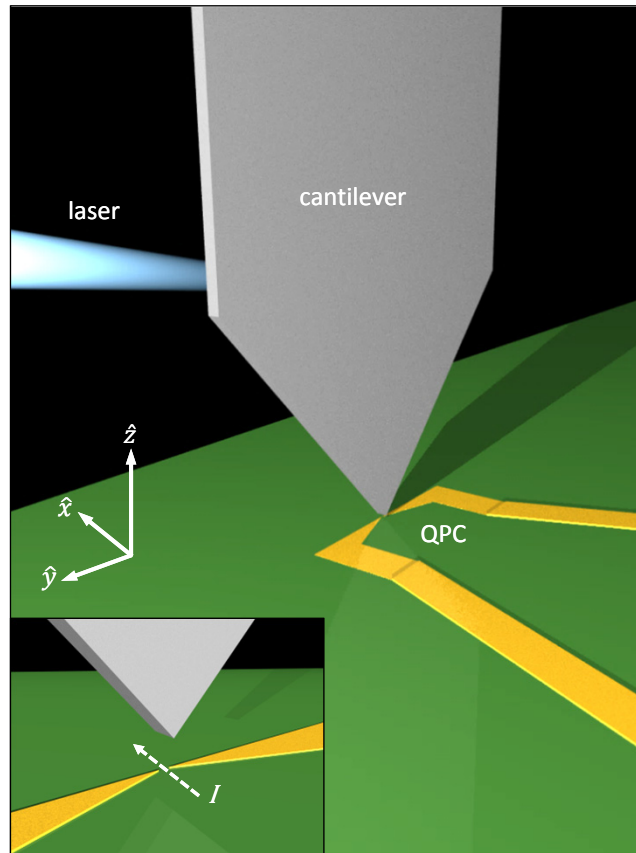
Figure 3.5 | **Schematic picture of the experimental setup.** The inset is a zoom-in of the QPC active region, showing the close proximity to the cantilever's tip. A source-drain voltage, applied to ohmic contacts on either side of the split gates, drives a current I through the QPC.

3.4.1 Measurement of Cantilever Thermal Motion

Owing to the proximity of the cantilever to the QPC, the cantilever's tip and the QPC are capacitively coupled. The tip acts as a movable third gate above the device surface, able to affect the potential landscape of the QPC channel and thereby to alter its conductance G. A voltage V_{G} applied to the split gates patterned on the surface modifies G in the same manner.

Figure 3.6 shows the effect on the QPC conductance by the gate voltage V_{G} or by a potential V_{L} applied to the cantilever. In both cases, the cantilever is located in the same position above the QPC and a DC source-drain voltage $V_{\mathrm{sd}} = 5.0$ mV is applied to ohmic contacts on either side of the QPC gates. As either V_{G} or V_{L} are made more negative, both act to deplete the electron gas in the QPC, decreasing G in steps of $2e^2/h$, until the conduction channel
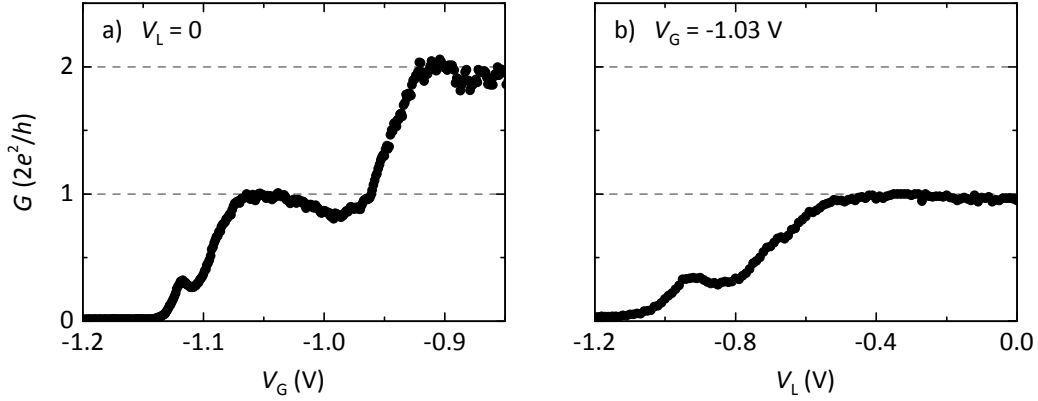
Figure 3.6 | **Conductance quantization as a function of gate and cantilever voltage.** At zero magnetic field, the cantilever is positioned above the QPC, while (a) V_G sweeps down until conduction pinch-off, at $V_L = 0$, and (b) V_L sweeps, while $V_G = -1.03$ V. The small conductance oscillation at $\approx 0.3\,G_0$ is probably due to a charged defect in proximity to the QPC, as shown also in Fig. 3.7.

pinches off. Comparing Figs. 3.6(a) and (b), we find that G is about 9 times more sensitive to the variation of V_G with respect to V_L. This factor corresponds to the ratio between the two capacitances to the QPC, which, due to the high dielectric constant of GaAs, strongly depends on the relative separation between the QPC and the cantilever tip.

The QPC sensitivity to cantilever motion also depends on the relative orientation between the direction along which the cantilever oscillates and the one followed by the current flow. For studying this behavior, different QPCs have been defined on the same chip (Fig. 3.1), with the split gates patterned such that a current flows either along the cantilever's oscillation direction (x axis in Fig. 3.5), or perpendicular to it. For geometrical reasons, G is most sensitive to cantilever motion when the cantilever is positioned just in front or just behind the QPC along x. Since the split gates partially shield the cantilever's effect on the QPC, the most favorable configuration is with these gates oriented such that the current flows along x. In order to map the effect on the conductance of the cantilever's position above the QPC device, G has been recorded while scanning the cantilever at fixed distance z, with a potential V_L applied. In such a conductance map, the position corresponding to the highest sensitivity is where the absolute value of the spatial derivative along the oscillation direction is maximum, as shown in Fig. 3.7.

With the tip of the cantilever so positioned, the QPC acts as a transducer of cantilever motion. Applying a gate voltage $V_G = -0.837$ V and a cantilever voltage $V_L = -1.280$ V, the QPC conductance is tuned to one half the value of the first conductance quantum. The QPC transduces the cantilever's ther-
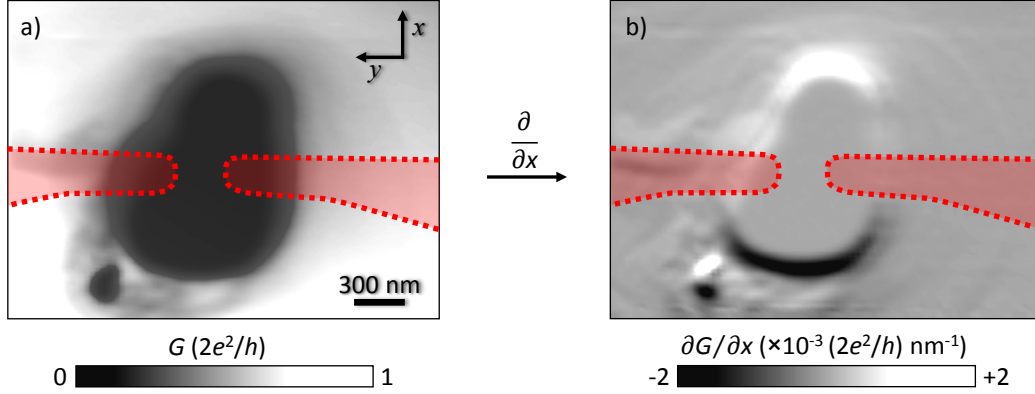
Figure 3.7 | **Conductance map.** (a) G and (b) its spatial derivative $\partial G/\partial x$ plotted as a function of the cantilever's position over the QPC, at a fixed distance $z = 80$ nm. The red shaded areas outline the position of the QPC gates. A 2-T magnetic field is applied perpendicular to the sample, $V_G = -0.837$ V, $V_L = -1.280$ V. The spot in the lower left corner of both figures might be due to a charged defect close to the QPC constriction. Data were processed with WSXM software [106].

mal motion into a current signal, as shown in Fig. 3.8(a). Under the same conditions, we also measure the cantilever displacement with the interferometer, which is used as an out-of-loop independent detector; the result is shown in Fig. 3.8(b). The resonances represent the cantilever's fundamental mode and match in both frequency and quality factor. In order to express the QPC current response (left axis in Fig. 3.8) in terms of cantilever motion (right axis), we normalize the peak QPC current spectral density to the peak of the displacement response measured by the interferometer, obtaining a conductance response up to $0.002 \, (2e^2/h) \, \mathrm{nm}^{-1}$ of cantilever motion. Note that, since the interferometer laser cannot be focused directly onto the cantilever tip, the displacement amplitude has to be retrieved from the relation (1.36), knowing the distance of the focus point from the tip ($\approx 90 \, \mu\mathrm{m}$) and the cantilever's mode shape function (see Section 1.5.1).

We verify that the QPC response at the cantilever resonance frequency is not an effect of electrical feedthrough, due, for example, to stray capacitive coupling between measurement lines. To do so, we drive the QPC with an AC source-drain voltage $V_{sd} = 2.0 \, \mathrm{mV_{rms}}$ at 113 Hz. In this situation, the QPC current spectrum, shown in Fig. 3.9, reveals a response centered on the cantilever's fundamental resonance and split between two peaks spaced by twice the source-drain drive frequency. The QPC is therefore mixing the cantilever thermal noise with its electrical AC excitation, confirming the mechanical origin of its response [54]. Further evidence comes from exciting cantilever oscillations using the mechanically coupled piezoelectric element: the height of the two side peaks increases with excitation amplitude.
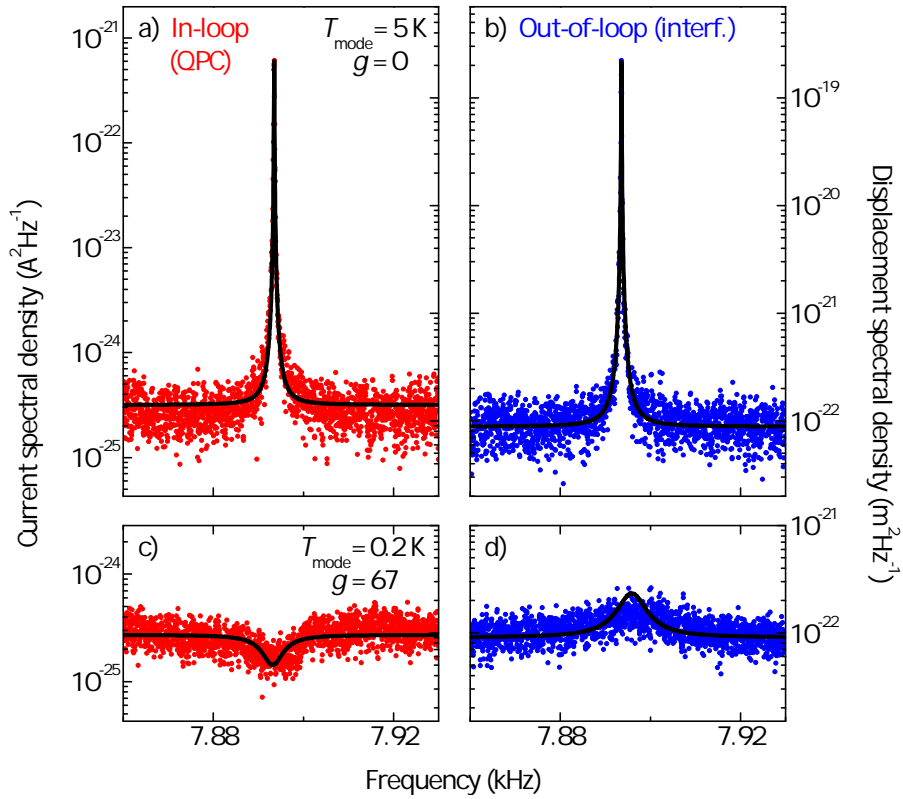
Figure 3.8 │ **Cantilever's fundamental mode spectrum.** The spectrum is detected at a base temperature $T = 4.2$ K by (a, c) a QPC transducer, (b, d) a fiber-optic interferometer. The QPC response is expressed in terms of both A^2 Hz^{-1} (left axis) and m^2 Hz^{-1} (right axis). (a) and (b) represent the cantilever thermal noise, (c) and (d) are the results of feedback damping. In the measurements shown here, the QPC gives a conductance response of $2 \times 10^{-4} \, (2e^2/h) \, nm^{-1}$ of cantilever motion.

3.4.2 Cantilever Feedback Cooling

Chapter 1 is devoted to describing the mechanics of a micro- or nano-sized resonator. It explains that, for frequencies in the vicinity of the fundamental mode, and for high quality factor, the motion of a cantilever is well approximated by the equation of a damped harmonic oscillator, driven by thermal force. Here we are studying the case of a closed-loop system, aimed at reducing the cantilever's fundamental mode temperature. Therefore also a driving feedback force has to be considered in the equation of motion. We approximate the optimal control operated in the feedback loop as a force proportional to the cantilever displacement with a $\pi/2$ phase lag. In the experiment, the phase of the feedback signal is affected by the delay introduced by stray capacitances in the loop and it has been tuned in order to achieve
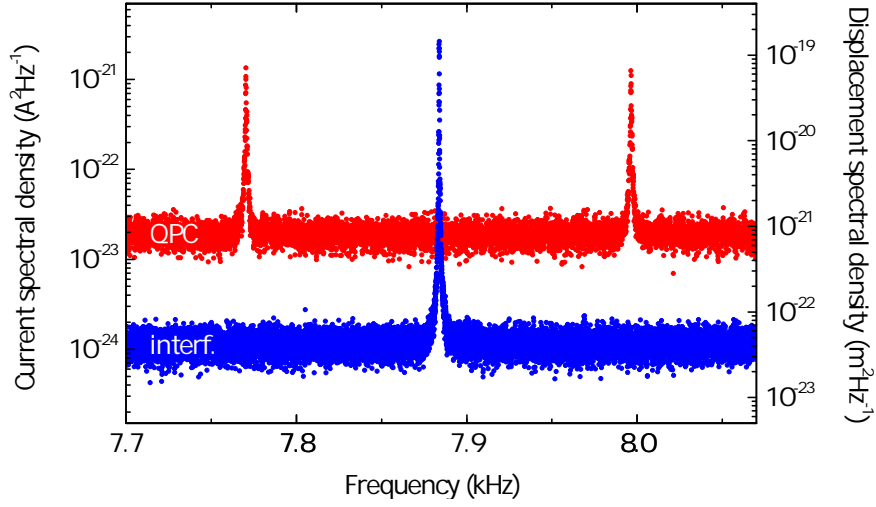
Figure 3.9 | **Cantilever thermal noise mixed with AC QPC excitation.** The fundamental mode spectrum is detected at a base temperature $T = 4.2$ K by a QPC transducer (red plot) and a fiber-optic interferometer (blue plot). The QPC response is expressed in terms of both A^2 Hz^{-1} (left axis) and m^2 Hz^{-1} (right axis). The QPC is driven by a 2.0 mV$_{rms}$ sinusoidal signal at 113 Hz.

the desired value $\pi/2$ for optimal damping [18]. The equation of motion of the cantilever can thus be written as:

$$m\ddot{x} + \Gamma_0\dot{x} + k_0 x = F_{th} - g\Gamma_0\omega_0\,\delta(t - \pi/(2\omega_0)) \otimes (x + x_n), \qquad (3.1)$$

where g is the feedback gain coefficient, $x_n(t)$ is the measurement noise on the displacement signal, δ is the Dirac distribution, and the symbol $\otimes$ denotes convolution.

Considering in (3.1) frequency components of the form $\hat{F}_{th}(\omega)\,e^{i\omega t}$ and $\hat{x}_n(\omega)\,e^{i\omega t}$, it is possible to determine the resonator's displacement spectral density as measured in-loop (S_x^{il}) and out-of-loop (S_x^{ol}). To do so, we follow the procedure described in Refs. [18,32] and detailed in Section 1.6.1. Applying the fluctuation-dissipation theorem (1.50), we express the white spectral density of the thermal force F_{th} in terms of the cantilever's mechanical parameters ω_0, k, and Q_0, and of the bath temperature T. The out-of-loop response is simply the sum of the cantilever's actual displacement $S_x(\omega)$ and the white spectral density of the interferometer's measurement noise S_{ξ_n}. On the other hand, in the case of the in-loop response, feedback produces anti-correlations between the transduction noise and the mechanical motion of

the cantilever. The resulting equations are the following:

$$S_x^{\text{il}}(\omega) = \frac{\frac{4\omega_0^3 k_B T}{Q_0 k_0} + \left[(\omega_0^2 - \omega^2)^2 + \left(\frac{\omega_0 \omega}{Q_0}\right)^2\right] S_{x_n}}{(\omega_0^2 - \omega^2)^2 + \left[\frac{\omega_0}{Q_0}(\omega + g\omega_0)\right]^2}, \tag{3.2}$$

$$S_x^{\text{ol}}(\omega) = S_x(\omega) + S_{\xi_n} = \frac{\frac{4\omega_0^3 k_B T}{Q_0 k_0} + \left(\frac{g\omega_0^2}{Q_0}\right)^2 S_{x_n}}{(\omega_0^2 - \omega^2)^2 + \left[\frac{\omega_0}{Q_0}(\omega + g\omega_0)\right]^2} + S_{\xi_n}. \tag{3.3}$$

We fit the undamped out-of-loop and in-loop spectra in Figs. 3.8(a), (b) with feedback gain $g = 0$. We first fit the out-of-loop spectrum through the Eq. (3.3) with three free parameters: ω_0, Q_0 and S_{ξ_n}. Setting these parameters as constants, we then fit the in-loop spectrum with S_{x_n} as the only free parameter. Both spectra are well described by the fit functions. The value of Q_0 extracted from this procedure is equal to 8.0×10^4 and is lower than that measured with the cantilever far from the QPC surface, due to unavoidable non-contact friction. S_{x_n} and S_{ξ_n} express the level of the noise floors for the in-loop and the out-of-loop measurements, respectively. They set the sensitivity of the QPC and the interferometer as displacement transducers, which is roughly the same for both: below 10^{-11} m Hz$^{-1/2}$.

The effective temperature of the fundamental mode T_{mode} does not depend on the measurement imprecision. It is proportional to the area under the curve $S_x(\omega)$, as defined in Eq. 1.54, considering only frequencies close to ω_0. For the data in Figs. 3.8(a) and (b), using the expression of $S_x(\omega)$ obtained from the fit, it results $T_{\text{mode}} = 5$ K, which is close to the bath temperature T of liquid helium.

We now describe the feedback cooling of the cantilever's fundamental mode using the QPC transducer. Optimal control of the resonator motion in the feedback loop allows the damping of its fundamental mode oscillations and therefore the reduction of T_{mode}. Such an effect can be described with the application of a non-zero gain g to the equation of motion (3.1). Increasing the value of g has the effect of lowering the displacement spectrum, as shown in Fig. 3.10. For high g, the feedback loop produces anticorrelations between the in-loop transduction noise and the oscillator's motion [32, 103, 104]. As a consequence, the displacement spectral density detected inside the feedback loop can even exhibit a dip below the noise floor near the oscillator's resonant frequency, as shown by the green plots in Fig. 3.10 and by Fig. 3.8(c). This spectrum represents the first evidence of noise *squashing* for a transduction scheme limited by electron, rather than photon, shot-noise. The solid line plotted along with this in-loop spectrum in Fig. 3.8(c) is a fit computed using Eq. (3.2), with the value of Q_0 extracted previously and with g as the free parameter.
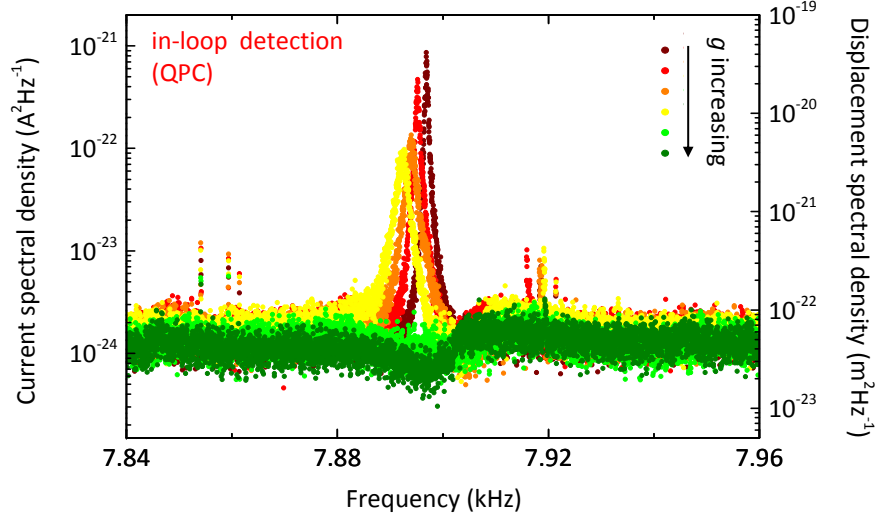
Figure 3.10 | **Feedback cooling of cantilever thermal noise.** The motion of the fundamental mode at a base temperature $T = 4.2$ K is damped by the application of a feedback force. Increasing the feedback gain g, the displacement spectrum detected in-loop is pushed down to the measurement noise level (red to yellow plots) and even below (green plots). The latter is the manifestation of noise *squashing*.

In order to provide a validation of the observed phenomenon and an independent measurement of T_{mode}, the cantilever motion is also detected through the out-of-loop interferometer. This spectrum, shown in Fig. 3.8(d), exhibits a peak above the uncorrelated measurement noise $S_{\xi_{\mathrm{n}}}$. In order to compare our model with the measured data, we plot the curve defined by Eq. (3.3) as a solid line in Fig. 3.8(d), using Q_0, $S_{x_{\mathrm{n}}}$, and $S_{\xi_{\mathrm{n}}}$ extracted from the previous fits and g extracted from the fit to the damped in-loop QPC spectrum of Fig. 3.8(c). The plot of the out-of-loop spectrum highlights the agreement between our theoretical model and the experimental data.

To calculate the mode temperature, a general relation can be derived from Eq. (1.54), using the expression of $S_x(\omega)$ given in Eq. (3.3). We find for T_{mode} the same result obtained in Ref. [32], valid for high quality factor:

$$T_{\mathrm{mode}} = \frac{T}{1+g} + \frac{k_0 \omega_0}{4 k_{\mathrm{B}} Q_0} \left(\frac{g^2}{1+g} \right) S_{x_{\mathrm{n}}}. \tag{3.4}$$

The values of T_{mode} resulting either from direct integration of the spectrum as in Eq. (1.54), or by extracting the parameters from the fit and then substituting them into Eg. (3.4), are equal within our precision: 0.2 K, twenty times less than the bath temperature. While such a cooling factor is smaller than what is obtained in other experiments (see Ref. [18], Table 6), this result represents an initial demonstration of feedback cooling employing a mesoscopic electronic transducer.

Equation (3.4) implies that, in the limit $g \gg 1$, the minimum achievable temperature is:

$$T_{\text{mode}}^{\min} = \sqrt{\frac{m\omega_0^3 T}{k_{\text{B}} Q_0} S_{x_{\text{n}}}}. \tag{3.5}$$

In our case, the minimum temperature results 0.21 ± 0.05 K, which is equal within the error to the observed value of T_{mode} in the noise squashing regime.

3.5 Conclusion and Outlook

The minimum achievable temperature in Eq. (3.5) expresses the efficiency of a cooling scheme based on active feedback. In fact, minimizing T_{mode} implies approaching a state with low phonon occupation number

$$N_{\text{mode}}^{\min} = \frac{k_{\text{B}} T_{\text{mode}}^{\min}}{\hbar\omega_0} = \frac{1}{2\hbar}\sqrt{S_{F_{\text{th}}} S_{x_{\text{n}}}}. \tag{3.6}$$

In order to access this regime, future experiments should minimize both the force noise and the measurement imprecision. The former involves employing cantilevers with low mass, low resonance frequency, and high quality factor. The base temperature should also be lowered, by means of a ^{3}He or a dilution refrigerator. In this case, care should be taken to isolate the cantilever from external vibrations, coming particularly from the cooling system, which could hinder the achievement of the lowest T_{mode}. Furthermore, T_{mode} can be influenced by measurement back-action effects, emerging on the resonator by accessing a regime of strong coupling with the transducer. As described in Section 1.6.2, back-action force has a rising contribution on S_x when approaching the quantum ground state of motion. In particular, when the force noise $S_{F_{\text{th}}}$ is dominated by the detector back-action and the detector itself is quantum limited, it results $\sqrt{S_{F_{\text{th}}} S_{x_{\text{n}}}} \approx \hbar$ and the lowest phonon occupancy is reached [7, 82].

A crucial improvement towards reaching the lowest T_{mode} is represented by a reduction of $S_{x_{\text{n}}}$, which involves both a decrease in the QPC current noise and an increase in the sensitivity of the QPC to the cantilever's displacement. In the experiment presented here, the QPC current noise floor is within a factor 10 above its shot-noise limit; an improvement of the measurement setup should allow us approaching this limit. On the other hand, a better sensitivity could be achieved in two ways:

1. improving the performance of the QPC as a one-dimensional conductor;

2. increasing the cantilever-QPC capacitive coupling.

The former implies optimizing the geometry of the split gates and reducing the bath temperature so as to have sharper QPC conductance quantization. As a result, the device should be more sensitive to local electrostatic fields. The latter requires us to optimize the shape of the cantilever tip for a higher influence on the QPC potential landscape and to bring the conductance channel closer to the tip. This task could be accomplished by using a QPC defined on a shallower 2DEG, as investigated in Chapter 4, and, more importantly – due to the high dielectric constant of GaAs – by reducing the gap between the cantilever tip and the QPC sample surface. Both solutions come at a cost: shallower 2DEGs are closer to the fluctuating charged defects on the wafer surface, raising the measurement imprecision; bringing the cantilever closer to the surface and to the split gates increases the non-contact friction. Reducing the density of charged defects on the surface remains a crucial challenge for future devices.

4 | Transduction of Nanomechanical Motion using Mesoscopic Transport

The previous chapter shows the performance of a split-gate QPC as a displacement transducer and as a means for feedback cooling the fundamental mode temperature of a nearby micro-sized cantilever. The minimum effective temperature and the sensitivity achieved by the QPC detector depend on its performance as a one-dimensional conductor and on the cantilever-QPC capacitive coupling.

In this chapter we report on some ongoing experiments, started within the work of this thesis, aimed at obtaining a stronger coupling between mechanical modes and quantized electronic states. The first section deals with the coupling of an ultra-soft cantilever to a QPC defined on a shallow 2DEG by local oxidation lithography. The close proximity of the 2DEG to the sample surface (only 35 nm) and the ability to tune the QPC width avoiding charged surface gates should in principle improve the cantilever-QPC capacitive coupling, by reducing their relative separation.

In the second section, we present an innovative electromechanical system made of a suspended-nanowire single-electron transistor (SET). Similar devices have been demonstrated to couple NW motion in a doubly-clamped geometry to single-electron tunneling events through the device [107]. The contribution of this thesis consists in the design and development of a fabrication protocol for defining a single or multiple quantum dots within a suspended NW via local electrostatic gates. This approach should allow a better control of the tunneling through the dots in the few-electron regime, through the application of relatively low electrostatic potentials. Besides studying the electromechanical interaction in the NW, such a device can be also coupled to the motion of an off-board cantilever, reasonably offering a better transduction efficiency with respect to a QPC.
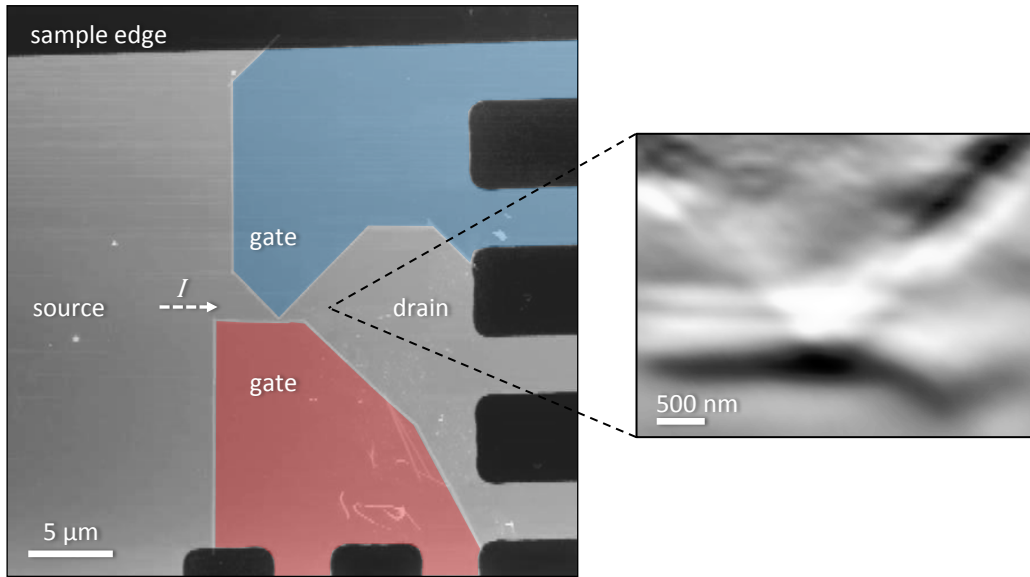
4.1 QPC Sensor Defined by Local Oxidation

Local oxidation of semiconductor heterostructures has revealed a powerful patterning technique, able to define several high-quality mesoscopic devices, such as QPCs, QDs, and antidot superlattices [108]. The general procedure consists in using an atomic force microscope (AFM) to locally oxidize the heterostructure surface, through the application of an electrostatic potential between the conductive AFM tip and the substrate. The AFM and the sample reside in a sealed chamber with nitrogen atmosphere of controlled humidity (typically $40 - 50\%$) and the tip is negatively biased (between -15 and -20 V) while scanning across the sample in tapping mode. As a result, the sample surface oxidizes in correspondence to the AFM tip, yielding oxide lines typically 100 nm wide and 8-20 nm high, depending on the applied voltage and the damping set-point of the AFM during the process [108]. For high-quality 2DEGs located close enough to the sample surface, the electrons get depleted below the oxidized regions. This way the plane of a 2DEG can be separated into various conductive areas which are laterally insulated from each other.

Developing this technique, our collaborators S. Hellmüller and K. Ensslin from ETH Zurich have designed and fabricated a QPC on a GaAs/AlGaAs heterostructure forming a 2DEG at only 35 nm from the surface. After pre-patterning the sample with a *mesa* and *ohmic contacts* via optical lithography (see Section 3.2.1), they have defined via local oxidation a narrow constriction in the 2DEG, about 100 nm wide. The oxide lines cut the 2DEG into four regions, out of which two are used as source and drain contacts and the other two as lateral in-plane gates for controlling the width of the QPC channel. The QPC is defined at less than $20 \, \mu\text{m}$ from the sample edge for the subsequent alignment to the fiber-optic interferometer part of the displacement measurement setup (see Sections 2.1 and 3.3.3). After the lithography, the same AFM setup is used to verify the process by scanning the sample at zero bias, obtaining a micrograph like the one shown in Fig. 4.1.

After mounting the sample on a custom chip carrier (CMR-Direct) and Au-bonding its contacts, we proceed to the QPC electrical characterization at $T = 4.2$ K. An AC voltage $V_{\text{sd}} = 100 \, \mu\text{V}_{\text{rms}}$ at 177 Hz is drawn across the source and drain contacts and the conductance G is measured while sweeping symmetrically a voltage V_{G} applied to the side gates. In case of a split-gate QPC, as the one described in Chapter 3, a negative potential has to be applied to the top gates for depleting the electron gas beneath. In a QPC defined via local oxidation, instead, at zero bias the conduction channel results pinched off, because of the intrinsic potential of the surface states in the oxide lines. Therefore a positive gate voltage is required to allow electron transport,

Figure 4.1 │ **Atomic force micrograph of a QPC defined by local oxidation.** The structure's active area is patterned within 20 µm of the sample edge. The blue and red shaded areas in the figure outline the two portions of the 2DEG used as side gates for controlling the QPC. The inset is a zoom-in of the QPC constriction, obtained using the cantilever of the measurement setup as a non-contact AFM probe. Data were processed with WSXM software [106].

as shown in Fig. 4.2. The graph visualizes the first conductance plateau, after subtraction from the raw data of a contact resistance $R_b = 8$ kΩ. We do not open the channel even further to avoid current leakage through the oxide barriers. The shoulder visible in the conductance graph at $0.7\,G_0$ likely corresponds to an effect known in the literature as *0.7 anomaly*, whose origin is still subject to debate [109]. This assumption is confirmed by measuring G in the presence of a strong magnetic field, since it has been observed that the 0.7 anomaly is sensitive to magnetism. In fact, increasing the field from 0 to 6 T (blue to red curves in Fig. 4.2), the 0.7 shoulder transforms into the first half-integer plateau, which is due to the removal of spin degeneracy in the QPC one-dimensional sub-bands (see Section 2.2.1).

4.1.1 Operation

The QPC is used to measure the low-temperature thermal motion of an off-board single-crystal silicon cantilever, of the kind described in Section 1.5.2, which provides a finite element model of its mode shape functions. The cantilever tip has been metallized with Ti/Au (10/30 nm), in order to reduce the non-contact friction due to the interaction with the QPC sample surface [105].
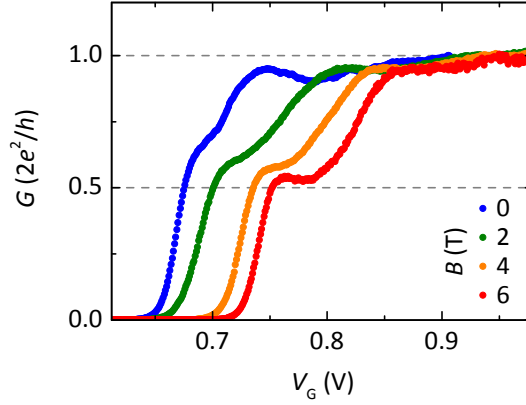
Figure 4.2 | **Conductance quantization in a magnetic field.** At $T = 4.2$ K, an AC voltage $V_{sd} = 100\,\mu V_{rms}$ at 177 Hz is applied between source and drain. At zero magnetic field, the QPC conductance exhibits a shoulder at $0.7\,G_0$ (blue curve). This effect gradually vanishes with the application of a strong magnetic field B, transforming into the first half-integer conductance plateau. The field is applied perpendicular to the sample.

The cantilever material is highly doped to make it conductive, therefore a voltage V_L can be applied by contacting the base of the chip. At $T = 4.2$ K, the cantilever has a fundamental resonance frequency $\omega_0/(2\pi) = 1.9$ kHz. The corresponding quality factor, measured in vacuum ($p < 10^{-6}$ mbar) through a *ring-down* technique (see Section 3.3.1), is $Q_0 = 10^4$. By measuring the cantilever thermal noise spectrum at several different bath temperatures, we find an ultra-low spring constant $k_0 = 100\,\mu N/m$, which makes such a resonator ideal for force sensing applications.

The experimental setup is the same described in Chapter 3. It ensures cryogenic operation at $T = 4.2$ K, good vibration isolation, and measurement with a low-power laser interferometer. The latter is used to independently calibrate the QPC displacement measurements in terms of cantilever motion.

After positioning the cantilever above the QPC, we optimize the alignment by imaging the sample using the cantilever as a non-contact AFM probe. In doing this, we follow the procedure described in Section 3.4, obtaining a micrograph of the QPC's active area shown in the inset of Fig. 4.1. Thereafter, we open the conduction channel by applying a voltage $V_G = 0.63$ V to the side gates. We negatively polarize the cantilever with $V_L = -1$ V and use it as a scanning gate, mapping its effect on the QPC conductance as a function of the scanning position, at fixed height $z \approx 150$ nm. The resulting image is reported in Fig. 4.3. It shows the depletion of the electron gas induced by the cantilever when it is positioned just above the QPC. The ring of higher conductance surrounding the depletion area is probably due to local defects which are charged up by the
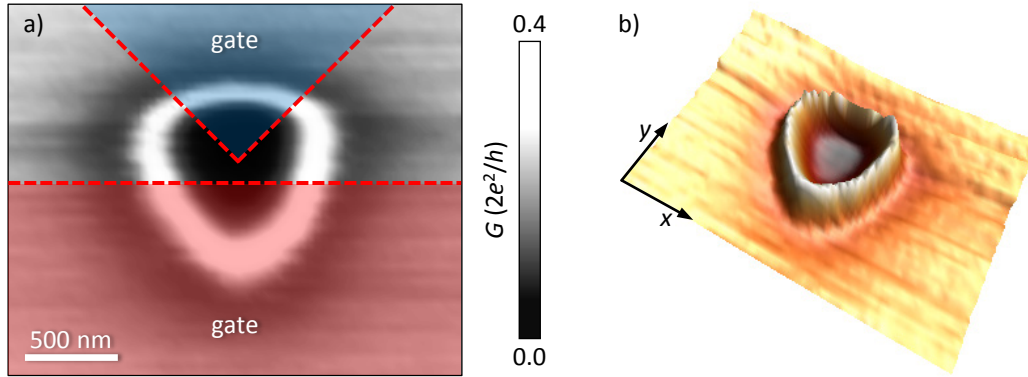
Figure 4.3 │ **Conductance map.** (a) G is plotted as a function of the cantilever's position over the QPC, at a fixed distance $z \approx 150$ nm. The blue and red shaded areas outline the portions of 2DEG used as lateral gates. $V_G = 0.63$ V, $V_L = -1$ V. (b) Three-dimensional plot of the same graph as in (a). Data were processed with WSXM software [106].

cantilever. Its shape resembles the geometry of the oxide lines defining the QPC, suggesting that the charged defects are likely due to the oxide itself. Because of the presence of this charge on the sample surface, the cantilever is subject to a high non-contact friction, which restrains the attempts to minimize the cantilever-QPC separation. This fact sets a strong limitation to the capacitive coupling that we are able to established between the two objects.

Positioning the cantilever tip just beyond the higher conductance ring in Fig. 4.3, we characterize the QPC as a transducer of the cantilever thermal motion. We apply a DC source-drain voltage $V_{sd} = 6$ mV and measure the spectral density of the QPC current. The result is plotted in Fig. 4.4, along with the displacement spectrum measured with the fiber-optic interferometer. The two spectra are a signature of the cantilever's fundamental mode and match in both frequency and quality factor. Since the interferometer laser cannot be focused directly onto the cantilever tip, we retrieve the displacement amplitude at the tip position by following the procedure described in Chapter 3, knowing the distance of the focus point from the tip (≈ 24 µm) and the cantilever's mode shape function (computed in Section 1.5.2).

The level of the noise floors for the QPC and interferometer measurements sets their sensitivity as displacement transducers. In case of the QPC, this is approximately 10^{-11} m Hz$^{-1/2}$, of the same order of the sensitivity reached by the split-gate QPC treated in Chapter 3.

4.1.2 Conclusion

We demonstrate that the performance of the QPC defined by local oxidation lithography as a sensor of cantilever motion is comparable to what we report
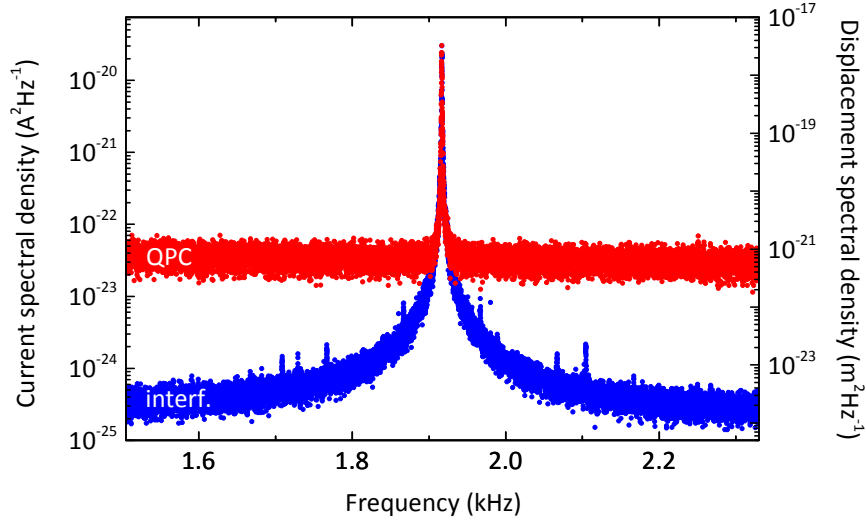
Figure 4.4 | **Cantilever's thermal noise spectrum.** The spectrum is detected at a base temperature $T = 4.2$ K by a QPC transducer (red dots) and by a fiber-optic interferometer (blue dots). The QPC response is expressed in terms of both A^2 Hz^{-1} (left axis) and m^2 Hz^{-1} (right axis).

for a QPC defined with top gates. Nevertheless, a strong limitation for the former device is the high non-contact friction between the cantilever and the sample surface. This unwanted electrostatic interaction arises from a high concentration of charged defects in correspondence to the QPC oxide lines. By limiting the minimum cantilever-QPC separation, this interaction restrains the capacitive coupling between the two objects.

Future experiments could attempt to reduce the friction by removing the semiconductor oxide via HCl or developer wet etching. In fact, it has been demonstrated that when the oxide is removed by dip etch, trenches remain in the locations previously occupied by the oxide, still preserving the structure's performance [108].

Following the same research direction, we have also studied a displacement detector made of a QPC defined via a shallow-etch technique [110,111]. Such a fabrication scheme consists in defining a one-dimensional conduction channel in a 2DEG by etching the heterostructure with large grooves deep enough to confine the electron gas in one dimension. Also in this experiment, we have experienced a high cantilever non-contact friction, due to the surface states enhanced by the etching process. Reducing the friction, perhaps by surface treatment of the QPC sample [105], still constitutes an interesting perspective for further experiments.
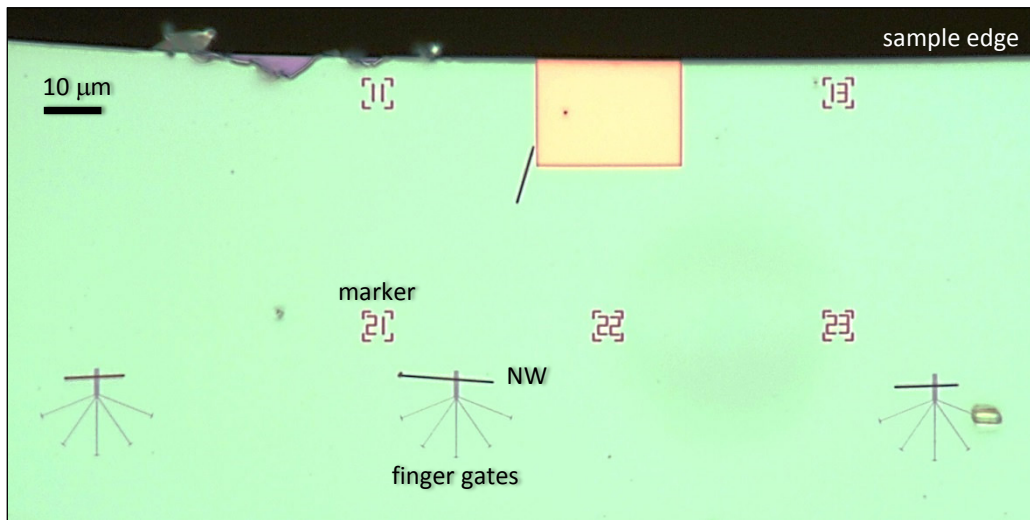
Figure 4.5 │ **NW positioned above finger gates.** Optical micrograph of a sample patterned with Ti/Au markers and narrow electrodes in the shape of fingers. After coating the sample with a first layer of electron-beam resist, InAs NWs are positioned individually above the finger contacts by means of a micro-manipulator. The NWs are then sandwiched in a second resist layer and the sample is cleaved for obtaining devices close to the sample edge, within $60\,\mu\mathrm{m}$ for the sample shown here.

4.2 Suspended-NW SET

We fabricate SETs made of single semiconducting NWs suspended above local electrostatic gates, in a doubly clamped geometry. The NWs are made of InAs and are grown via metal-organic vapor phase epitaxy. They are oriented in the $\langle 111 \rangle$ direction and are 100-150 nm in diameter with a typical length of several micrometers. The devices are realized on a degenerately doped Si substrate coated with a 300-nm layer of SiO_2. Such a conductive substrate can be used as a global back gate controlling the carrier density in the SET. The fabrication process is articulated in several stages summarized in the following. The detailed protocol is schematized in Appendix C.

Finger Gates and Markers. In a first stage, the substrate is patterned via electron-beam lithography with markers and narrow electrodes in the shape of fingers, as shown in Fig. 4.5. These finger leads are later used for locally gating the SET and eventually defining single or multiple QDs by tuning the carrier density in the NW and forming tunnel barriers. By e-beam evaporation and lift-off, finger gates and markers are metallized with Ti/Au, 5/15 nm thick.
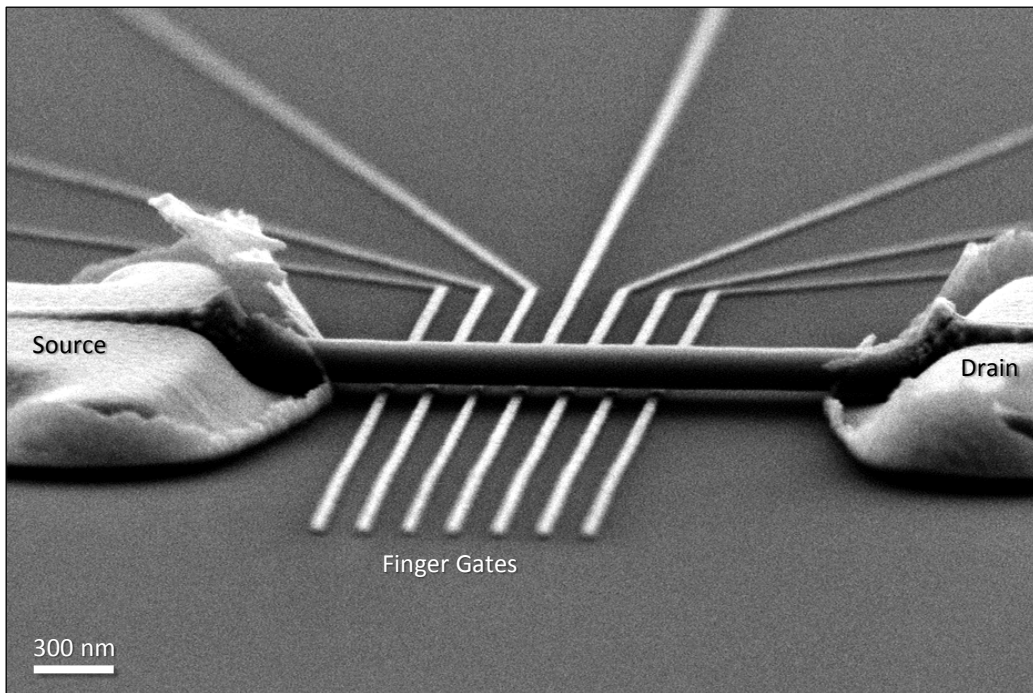
Figure 4.6 | **Suspended-NW SET.** Scanning electron micrograph of a device, with a NW suspended ≈ 80 nm above the finger gates. Source and drain contacts defined by sputtering deposition serve also as mechanical supports for the NW, in a doubly clamped geometry. The SEM stage has been tilted to highlight the narrow gap between the NW and the finger gates.

NW Transfer. Several NWs are transferred from their growth substrate and positioned one-by-one above the finger gates with a micro-manipulator, as in Fig. 4.5. In order to obtain suspended devices, the NWs are sandwiched between two layers of electron-beam resist. The first layer is spin-coated on the substrate prior to the NW transfer: its thickness determines the distance of the NWs from the substrate. The process has been optimized for obtaining $2\,\mu$m-long devices suspended without collapsing at 100 nm from the substrate. The tip of the micro-manipulator used for positioning the NWs is a custom tapered glass rod, whose high flexibility ensures careful alignment above the finger gates minimizing the risk of breaking the NWs.

Electrodes. The NWs are embedded into a second layer of resist, which serves for defining via EBL source and drain electrodes and contacts to the finger gates. After the resist deposition, the sample is carefully cleaved in order to obtain devices within $150\,\mu$m of the sample edge. Thereafter, we record the positions of the NWs with respect to the marker pattern and design a suitable EBL mask. Following resist exposure and development, the

sample undergoes a quick succession of etching and passivation stages aimed at improving the quality of the source and drain *ohmic contacts*. A first stage of oxygen-plasma etching removes the organic residuals from the contact areas. Then the NW surface within the contact areas is subject to sulfur passivation through a solution of ammonium polysulphide, $(NH_4)_2S_x$ [112]. Finally, the sample is loaded into a sputtering unit where it is subject to argon-plasma etching for removing the InAs native oxide. Without breaking the vacuum, we deposit Ti/Au contacts thick enough to fill the gap between the suspended NWs and the substrate and to completely cover the NW ends. While thermal deposition of metallic films in ultra-high vacuum is highly directional, sputtering deposition at higher pressure allows the contacts to wrap around the NW ends. Such metalizations serve therefore not only as source and drain ohmic contacts, but also as stiff mechanical supports for the NW. After lift-off, the process is completed by a phase of critical-point drying (CPD), which enables drying narrow-gap devices avoiding their collapse to the substrate because of surface tension. An SEM picture of a final device, with a NW suspended ≈ 80 nm above the finger gates, is shown in Fig. 4.6.

Bonding. The sample is glued to a customized chip-carrier (CMR-Direct) with silver paint, which enables electrical contact to the doped Si back gate. Au-bonding of the electrodes to the chip-carrier completes the fabrication.

4.2.1 Single-Electron Transport

At low temperature ($T = 4.2$ K), our NW transistor enters the Coulomb blockade regime. By depleting the charge carriers in the NW through the finger gates, we are able to confine quantized electron charge within the NW, thus forming a quantum dot. In such a regime, the quantum mechanical level spectrum of the QD can be studied by transport measurements. Charge confinement implies that the tunnel barriers isolating the QD are sufficiently high, or, in other words, that the tunnel resistance R_T is higher than the quantum of resistance: $R_T \gg h/e^2$ [113]. We can define a charging energy of the system, i.e. the energy required to add an electron to the QD, $E_C = e^2/C_\Sigma$, where C_Σ is the QD self-capacitance. When the charging energy is the dominant energy scale of the system, i.e. $k_B T \ll E_C$, single electron tunneling events through the dot can be observed [114].

We apply a small AC signal between source and drain, $V_{sd}^{AC} = 100\,\mu V_{rms}$ at 277 Hz, so that $V_{sd}^{AC} \ll E_C/e$. Then we record a so-called *charge stability diagram*, which is a plot of the conductance through the device as a function of both gate voltage and source-drain DC voltage. Sweeping the voltage on all the finger gates to negative values, the electrons in the NW are depleted. Approaching pinch-off, electrons enter the SET one at a time, and another
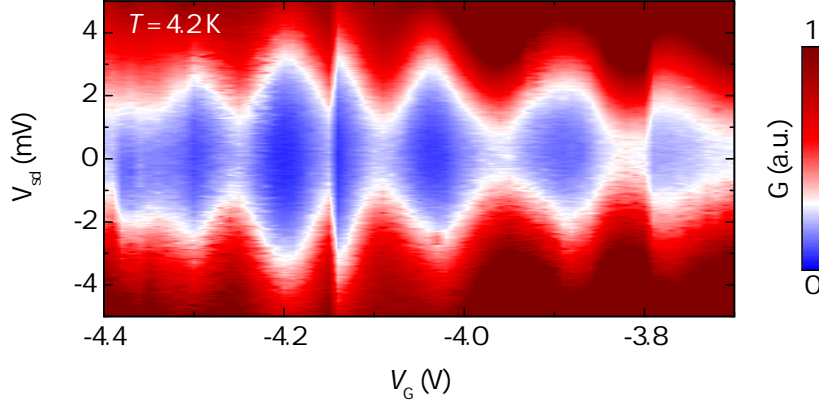
Figure 4.7 | **Charge stability diagram of the NW SET.** The conductance of the SET at $T = 4.2$ K is plotted as a function of the voltage V_G applied to all the finger gates and of the DC component of the voltage V_{sd} between source and drain. The device is fed with an AC source-drain signal $V_{sd}^{AC} = 100\,\mu V_{rms}$ at 277 Hz.

electron cannot tunnel into the device, until the first one tunnels out. In particular, electrons are able to tunnel if their energy contribution to the QD is higher than E_C. Either tuning the QD energy levels through the gates, or the electron injection energy through the source-drain potential, both are able to accomplish the condition for single electron tunneling. As a consequence, the conductance through the SET can be tuned by controlling either V_{sd} or V_G. The resulting stability diagram is shown in Fig. 4.7. The plot exhibits a diamond structure, clear signature of Coulomb blockade. Within each diamond, the current through the NW is inhibited due to the absence of available transport channels for that specific voltage range. Hopping from one diamond to the next consecutive one, the charge occupancy on the QD increases by one electron. These considerations allow us to estimate the self-capacitance of the QD and consequently its size. In fact, C_Σ is determined by the width of the Coulomb diamonds:

$$\Delta V_{sd} = \frac{E_C}{e} = \frac{e}{C_\Sigma}, \tag{4.1}$$

$$\Delta V_G = \frac{e}{C_G} = \frac{e}{\alpha_G C_\Sigma}, \tag{4.2}$$

where C_G is the capacitance between the finger gates and the QD and $\alpha_G \equiv C_G/C_\Sigma$ is the finger gates lever arm. From Eq. (4.1), we estimate the QD self-capacitance $C_\Sigma = 50$ aF, while from Eq. (4.2), we calculate the gate capacitance $C_G = 1.5$ aF and the corresponding lever arm $\alpha_G = 0.03$.

The QD likely corresponds to an impurity in the NW, which allows charge localization. Assuming the charge distribution to have a spherical symmetry,

we can write:

$$C_\Sigma = 2\pi\varepsilon_\mathrm{r}\varepsilon_0 D, \tag{4.3}$$

where ε_r and ε_0 are the dielectric constants of InAs and of vacuum, and D is the diameter of the charge distribution. Inverting this relation, we find $D = 60$ nm, compatible with a QD formed within the NW diameter.

4.2.2 Conclusion

The finger gates defined below the NW SET serve different functions. We have demonstrated their primary role in controlling the electron density in the NW, enabling to access the single-electron transport regime. In the prospect of electromechanical characterization of the device, they could also adjust the mechanical tension in the NW and actuate its motion [107]. Compared to a global back gate used for the same purposes, the finger gates present several advantages. By applying different voltages to each finger, they should allow defining a single or multiple QDs within the NW, opening up the possibility to have QDs in prefixed locations, with tunable barrier and energy levels, and not due to random impurities within the NW. Usually NW SETs with finger gates are made by depositing a thin insulating layer above the NW and then depositing the metallic gates on top. The insulator, usually HfO_2 [113], enhances the gate capacitance, due to its high permittivity, and inhibits current leaking. However, the direct contact of the NW with the insulating layer degrades the transport quality, due to the high concentration of charged defects at the interface. The suspended NW design, instead, should provide a solution to this issue, at the cost of a lower gate capacitance. Finally, attempting to couple a suspended-NW SET to the motion of an off-board cantilever could take advantage of the lower voltage required to pinch-off the NW with the finger gates, with respect to the back gate, which, due to a lower capacitance, typically needs several tens of volts. Lower voltage is directly related to lower non-contact friction, and then to the possibility to reduce the cantilever-SET separation for achieving a larger coupling strength. Such a system is promising compared to coupling to a QPC because the electron transport in the NW can be localized far closer to the cantilever motion than can the sub-surface transport through a QPC, reasonably resulting in a better transduction efficiency.

Further work is required for improving the control over the SET transport. The main current issue is the need for high voltage (below -20 V) for depleting the NW with a single finger gate. Using NWs with a more narrow diameter or of different material should reduce the carrier concentration and therefore allow a pinch-off at lower absolute voltage. On the other hand, the same goal can be accomplished by further reducing the NW separation

from the finger gates. Attempts in these directions are still ongoing in our laboratory.

5 | Quantum Dot Opto-Mechanics in a Fully Self-Assembled Nanowire

Coupling a nanomechanical resonator to a quantum limited displacement detector enables the readout of motion with ultra-high resolution. Besides applications to precise force and mass sensing, research in this field is now addressing what were once purely theoretical questions: the initialization and control of non-classical states of mechanical motion. In addition, a resonator can be coupled to another quantum system, providing a probe and readout device of its quantum state. Exploiting a mechanical resonator as a quantum probe opens interesting scenarios to quantum information processing and networking. For instance, the resonator could serve as a quantum transducer, mediating interactions between different quantum systems and therefore combining the advantages of distinct physical properties into one architecture.

In this chapter, we report on the coupling of a nanomechanical oscillator with controllable quantum states, in which both the coupling interaction and the quantum states themselves are intrinsic to the oscillator's structure. The quantum states are due to optically active quantum dots, embedded in MBE-grown GaAs/AlGaAs core-shell nanowires. Since a NW is also a nanomechanical resonator and the embedded QDs are naturally located close to its surface, the QDs are coupled to the NW motion. Oscillations of the NW produce a time-varying strain field, which modulates the QD emission energy in a broad range exceeding 14 meV. Furthermore, this opto-mechanical interaction enables the dynamical tuning of two neighboring QDs into resonance, possibly allowing for emitter-emitter coupling. Our approach opens up the prospect of using QDs to probe and control the mechanical state of a NW, or conversely of making a quantum non-demolition readout of a QD state through a position measurement. The results presented in this chapter have been published as:

[34] Montinaro, M., Wüst, G., Munsch, M., Fontana, Y., Russo-Averchi,

E., Heiss, M., Fontcuberta i Morral, A., Warburton, R. J., and Poggio, M. *Nano Letters* **14**, 4454 (2014).

5.1 Hybrid QD-in-NW System

Progress in nanotechnology allows the fabrication of a wide assortment of systems in which a mechanical resonator is coupled to a microscopic quantum system. These so called *hybrid systems* include optical [14] and microwave [23] cavities, superconducting devices [15,24], laser-cooled atoms [25], quantum dots [26,27], and nitrogen vacancy (NV) centers in diamond [20,28–30]. These coupling schemes usually rely on mechanical structures engineered by the application of electrodes, magnets, or mirrors, in order to translate motion into the modulation of electric, magnetic, or optical fields. In most cases, however, such a functionalization competes with the requirement of a small resonator mass, necessary to achieve a high coupling strength [37]. Moreover, the functionalization process often adds additional paths of dissipation and decoherence, reducing the lifetime of the coupled quantum system.

The coupling mechanism we present here is not only unusually strong, but its *built-in* nature produces a hybrid system whose inherent coherence is unspoiled by any functionalization or external field and whose fabrication is simpler than top-down techniques. The specific nano-resonator that we study is a bottom-up GaAs/AlGaAs core-shell NW containing optically-active QDs [36]. These QDs have been shown to emit narrow optical line-width (down to 29 μeV) single photons with high brightness (count rates in the MHz range) [36]. Here we show that their energy levels are coupled to the mechanical vibrations of the NW through intrinsic material strain. We demonstrate that mechanical motion allows a reversible tuning of the QD optical frequency with no measurable influence on its photoluminescence intensity.

5.2 Experimental Setup

In this section, we describe the growth details of the QD-in-NW system and its configuration in cantilever geometry. The experimental setup used for the mechanical and optical characterization of our hybrid system is also presented.

5.2.1 QD-in-NW Structure

Our QD-in-NW structures are fully self-assembled by molecular beam epitaxy. There is strong evidence that the QDs form at the apex of the GaAs/-
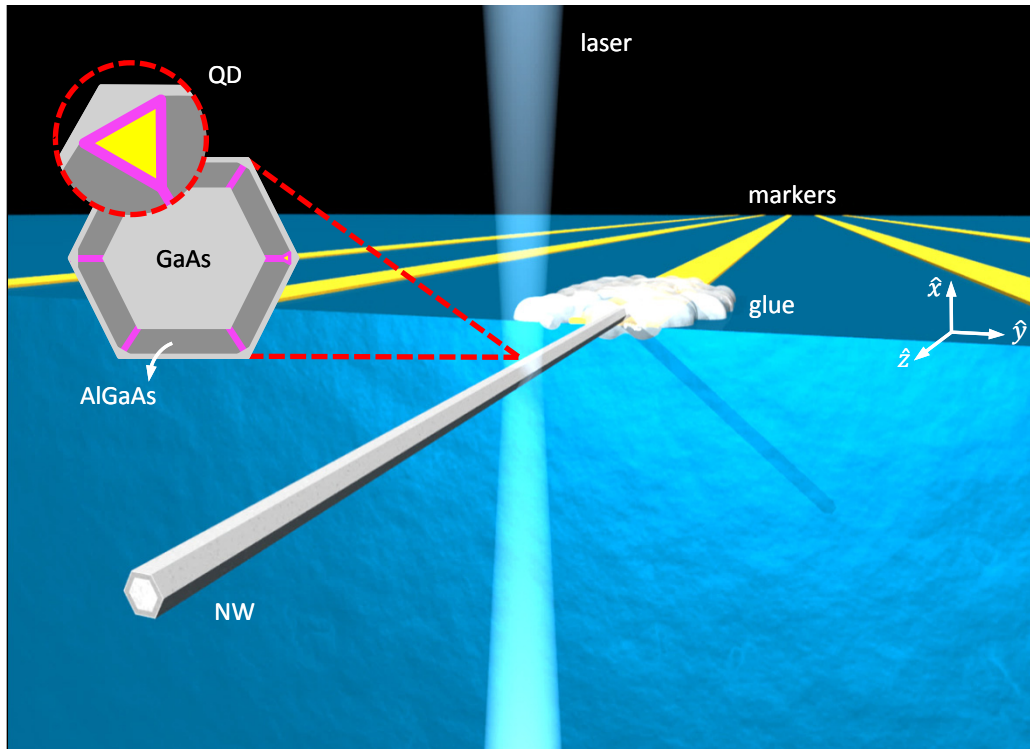
Figure 5.1 | **QD-in-NW structure.** The schematic picture shows a NW glued to the edge of a Si chip, and the laser beam used for optical and mechanical readout. The inset is a sketch of the NW cross-section, showing the composition of the core-shell structure and the close proximity of the embedded QDs to the surface of the NW. The purple regions are rich in Al content and surround an Al-poor region (yellow), defining a QD [36, 115].

AlGaAs interface, in Al-poor regions embedded in the Al-rich corners of the NW hexagonal cross-section [36, 115], as shown schematically in Fig. 5.1. Additional analysis supporting this explanation is reported in Appendix D. Note, however, that Weiß *et al.* offer an alternative interpretation, arguing that QD-like emission centers observed in similar core-shell NWs arise from randomly distributed alloy fluctuations or defects within the AlGaAs shell [116]. In either case, by controlling the overall diameter of core and shell during growth, it is possible to position the QDs within a few nanometers of the NW surface. This proximity to the surface allows for the optimal coupling of the QDs to the strain field in the NW, as shown in the finite element model in Section 1.5.3. Despite their position near the surface, these QDs retain their high optical quality, making them ideal for sensing applications. The NWs studied here have a predominantly Zinc-Blende crystalline structure and display a regular hexagonal cross-section. The synthesis starts with a 290-nm thick NW core, grown along $[1\,\bar{1}\,1]$ on a Si substrate by the Ga-

assisted method detailed in Refs. 117, 118. Once the NWs are about 25 μm long, the axial growth is stopped by temporarily blocking the Ga flux and reducing the substrate temperature from 630 down to 465 °C. Then a 50-nm thick $Al_{0.51}Ga_{0.49}As$ shell capped by a 5-nm GaAs layer is grown, as detailed in Ref. 119.

5.2.2 NW Cantilever

In order to study the opto-mechanical coupling, individual NWs are detached from their growth substrate with micro-manipulators (Narishige) and glued in a cantilever configuration to the edge of a silicon chip. Silicon has been chosen because not emitting in the same spectral range of the QD fluorescence. In a previous step, the Si chip is patterned with lithographically defined markers (Ti/Au, 10/30 nm thick), used for the optical alignment of the measurement setup. Particular care is necessary while manipulating and aligning the NWs. During the work of this thesis, this process has been optimized for high yield. The precautions include the use of sharp tungsten micro-chisels (Eppendorf) for detaching single NWs and of a low viscosity glue (Norland) to ensure a slow drying. For final adhesion, the glue requires an ultra-violet curing stage, which enables long working time for sample preparation. While a glue with very high fluidity would also allow a long preparation process, its use is not recommended because it can soak the entire NW, making its positioning problematic. The NWs are positioned with one hexagonal facet in contact with the Si chip and so that the length of the suspended portion amounts to about 20 μm.

5.2.3 Piezoelectric Transducer and Sample Stage

The sample containing several NWs aligned on one edge is rigidly fixed to a commercial piezoelectric transducer (PZT) from PI GmbH. Having a mechanical cutoff frequency in the MHz range, this PZT enables to efficiently drive mechanical oscillations of the NW.

As shown in Fig. 5.2, the chip and PZT are mounted to a three-dimensional positioning stage which has nanometer precision and stability (Attocube), in a low-pressure ^{4}He chamber ($p = 0.35$ mbar) at the bottom of a ^{4}He cryostat ($T = 4.2$ K).

5.2.4 Scanning Confocal Microscope

By controlling the positioning stage, we align individual QDs within each NW with the 400-nm collection spot of a confocal optical microscope [120].
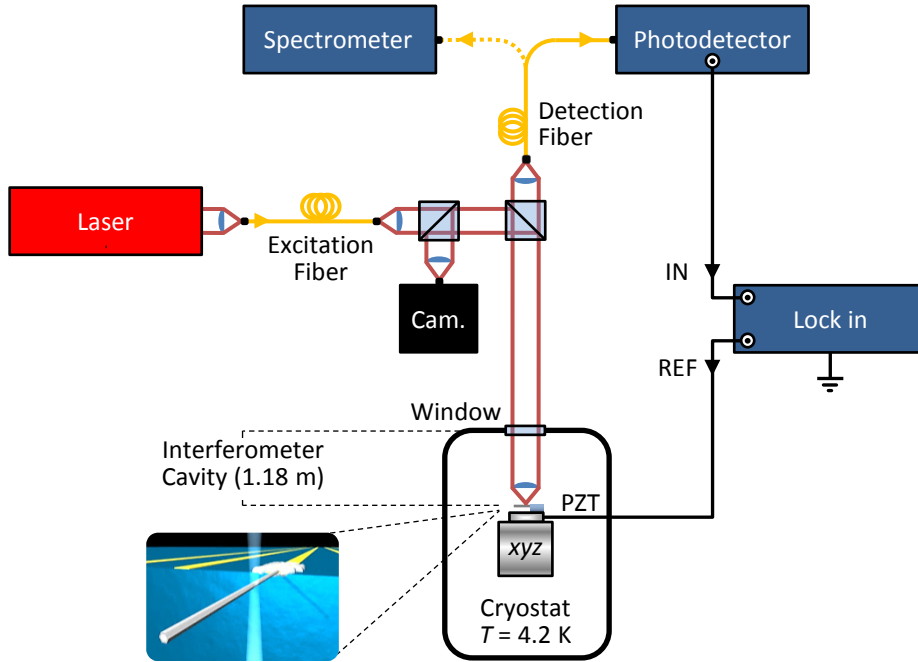
Figure 5.2 │ **Schematic diagram of the experimental setup.**

The microscope serves for non-resonant laser excitation of the QDs and efficient collection of their fluorescence. The confocal configuration is ensured by a single-mode optical fiber used for light collection, which serves as a pinhole [120]. Besides diffraction-limited optical performance, the microscope combines precise and reliable sample alignment, high mechanical stability with negligible drift over many days of operation, and elevated light collection efficiency, due to a high numerical aperture (NA = 0.82). As shown schematically in Fig. 5.2, the setup consists of a low-power HeNe excitation laser at 632.8 nm, a CCD camera for imaging the sample, and a high-resolution spectrometer for analyzing the emitted photoluminescence (PL). The spectrometer is essentially made of a monochromator and a nitrogen-cooled CCD, and provides a resolution of 60 μeV at the QD emission energy.

5.2.5   Laser Interferometer

We detect the mechanical oscillation of each NW via laser interferometry, through the technique described in Section 2.1. 80 μW of laser light from a wavelength-tunable, highly coherent 780-nm laser diode are focused onto the NW free end and the reflected light is collected by a fast photodetector. As shown in Fig. 5.2, the interferometer setup shares the optics of the confocal microscope. A low-finesse Fabry-Pérot cavity forms between the NW and
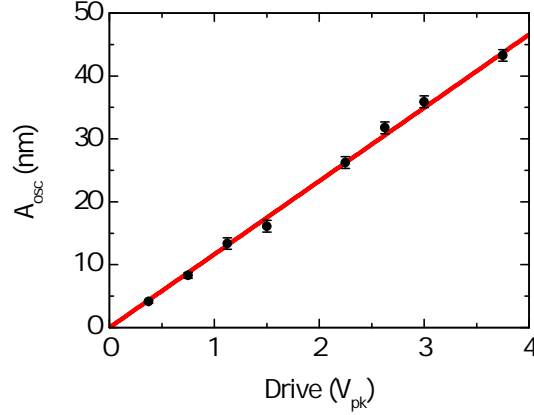
Figure 5.3 | **Interferometer test.** Amplitude of the positioning stage displacement oscillation at 117 Hz as a function of the amplitude of the drive voltage, measured at a temperature of 4.2 K. The error bars correspond to the peak-to-peak amplitude of the interferometric noise. The red line is a linear fit, from which we extract a conversion factor of 11.6 ± 0.1 nm/V.

a low-reflective window at the entrance of the ^{4}He chamber. This fact is confirmed by a measurement of the cavity free spectral range, $(2.6 \pm 0.1) \times 10^{-13}$ m, from which, by means of Eq. (2.9), we derive a cavity length of 118 ± 5 cm.

As discussed in Section 2.1, interferometer displacement measurements are calibrated by an accurate determination of the laser wavelength. In order to double-check this calibration, we measure the displacement amplitude A_osc of the positioning stage along the interferometer optical axis $\hat{x}$, while the stage is driven by a low-frequency oscillation (117 Hz). As shown in Fig. 5.3, the measurement is repeated for several drive voltages in order to extract, through a linear fit, a conversion factor for the piezoelectric positioning stage equal to 11.6 ± 0.1 nm/V. The entire procedure is repeated with the interferometer aligned to a variety of different positions on the yz plane, including the position of the NW free end. The values measured using our interferometer are close to the specifications of the positioning stage, which provide a rough conversion factor of 8 nm/V.

5.3 NW Displacement Detection

Using the PZT, we excite the fundamental mechanical mode of a NW and detect the resulting oscillations with the interferometer. The photodetector signal is filtered at the frequency and phase of the PZT excitation through a lock-in amplifier. Fig. 5.4(a) shows the spectral response of the free-end displacement x of the NW. A main resonance and a smaller peak at lower fre-
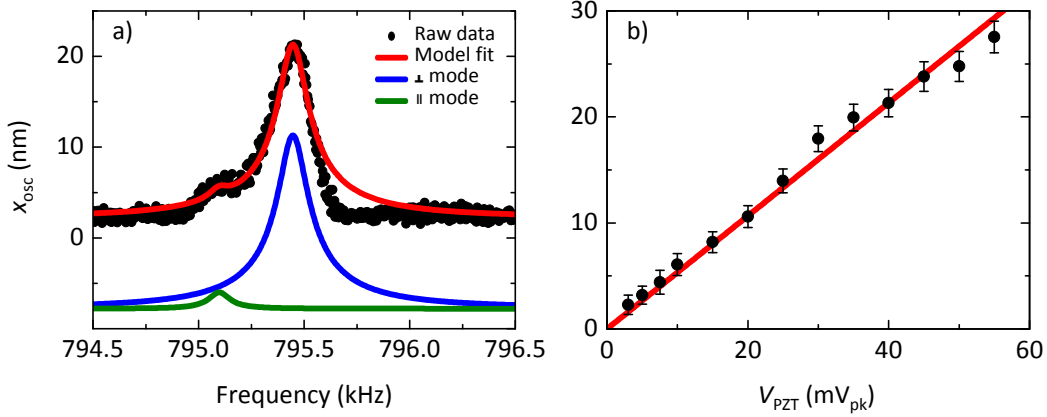
Figure 5.4 | NW mechanical characterization. (a) Spectrum of the NW free-end oscillation amplitude x_{osc} corresponding to its lowest order flexural vibrations at $T = 4.2$ K, driven by the PZT at $V_{PZT} = 40$ mV$_{pk}$. The red line is a model fit (see main text), highlighting two resonances split by 350 Hz, corresponding to polarized, non-degenerate vibrational modes. The green curve represents the vibration parallel to the NW substrate, while the blue curve represents the perpendicular one (both are shifted for clarity). The mechanical quality factors of the two modes, extracted from the fit, are $Q_{\parallel} = 7600$ and $Q_{\perp} = 5800$. (b) NW free-end oscillation amplitude x_{osc} as a function of the amplitude of the PZT excitation voltage V_{PZT}. The error bars correspond to the peak-to-peak amplitude of the interferometric noise. The red line is a linear fit, from which we extract the conversion factor $\partial x/\partial V_{PZT} = 0.53 \pm 0.01$ nm/mV.

quency are clearly observable, separated by 350 Hz. The asymmetric clamping of the NW to the Si chip, realized by gluing the NW with one hexagonal facet in contact with the Si surface (see Fig. 5.1), splits the fundamental mode into a doublet of flexural modes, oriented either perpendicular or parallel to the Si surface. This interpretation is confirmed by the finite element model of the system illustrated in Section 1.5.3. The mode oscillating perpendicular to the surface is preferentially driven by the PZT, because its oscillation direction $\hat{x}$ coincides with the axis along which the PZT moves. This mode is also more easily detected by the interferometer, since its direction of oscillation coincides with the interferometer optical axis. For these reasons, we interpret the main resonance in Fig. 5.4(a) as corresponding to the perpendicular mode. The asymmetry visible in this resonance is due to the onset of a weak mechanical non-linearity of the NW [56,95]. In the same way as described in Chapter 1, when excited in the linear regime, each of these mechanical resonances can be modeled as a damped harmonic oscillator with a resonant driving force. Following the procedure described in Section 1.6.1, we fit the NW response using this model, extracting for the perpendicular mode a resonant frequency $\omega_0/(2\pi) = 795.4$ kHz and a mechanical quality factor $Q_{\perp} = 5800$ and for the parallel mode $Q_{\parallel} = 7600$. Furthermore, by driving the main resonance as a function of the excitation
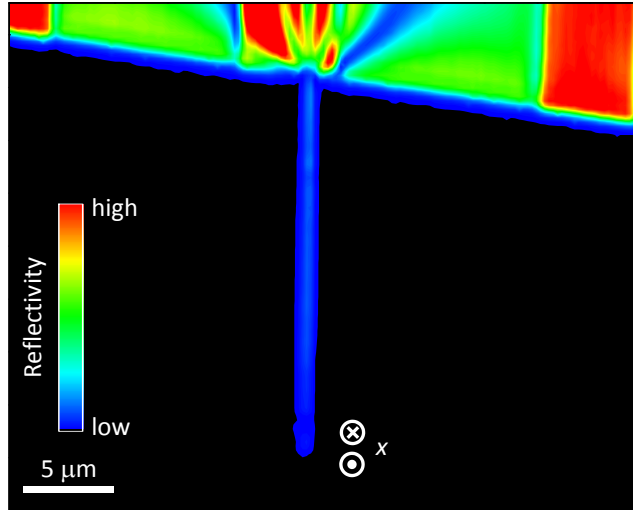
Figure 5.5 | **Scanning confocal micrograph.** The light reflected from the sample is plotted as a function of the laser beam position. The NW oscillation direction in the prominent mode is marked at its free end.

amplitude V_{PZT}, we explore the linear regime of the NW's free-end displacement, as shown in Fig. 5.4(b). With a linear fit, we extract a conversion factor, $\partial x/\partial V_{\mathrm{PZT}} = 0.53 \pm 0.01$ nm/mV, between the PZT drive amplitude and the amplitude of the free-end displacement.

5.4 Opto-Mechanics

We study the opto-mechanical coupling by collecting PL from individual QDs within a single NW. In a first step, we use the scanning confocal microscope for imaging the sample and finding a NW. The approximate position is found by using directly the CCD camera part of the setup. Afterward, for fine alignment, we collect the light reflected from the sample as a function of the scanning position. The resulting confocal micrograph for the NW under investigation is plotted in Fig. 5.5.

Sections 1.4.1 and 1.5.3 respectively report an analytical model and a FEM of the strain field in a long and thin cantilever with uniform cross-section throughout its length, like our NW structures. They show that the oscillation-induced material strain is highest at the clamped end of the NW. For this reason we search for QDs in proximity to this area, for obtaining the largest energy modulation. Using the scanning confocal microscope, a number of suitable QDs are identified near the clamped NW end, having bright, narrow, and spectrally isolated exciton emission lines. Figure 5.6
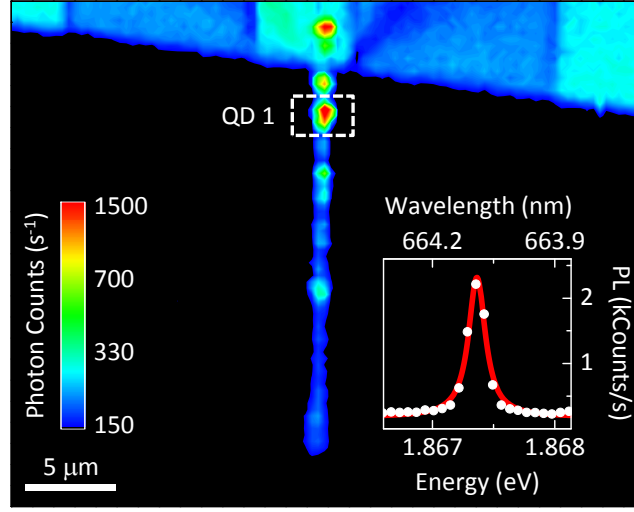
Figure 5.6 | **Spectrally filtered scanning confocal micrograph.** As a function of the excitation laser position, we plot the light intensity detected from the sample (logarithmic color scale), spectrally filtered at the peak PL energy $E_{\mathrm{ex}}^0 = 1.867$ eV, corresponding to exciton emission of QD 1. The inset shows the corresponding PL spectrum (white dots), together with a Lorentzian fit (red line). The linewidth (FWHM) is $\hbar\Gamma = 140\,\mu$eV.

shows a spatial map of the PL at 1.867 eV (664 nm) under non-resonant laser excitation of the sample. The plot also includes a weak component of reflected light at the filtered energy, which reveals the position of the NW and the Si substrate with its alignment markers, similarly to the confocal micrograph in Fig. 5.5. The map highlights a conveniently located QD, which we label QD 1, whose PL spectral signature includes an exciton emission peak shown in the inset.

In the next step, the laser beam is maintained in alignment with QD 1's position and its PL spectrum is recorded as a function of the PZT excitation frequency $\omega/(2\pi)$, while holding the amplitude V_{PZT} constant. As shown in Fig. 5.7(a), several emission peaks are detected within the same laser detection spot. As ω is swept through the NW resonance ω_0, the exciton emission peaks are broadened and deformed as a consequence of the time-integrated sinusoidal motion of the NW [27]. The envelope of the PL spectra as a function of ω resembles the NW displacement spectrum shown in Fig. 5.4(a). In particular, the low-frequency shoulder of the broadened envelope corresponds to the oscillation mode parallel to the substrate surface.

We explore the range of the exciton energy modulation by recording PL spectra as a function of the excitation amplitude V_{PZT}, while driving the NW on resonance with the dominant perpendicular mode ($\omega = \omega_0$). As shown in Fig. 5.7(b), each spectral line exhibits a different broadening, as a con-
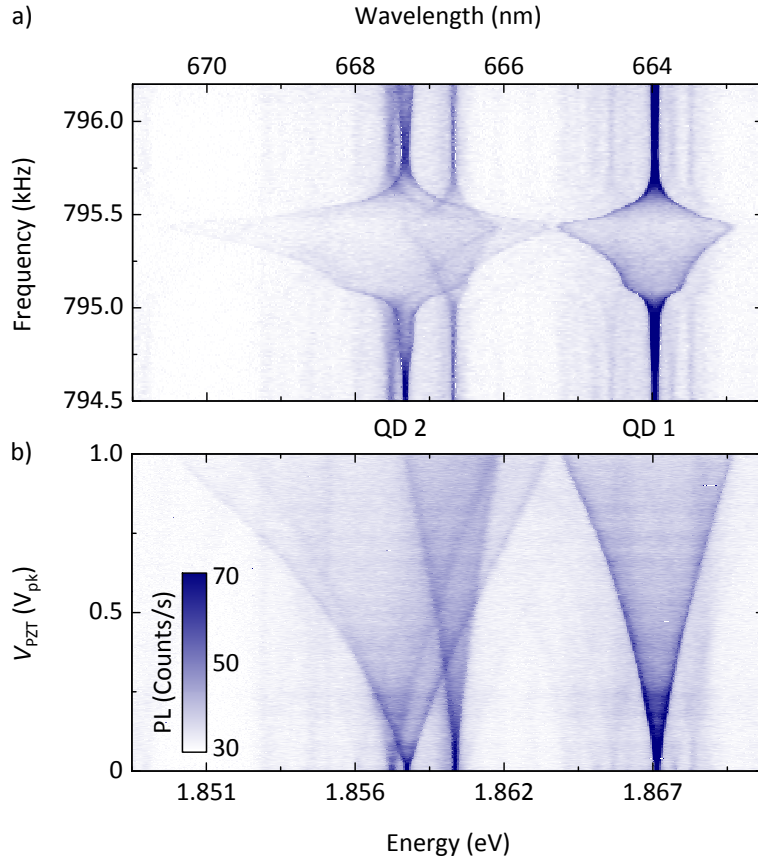
Figure 5.7 | **Effect of the NW excitation on the QD photoluminescence.** PL spectra of some neighboring QDs (labeled QD 1 and QD 2) acquired while sweeping (a) the frequency of the PZT excitation, with $V_{\mathsf{PZT}} = 1$ V_{pk}, and (b) the amplitude of the excitation, with the frequency set to the resonance of the NW's perpendicular flexural oscillation ($\omega = \omega_0 = 2\pi \times 795.4$ kHz).

sequence of its specific sensitivity to the local strain. For high excitation voltages, we observe an asymmetric energy broadening, due to the different response of the QD band structure under compressive or tensile stress in the NW [47, 121]. Note that a further increase of the excitation amplitude leads to a saturation of the peak-to-peak exciton modulation width just beyond 14 meV. It is currently not known whether this modulation is limited merely by how hard we are able to drive the NW motion, or whether a more fundamental saturation eventually limits the range.

5.4.1 Coupling Strength

While the mechanical motion of the NW in this experiment is best described in classical terms, individual PL peaks from an embedded QD can be approx-
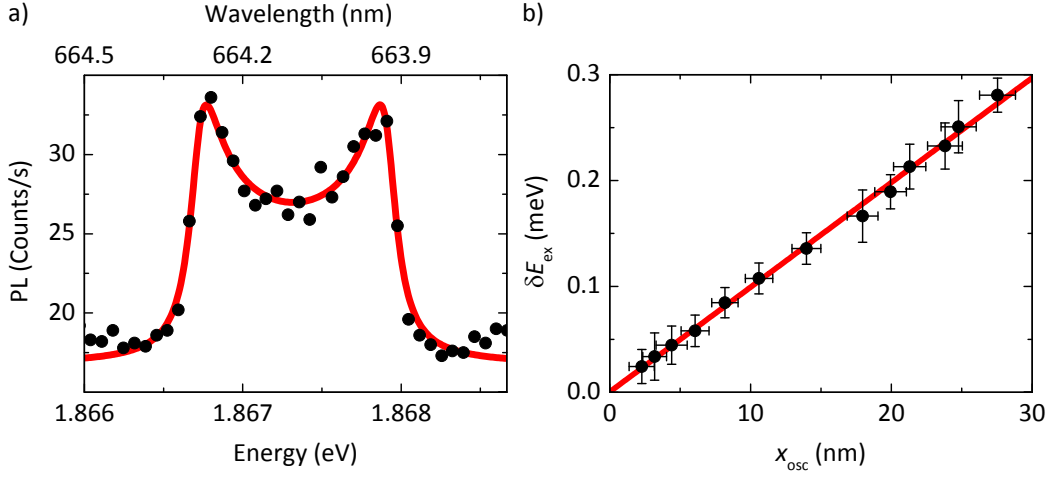
Figure 5.8 │ Strength of the opto-mechanical coupling. (a) PL spectrum of QD 1 (black dots) under NW excitation on resonance with the perpendicular flexural mode ($\omega = \omega_0$, $V_{\mathsf{PZT}} = 250$ mV$_{\mathsf{pk}}$). The red line is a fit according to the model equation (5.2), from which the exciton energy shift amplitude δE_{ex} is extracted. (b) δE_{ex} of QD 2 versus the NW free-end displacement amplitude x_{osc}. The red line is a linear fit, from which we extract the opto-mechanical coupling parameter $(\partial E_{\mathrm{ex}}/\partial x)|_{x=0} = 9.9 \pm 0.7\,\mu$eV/nm. The error bars on x_{osc} are the same as mentioned in Fig. 5.4(b); those on δE_{ex} are the standard deviations extracted from the fits of the mechanically excited PL spectra, as in (a).

imated as resulting from a quantum two-level system with an exciton transition energy $E_{\mathrm{ex}}(x)$ between ground and excited states $|g\rangle$ and $|e\rangle$ [36, 115]. The coupling between the NW motion and the QD can then be introduced as a shift in the exciton energy that depends on the displacement x of the NW's free end. Considering only the prominent perpendicular flexural vibration and neglecting non-linear terms in x [37], the time-dependent Hamiltonian of our hybrid system can be written as

$$\hat{H}(t) = \frac{1}{2}m\dot{x}^2 + \frac{1}{2}m\omega_0^2 x^2 + E_{\mathrm{ex}}^0 \frac{\hat{\sigma}_z}{2} + \left.\frac{\partial E_{\mathrm{ex}}}{\partial x}\right|_{x=0} x\,\frac{\hat{\sigma}_z}{2}, \qquad (5.1)$$

where the first two terms describe the mechanical energy of the unperturbed NW, the third term describes the emission energy of the unperturbed QD, and the last one describes the opto-mechanical interaction. In the equation, m is the NW effective mass, E_{ex}^0 is the transition energy of a QD exciton for the NW at its rest position, $\hat{\sigma}_z = |e\rangle\langle e| - |g\rangle\langle g|$ is the Pauli operator of the two-level system, and $(\partial E_{\mathrm{ex}}/\partial x)|_{x=0}$ is the opto-mechanical coupling parameter at the NW rest position. The NW motion produces a time-varying deformation of the NW's crystalline structure, in turn altering the energy levels of the embedded QDs via a deformation potential, and resulting in a time-varying shift in the QD exciton emission energies. The sign and

magnitude of this shift under compressive or tensile strain depend on the localization of the QD within the NW cross section and possibly on intrinsic properties of each QD [122].

To evaluate the strength of the opto-mechanical coupling, we extract the PL profiles of the exciton lines for various values of the drive V_{PZT}, e.g. Fig. 5.8(a). The profiles are then fit with a Lorentzian whose central energy E_{ex}^0 is modulated by a sinusoid of amplitude δE_{ex} [28]. In fact, during half an oscillation period of the NW, the QD luminescence feels a succession of blue- and red-shift, whose time-integrated emission can be modeled as:

$$n_{\mathrm{d}}(E_{\mathrm{ex}}, \omega_0) = n_0 \frac{\omega_0}{\pi} \int_0^{\pi/\omega_0} \frac{\hbar^2 \Gamma^2}{(E_{\mathrm{ex}} - E_{\mathrm{ex}}^0 - \delta E_{\mathrm{ex}} \cos \omega_0 t)^2 + \hbar^2 \Gamma^2} \, \mathrm{d}t. \quad (5.2)$$

Here n_{d} indicates the photon counts per unit time, while n_0 and $\hbar\Gamma$ are the intrinsic QD photon counts and emission linewidth (FWHM), which can be measured from the QD PL spectrum in absence of mechanical excitation (inset of Fig. 5.6). Using our interferometer measurements (Fig. 5.4(b)), we then relate the displacement amplitude x_{osc} of the NW free end with the amplitude δE_{ex} extracted from the fit. The result, displayed in Fig. 5.8(b) for QD 2 (which resides in the same optical spot as QD 1), shows that in the linear regime of mechanical excitation, δE_{ex} is also linear in x_{osc}. A fit to this data provides an opto-mechanical coupling parameter $(\partial E_{\mathrm{ex}}/\partial x)|_{x=0} = 9.9 \pm 0.7 \, \mu\mathrm{eV/nm}$, which is one of the largest observed in our measurements.

5.4.2 Deformation Potential Model

The application of mechanical strain to the NW alters the lattice constant and the symmetry of the solid. These effects, in turn, cause significant changes in the electronic band structure that manifest themselves in the optical properties. The isotropic and deviatoric components of the strain (see Section 1.4.1) both contribute to such opto-mechanical coupling, with a weight given by their respective deformation potential, conventionally indicated as a for the isotropic deformation and d for the deviatoric component induced by a stress along $\langle 1\,1\,1 \rangle$ [123, 124].

In a recent work, Signorello and collaborators have measured the deformation potentials and the Poisson's ratio for Zinc-Blende GaAs/AlGaAs core-shell NWs – without embedded QDs – grown along $\langle 1\,1\,1 \rangle$, as in our case, at a temperature of 100 K [47]. The measured values are reported in Table 5.1.

The brightest exciton transition in our QDs concerns the conduction and the heavy-hole bands, each responding in a different way to the applied strain. The variation of the energy gap between these bands ($\Delta E^{\mathrm{C\text{-}HH}}$) under me-

Parameter	Value	Unit
ν	0.16 ± 0.04	
a	-8.6 ± 0.7	eV
d	-5.2 ± 0.7	eV

Table 5.1 │ **Electro-mechanical material parameters.** The values have been measured for Zinc-Blende GaAs/AlGaAs core-shell NWs grown along $\langle 1\,1\,1 \rangle$, at a temperature of 100 K. Taken from Ref. [47].

chanical excitation can be connected to the axial strain $\varepsilon_\parallel$ through the following model [44, 123]:

$$\Delta E^{\text{C-HH}} = \left[(1 - 2\nu)\, a + \frac{1}{\sqrt{3}}(1 + \nu)\, d \right] \varepsilon_\parallel. \tag{5.3}$$

From the FEM of the NW strain tensor, reported in Section 1.5.3, we extract the profile of $\varepsilon_\parallel$ along $\hat{z}$ corresponding to the lowest perpendicular mode, for a given displacement of the NW free end. The graph in Fig. 5.9 shows such a plot for $\varepsilon_\parallel$ at 10 nm below the NW surface, a distance where the QDs best coupled to strain are located. The red spot, in particular, marks the position where the QDs analyzed in this chapter are placed, $2.0 \pm 0.3\,\mu\text{m}$ away from the clamped edge of the NW. Inserting the value of $\varepsilon_\parallel$ at the QD position into the Eq. (5.3), we obtain a displacement-dependent energy shift of $13 \pm 2\,\mu\text{eV/nm}$. Though this estimation does not take into account the detailed QD band structure, the value we have found is close to our experimental result $(9.9 \pm 0.7\,\mu\text{eV/nm})$, therefore corroborating the strain-dependence of the band structure as the dominant coupling mechanism.

5.4.3 QD Stroboscopy

We study the time evolution of the QD exciton energy shift by acquiring stroboscopic PL spectra [27, 116]. As shown schematically in Fig. 5.10, two synchronized and isochronous signals drive the NW on resonance through the PZT and, using an acousto-optic modulator (AOM), chop the laser excitation with a 5% duty-cycle. The QDs are therefore excited only for 5% of the mechanical oscillation period of the NW. By recording PL spectra as a function of the phase between the two modulation signals, as shown in Fig. 5.11, we explore the temporal evolution of the QD exciton lines during a NW oscillation period.

This experiment reveals exciton lines, such as those of QD 1 and QD 2 in Fig. 5.11, that respond to the mechanical oscillation of the NW with
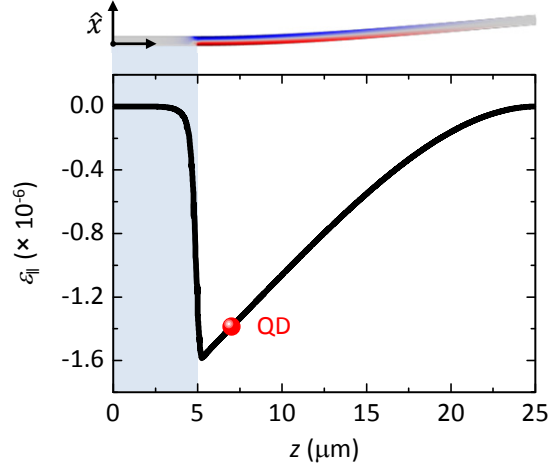
Figure 5.9 | Strain profile along $\hat{z}$. The strain component $\varepsilon_\parallel$ at 10 nm below the NW surface is plotted for the NW free-end displaced by 1 nm along $\hat{x}$, for the lowest perpendicular mode. The shaded area from $z = 0$ to $z = 5\,\mu m$ marks the region of the NW which is clamped to the substrate. The red spot at $z = 2.0 \pm 0.3\,\mu m$ from the edge of the clamped region marks the position where the QDs analyzed in this chapter are located. The upper inset shows the mode shape in consideration, with the strain amplitude in color scale as in Fig. 1.10.

opposite shifts in emission energy. The shifts in energy induced by strain are a consequence of the change in the fundamental bands resulting from the compression or extension of the lattice constant. Therefore, for a given strain, exciton transitions from the same QD should show energy shifts of the same sign and similar magnitude. Conversely, emission lines showing drastically different shift amplitudes or even shifts with different signs correspond to QDs located at different positions within the NW cross-section. In particular, two identical QDs within the same optical collection spot, located on opposite sides of the NW neutral axis, result in opposing strains produced for the same cantilever free-end displacement. On the other hand, differences in the extension and composition of each QD may also account for the varying responses to NW motion [122]. Alternatively, randomly distributed QDs in the shell of the NW, as postulated by Weiß *et al.*, may also produce such variations [116]. In any case, when two spatially and spectrally close QD excitons display strong opto-mechanical couplings of opposite sign, their energies may become degenerate for a particular time in the oscillation period (or equivalently for a particular position of the NW free end), as for the spectral lines outlined by the dashed circle in Fig. 5.11. In the future, exploiting this mechanically mediated tuning may allow us to couple two nearby QDs within a single NW. In addition, the sinusoidal time evolution of the PL spectral lines emerging from the measurement provides a confirmation of the mechanical origin of the QD emission broadening. Note also
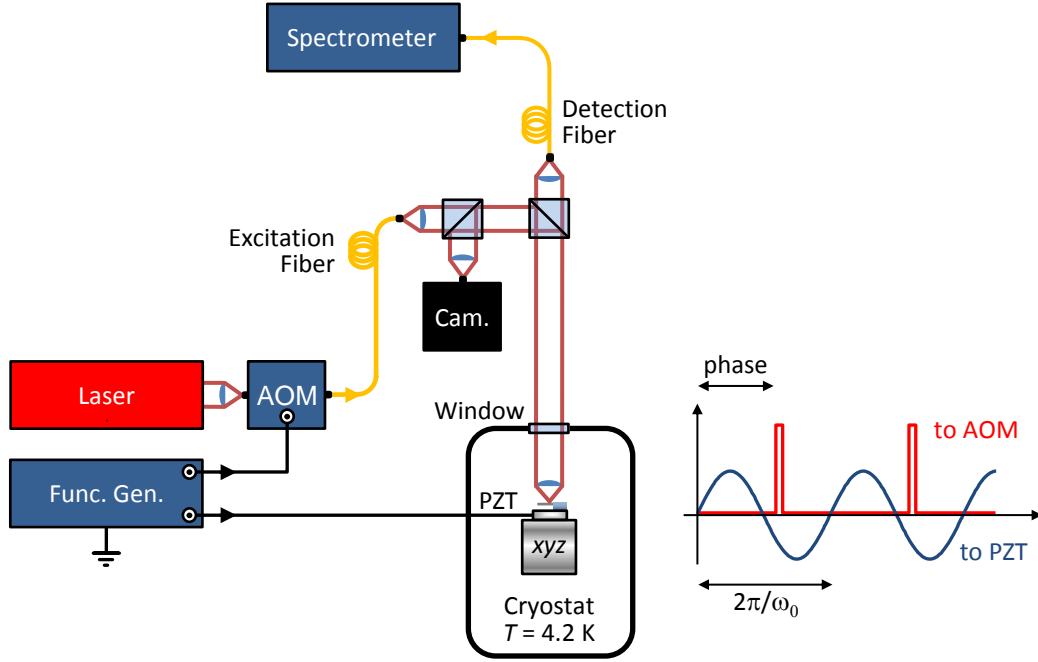
Figure 5.10 | **Scheme of the setup for QD stroboscopy.** Two synchronized and isochronous signals from a function generator are used to drive the NW on resonance and to modulate the QD excitation with a 5% duty-cycle, by means of an AOM.

that the modulation of the QD energy has no measurable influence on the corresponding PL intensity.

5.5 Conclusion and Outlook

In order to compare our results with other hybrid quantum systems [27, 37], the opto-mechanical interaction described in Eq. (5.1) can also be expressed in terms of the coupling rate

$$ \lambda \equiv \frac{1}{2\hbar} \left. \frac{\partial E_{\mathrm{ex}}}{\partial x} \right|_{x=0} x_{\mathrm{zpf}}, \tag{5.4} $$

which is the exciton frequency shift per vibrational quantum. Using the FEM of the NW, we calculate its effective mass $m = (3.5 \pm 0.7) \times 10^{-15}$ kg, where the error is dominated by the measurement imprecision of the NW thickness (see Section 1.5.3). This result, combined with knowledge of ω_0, allows us to calculate $x_{\mathrm{zpf}} = (5.5 \pm 0.6) \times 10^{-14}$ m. Therefore, for QD 2, the coupling rate $\lambda/(2\pi) = 66 \pm 12$ kHz. This opto-mechanical coupling rate is similar to that recently measured by Yeo *et al.* [27] for etched nano-pillars containing
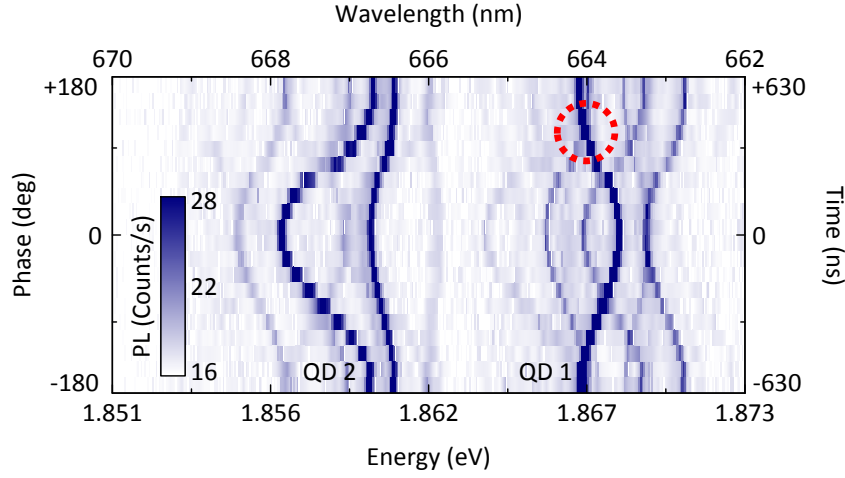
Figure 5.11 | **Time-resolved PL evolution.** Stroboscopic PL spectra of several neighboring QDs as a function of the phase (left axis) and the time delay (right axis) between the excitation-laser modulation and the PZT drive ($\omega = \omega_0$, $V_{\mathsf{PZT}} = 250$ mV$_{\mathsf{pk}}$). The dashed circle outlines two exciton spectral lines dynamically tuned to the same energy.

self-assembled QDs, where $\lambda/(2\pi) = 230 \pm 50$ kHz (note that in Ref. [27] $g_0 = 2\lambda$).

Both here and in Yeo *et al.*, the ratio λ/ω_0 is not far from unity, which makes these kinds of systems particularly promising for the quantum non-demolition (QND) readout of a QD state through a precise measurement of the NW displacement [27]. In particular, using Eqs. (5.1) and (5.4), we find that the displacement between the rest positions of the NW free end in the QD states $|g\rangle$ and $|e\rangle$ is $4x_{\mathrm{zpf}}\lambda/\omega_0$. In order to be observable, this displacement must be larger than x_{zpf}; in fact, at a finite temperature T, the displacement must be larger than the NW's thermal fluctuations x_{th}. In Section 1.6.2, we have found through the virial theorem the relation (1.59), which connects the fluctuations of the position operator $\hat{x}$ to the average phonon occupation number N. In terms of thermal fluctuations, we can then write, for the fundamental mode:

$$x_{\mathrm{th}}^2 = \langle N|\, \hat{x}^2\, |N\rangle = \frac{\hbar}{m\omega_0}\left(\frac{1}{2} + N\right) = x_{\mathrm{zpf}}^2(1 + 2N). \qquad (5.5)$$

Therefore, a determination of the QD state can be made through a displacement measurement, if $\lambda/\omega_0 > (1/4)\sqrt{1 + 2N}$. In the high temperature limit $k_BT \gg \hbar\omega_0$, the requirement is that $\lambda/\omega_0 > \sqrt{k_BT/(8\hbar\omega_0)}$. However, for our experimental parameters, the ratio λ/ω_0 is still 10^3 times too small for such effects to be observed.

Auffèves and Richard [17] have recently proposed an alternative approach to such a non-demolition measurement, which takes advantage of the high

Q of the NW oscillator. In their scheme, the QD is optically excited by a continuous-wave laser modulated at the NW resonance frequency. This process builds up, through constructive interference, a large coherent mechanical excitation of the NW. On resonance with a QD transition, the amplitude of the excitation is roughly Q times larger than the displacement difference calculated in the aforementioned static case. For our experimental parameters, this amplitude would be 6 times larger than the NW thermal fluctuations, making it detectable by a high-sensitivity interferometer [68]. It should be noted that a QND measurement also requires the time necessary to build up such a coherent phonon field (T_r) to be smaller than the quantum transition lifetime (τ_{ex}), which is not the case here ($T_r \approx 18$ ms, while $\tau_{\mathrm{ex}} \approx 1$ ns) nor in the experiment of Yeo *et al.* [27]. The use of a longer-lived QD state such as a dark exciton ($1\,\mu$s [125]) or a spin state (0.5 s [126]) could bring the system closer to the required lifetime. In addition, given a detection of the NW displacement with a large enough signal-to-noise ratio, T_r could be reduced using feedback damping, which can modify a mechanical oscillator's response time without affecting its intrinsic properties [32].

Our QD-in-NW system is a good candidate for investigating a possible interaction between the mechanics and a spin state. In presence of a magnetic field, the spin degeneracy of a QD exciton is removed. It has been demonstrated that the resulting Zeeman splitting can be tuned by an external electric field, which modifies the g-factor [127]. We expect a similar control over the splitting via the deformation potential induced by the NW vibration. Given the possibility of preparing a QD state in a specific spin polarization, for instance by resonant excitation [128], such a control would result in a spin-oscillator coupling, similar to what was recently demonstrated in NV centers in diamond resonators [29, 30].

We note that prospects of quantum control over a mechanical resonator, or proposals for using a mechanical resonator as a transducer for quantum information, require the hybrid interaction to be large compared to the rates at which the coupled systems decohere into their local environments [14, 31]. Some proposals require the condition of *large cooperativity* [129, 130]: $\lambda/\sqrt{\gamma_{\mathrm{ex}}\Gamma_{\mathrm{th}}} > 1$, where γ_{ex} is the decoherence rate of the quantum transition, in our case associated to a QD exciton (> 1 GHz [36]) and $\Gamma_{\mathrm{th}} = k_B T/(\hbar Q)$ is the mechanical heating rate. Using the values from this experiment, the cooperativity is 10^{-3}. Nevertheless, the QD-in-NW system is particularly promising, given that λ could be improved by working with a higher flexural mode of the NW. In fact, as demonstrated analytically in Section 1.4.1, and confirmed by the FEM in Section 1.5.3, the maximum strain in the NW scales for higher modes as the eigenfrequency. Improvements in the detection of higher modes should therefore provide an opto-mechanical coupling parameter increased as the strain. However, the coupling rate λ

also depends on the NW's zero-point motion $x_{\mathrm{zpf}} = \sqrt{\hbar/(2m_n\omega_n)}$. While the mode effective mass m_n does not depend in our geometry on n, the mode resonance frequency ω_n increases with n, by a factor 6 for the second order mode doublet with respect to the first one. This dependence implies an increase of λ by a factor 2 (or bigger) for the second order (or higher) flexural modes of the NW. Moreover, as pointed out also by Yeo *et al.*, realistic improvements of the size and shape of the NW should also lead to a significant increase of λ. In fact, from the relation (1.35) and from the expression of x_{zpf}, it results that λ scales with the NW diameter D, length L and volume V according to [27]:

$$\lambda \propto \frac{\beta_n \sqrt{D}}{L\sqrt{V}}. \tag{5.6}$$

Increasing the coupling thus requires decreasing the volume and the aspect ratio of the NW. By suitably modifying the NW dimensions and using a conical geometry, able to concentrate the elastic energy close to the clamped end, Yeo *et al.* estimate a coupling rate improved by a factor 40 [27]. Furthermore, the use of a doubly-clamped and short NW should combine the advantages of a lower aspect ratio with a significant increase of the parameter β_n (see Table 1.2). On the other hand, in the prospect of achieving a large cooperativity, the experiment could be carried out in a dilution refrigerator at $T = 10$ mK and the mechanical quality factor could be improved up to a few times 10^6, perhaps by surface treatment, as was demonstrated in Si cantilevers with similar aspect ratios [131], and by studying NWs directly clamped to their growth substrate [56].

Our monolithic opto-mechanical system constitutes a good candidate for recent proposals of a hybrid quantum system integrating an optical cavity, a quantum two-level system and a mechanical resonator [132–135]. Cavity quantum electrodynamics (QED) experiments have revealed successful in exploring the light-matter interaction at the quantum level in atomic physics [136]. A growing interest is now emerging for hybrid systems establishing a bridge between QED and opto-mechanics, in a platform interfacing photons, phonons, and artificial atoms. Our QD-in-NW system could for instance be included in a high finesse miniaturized optical cavity, as those demonstrated by Favero *et al.* [137] and Flowers-Jacobs *et al.* [138]. Such a system would take advantage of a series of factors, like our intrinsically strong QD-oscillator interaction, the high opto-mechanical coupling offered by the cavity, and its compactness, stability, and compatibility with cryogenic operation. The resulting tripartite quantum system would offer enhanced effective interactions between the mechanics and the cavity field, leading for instance to efficient cooling of the mechanical resonator to the ground state, even in a regime in which standard radiation pressure cooling would be in-

efficient [134], like in the unresolved sideband regime (see Section 3.1). In addition, the emergence of both phonon bunching and anti-bunching has been prospected in such a coupled system [132].

The sensitivity of the QDs in our system to the resonant vibration of the NW could also be used to reveal displacement variations due to the application of electrical or magnetic forces or to a change of the NW mass. This fact opens the perspective of using our QD-in-NW system as an integrated force probe or as a nanomechanical mass sensor. By measuring the QD PL, one could monitor the NW motion in a technically simpler way than optical interferometry [68, 137–140] or other schemes [141–143].

We estimate the sensitivity of our apparatus as a displacement transducer and as a force or strain detector. For this purpose, we first measure, for a QD emission line, the intrinsic fluctuation in time of the photon count in a narrow spectral bin around the transition energy E_{ex}^0. The amplitude of such fluctuation depends on the bin size and on the integration time τ. An external force applied to the NW produces, through the deformation potential coupling, a variation of the QD photon count in a given spectral interval. For such a force to be detectable, the induced photon count variation has to be bigger than the intrinsic fluctuation. This count variation is in turn a direct consequence of the emission energy modulation, whose amplitude δE_{ex} can be calculated through the model described in Eq. (5.2). From the opto-mechanical coupling parameter $(\partial E_{\mathrm{ex}}/\partial x)|_{x=0}$ measured for QD 2, we are then able to convert the emission energy modulation into a root-mean-squared displacement x_{rms} of the NW free-end. Finally, by multiplying such displacement to the square root of τ, we obtain a displacement sensitivity $\approx$ 3 nm Hz$^{-1/2}$. Note that this result is limited, in particular, by the resolution of our spectrometer, equal to 60 μeV. On the other hand, the sensitivity could be improved by 4 orders of magnitude by means of resonant laser spectroscopy [128]. The applied force is proportional to the NW displacement x_{rms} through the spring constant $k = m\omega_0^2 = 90 \pm 20$ mN/m. Therefore we are able to estimate a force sensitivity $\approx$ 300 pN Hz$^{-1/2}$. Our setup is also sensitive to strain variations in the NW. Through the FEM of the NW, relating the strain to the NW free-end displacement, it is possible to express a strain sensitivity of our setup, $\approx 5 \times 10^{-6}$ strain Hz$^{-1/2}$. This result is of the same order of the sensitivity recently estimated for strain-mediated coupling of a diamond cantilever to the spin of an embedded NV center [30].

In summary, in this Chapter we demonstrate an *as-grown* opto-mechanical system produced entirely by bottom-up self-assembly. The structure's intrinsic properties couple multiple QDs to the same NW mechanical oscillator. This interaction enables the tuning of QD energies over a broad range exceeding 14 meV, opening the way for mechanically induced coupling between different QDs in the NW. Our approach opens up the prospect of us-

ing QDs to probe and control the mechanical state of a NW, or conversely of making a quantum non-demolition readout of a QD state through a position measurement.

6 | Conclusion

The coupling of nanomechanical resonators to controllable quantum systems represents a growing and promising area of research. Recent advances in this field have brought to astonishing results, such as the initialization of a mechanical resonator into its quantum ground state [12–14] and even the preparation of non-classical coherent states of motion [15]. These achievements open up appealing scenarios to quantum information technologies and to the exploration of the quantum-classical boundary [27]. From an application perspective, such quantum-mechanical *hybrid* systems provide a versatile and attractive tool for a variety of precision measurements, like ultra-sensitive detection of force [3], mass [4], and displacement [5,6].

Quantum control over a mechanical resonator, or, conversely, the prospect of using resonator's motion for probing quantum states, both involve some tight requirements. First of all, the interaction between the mechanics and its quantum partner has to be large on the scale of the decoherence rates of the coupled systems. In most cases, the coupling mechanism has to be activated by engineering the resonator with electrodes, magnets, or mirrors, or by using tailored laser fields. For this reason, the search for a strong coupling typically competes with the requirement of overcoming decoherence effects. In addition, for quantum effects to be observable, strong coupling has to be accompanied by the preparation of zero entropy initial states, for instance by cooling the resonator into its ground state of motion.

The motivation pursued by this thesis is to contribute to the inspiring field of hybrid systems by walking through each of the aforementioned directions. We in fact demonstrate a promising system in which optically active quantum dots, embedded in fully self-assembled core-shell nanowires, are coupled to the nanowire motion. Mechanical vibrations of the nanowire modulate the quantum dot emission energy over a broad range exceeding 14 meV, by means of deformation potential coupling. In our system, therefore, both the coupling mechanism and the quantum states themselves are intrinsic to the resonator's structure. Besides revealing unusually strong, such a *built-in* opto-mechanical interaction produces a hybrid system whose inherent coherence is unspoiled by any functionalization or external field and whose fabrication is simpler than top-down techniques.

We further demonstrate the use of a quantum point contact as a displacement transducer to measure and control the low-temperature thermal motion of a nearby micromechanical cantilever. We show that by including the QPC in a suitable feedback loop, we are able to cool the cantilever's fundamental mechanical mode down to the level of the measurement noise, achieving a squashing of the QPC noise at high gain. Due to its off-board design, our system is particularly versatile and suitable to force-sensing applications. Since the QPC transducer is sensitive to local modifications of the nearby electric field, our approach is in principle compatible with any nanoscale resonator, without requiring any functionalization to activate the coupling. By improving the performance of the QPC as a one-dimensional conductor and the cantilever-QPC capacitive coupling, our system has the potential to achieve quantum-limited displacement resolution and ground state cooling. We then report on some ongoing attempts to overcome the current limitations and couple mechanical motion to different mesoscopic transport devices.

We remark that our demonstration of an *as-grown* quantum-dot-in-nanowire hybrid system opens up bright prospects on future experiments, as also testified by the very recent ferment of the scientific community around this topic [27, 29, 30]. We find that the opto-mechanical coupling rate is not far from the nanowire mechanical frequency. This fact makes our system particularly promising for the quantum non-demolition readout of a quantum dot state through a measurement of the nanowire position [17]. On the other hand, we show that the coupling can be further optimized, and the nanowire mechanical heating rate reduced, thus disclosing the captivating perspective of using quantum dots to probe and control the mechanical state of a nanowire. In this context, it would be important to investigate a possible spin-oscillator coupling in our system, given the long coherence time offered by a spin state in a quantum dot. The wide range of control over the quantum dots emission energy and the ability to tune two neighboring dots into resonance pave the way to mechanically induced emitter-emitter coupling. In addition, our monolithic opto-mechanical system constitutes a good candidate for recent proposals of a tripartite hybrid system, which would integrate an optical cavity, a quantum two-level system and a mechanical resonator [132–135]. The intrinsically strong coupling between the quantum dots and the nanowire motion would enhance the interaction between the mechanics and the cavity field, leading for instance to efficient cooling of the resonator to the ground state. Finally, the quantum dot sensitivity to the nanowire resonant vibration could also support the use of our system as an integrated force probe or as a nanomechanical mass sensor. In other words, the results reported here constitute not only a relevant proof-of-principle, moreover they open up intriguing challenges in future research.

A │ QPC Fabrication Protocol

CLEANING	TCE, Acetone, Methanol, 5' each in US	
PRE-BAKE	120°C, 5'	
SPIN-COATING	Resist: ma-N415, spin at 6000 rpm, 45'', ramp = 6''	
BAKING	93°C, 90''	**UVL: MESA**
EXPOSURE	Hard contact for 6'', lamp on CH1, 14'' (CH2, 7'')	
DEVELOPING	Ma-D 332 S, 2' + rinse in H_2O, 20''	
PROFILOMETER	Measure resist thickness	
ETCHING	$H_2SO_4 : H_2O_2 : H_2O = 1 : 8 : 240$, 20'' for 80 nm	
REMOVE RESIST	NMP at 50°, 5' in US	
CLEANING	TCE, Acetone, Methanol, 5' each in US	
PRE-BAKE	120°C, 5'	
SPIN-COATING	Resist: ma-N415, spin at 6000 rpm, 45'', ramp = 6''	
BAKING	93°C, 90''	
EXPOSURE	Hard contact for 6'', lamp on CH1, 14'' (CH2, 7'')	
DEVELOPING	Ma-D 332 S, 2' + rinse in H_2O, 20''	
PLASMA ETCHING	Base p = $5x10^{-5}$ mbar, 16% O_2 at 250 mbar, 30 W, for 1'	**UVL: OHMIC CONTACTS**
ETCHING	HCl 37%, 5'' + rinse in H_2O, 15''	
EVAPORATION	Ni / Ge / Au / Ni = 2 / 26 / 54 / 15 nm, for totally 97 nm	
LIFT-OFF	NMP at 50°C (eventually US at low power, i.e. 20%)	
CLEANING	TCE, Acetone, Methanol, 5' each, no US	
ANNEALING	350°C, 120'' + 420°C, 50''	
OHMICS CHECK-UP	Check the linearity and the resistance of the contacts with needle probes	

SPIN-COATING	Resist: custom PMMA for a 130-nm film, spin at 4000 rpm, 40'', ramp = 4''	EBL: GATES
BAKING	180°C, 7'	
EXPOSURE	Aperture = 10 μm, e-gun potential = 20 kV, field size = 250 μm, step size = 8 nm, dose = 240/130/160 μAs/cm^2 (QPC/leads/markers)	
DEVELOPING	MIBK : IPA : MEK = 1 : 3 : 1,3%, 75'' + rinse in IPA, 15''	
EVAPORATION	Ti/Au = 5/15 nm	
LIFT-OFF	NMP at 50°C, no US	
CLEANING	TCE, Acetone, Methanol, 5' each, no US	UVL: LEADS
PRE-BAKE	120°C, 5'	
SPIN-COATING	Resist: ma-N415, spin at 6000 rpm, 45'', ramp = 6''	
BAKING	93°C, 90''	
EXPOSURE	Hard contact for 6'', lamp on CH1, 14'' (CH2, 7'')	
DEVELOPING	Ma-D 332 S, 2' + rinse in H$_2$O, 20''	
EVAPORATION	Ti/Au = 10 / 130 nm	
LIFT-OFF	NMP at 50°C (eventually US at low power, i.e. 20%)	
CLEAVING	The QPC must be within 150 μm of the edge of the sample	
Au-BONDING	Glue the sample on the chip carrier with PMMA and bake it at 50°C for 20'. Avoid static discharge!	

B | QPC Control and Acquisition Electronics
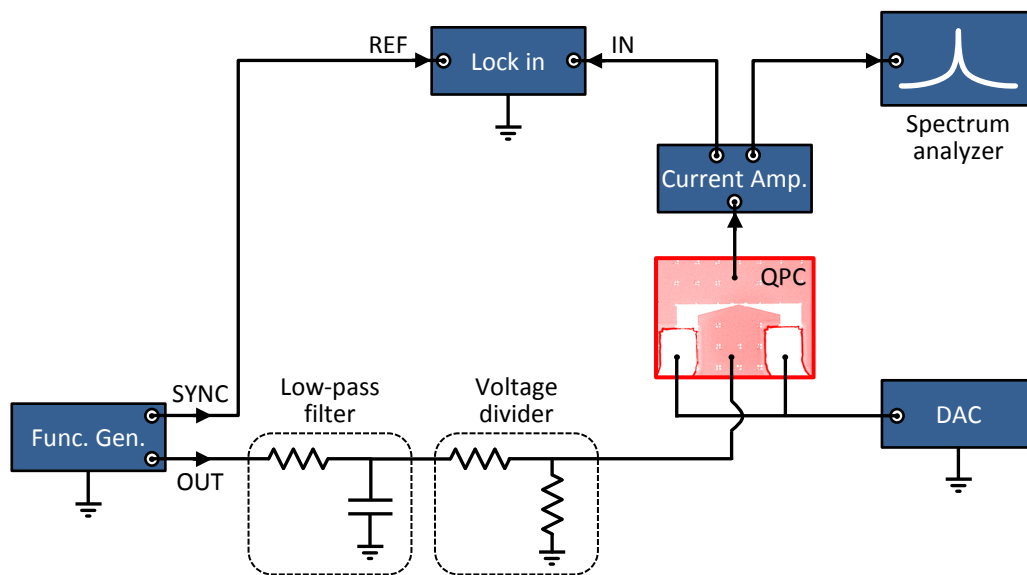
C | Suspended-NW SET Fabrication Protocol

CLEANING	TCE, Acetone, Methanol, 5' each in US	**EBL: FINGER GATES & MARKERS**
PRE-BAKE	120°, 5'	
SPIN-COATING	Resist: custom PMMA for a 100-nm film, spin at 6000 rpm, 40'',ramp = 6'	
BAKING	180°C, 7'	
EXPOSURE	Gates/markers: aperture = 7.5 µm, e-gun potential = 30 kV, field size = 50/400 µm , step size = 1/6 nm, dose = 600/360 µAs/cm^2	
DEVELOPING	MIBK : IPA : MEK = 1 : 3 : 1,3%, 75'' + rinse in IPA, 15''	
EVAPORATION	Ti/Au = 5/15 nm	
LIFT-OFF	Acetone	
CLEANING	IPA	**NW TRANSFER**
SPIN-COATING	Resist: EL-9, 6000 rpm, 60'', ramp = 6, for gap = 260 nm; EL-9:EL [1:1], 4000 rpm, 60'', ramp = 6, for gap = 100 nm; EL-9:EL [5:7], 4000 rpm, 60'', ramp = 6, for gap = 70 nm	
BAKING	175°C, 7'	
MICRO-MANIPULATION	Make a glass needle: all four weights, distance: 6(3), T_1=~65°C, T_2=~69°C. Transfer and place the NWs above the finger gates	

SPIN-COATING & BAKING	Resist: EL-9, 3200 rpm, 45'', ramp = 3; 175°C, 7'; PMMA 495, 4000 rpm, 45'', ramp = 4; 180°C, 45''; PMMA 950, 4000 rpm, 45'', ramp = 4; 180°C, 45'	
CLEAVING	The SETs must be within 150 μm of the sample edge	
CLEANING	IPA, 5'' in US	
CAD	Take pictures of the NW position, prepare the CAD	
EXPOSURE	Small/big features: aperture = 10/120 μm, e-gun potential = 20 kV, field size = 500/2000 μm, step size = 32/64 nm, dose = 220 μAs/cm^2	
DEVELOPING	MIBK : IPA : MEK = 1 : 3 : 1,3%, 90'' + rinse in IPA, 60''	
O$_2$ PLASMA ETCHING	Base p = 5x10^{-5} mbar, 16% O$_2$ at 25 mbar, 30 W, for 45''	
SULFUR PASSIVATION	0.5 ml of 1.56 M $(NH_4)_2S_x$ solution in 20 ml H_2O, 50°C water bath for 5' (position the chip upside-down)	
Ar PLASMA ETCHING	Load the sample into the sputtering unit. Ar plasma for 3'	
SPUTTERING	Gas flow: 30 sccm, p = 7. 5x10^{-5} mbar, current = 0.15 A, Ti/Au = 5'/2'30'' for 100 nm gap	
LIFT-OFF	Acetone, 10'	
CLEANING	IPA, Ethanol, keep in liquid!	
CPD	8 cycles to exchange Ethanol with liquid CO_2	
ANNEALING	150°C, 1' + 250°C, 5'	
Au-BONDING	Glue the sample on the chip carrier with silver paint (for back-gating). Avoid static discharge!	

EBL: ELECTRODES

D | Distribution of QD Exciton Energy Shifts

We analyze the distribution of energy shifts of PL lines from QDs located in the same position along the NW length (within the laser detection spot), and emitting in a spectral range of 30 meV, centered around 1.860 eV. This relatively narrow energy window restricts our analysis to QDs with similar size and composition. We consider the energy shift induced in the QDs by a resonant mechanical excitation of the NW. In order to exclude the effect of asymmetric energy modulation, due to the different response of the QD band structure under compressive or tensile stress [47, 121], we consider energy shifts only towards higher energies. The distribution of the data is plotted in Fig. D.1(a).

The experimental result is compared to two different models for the spatial distribution of the QDs in the shell of the NW. The first model, illustrated in Fig. D.1(b), assumes QDs located at the apexes of the NW hexagonal cross-section. The histogram in Fig. D.1(c), instead, results from a model of QDs uniformly distributed along the shell perimeter.

The experimental distribution conforms more closely to the model of QDs located at the apexes of the cross-section. Though not conclusive, this analysis lends support to the interpretation of the QD spatial distribution in our NW structures originally given by Heiss *et al.* [36] and recently confirmed by Fontana *et al.* [115]. The observed deviations from such a model can be explained as weak fluctuations of size and composition of the analyzed QDs [122], and to different distances from the center of the cross-section.
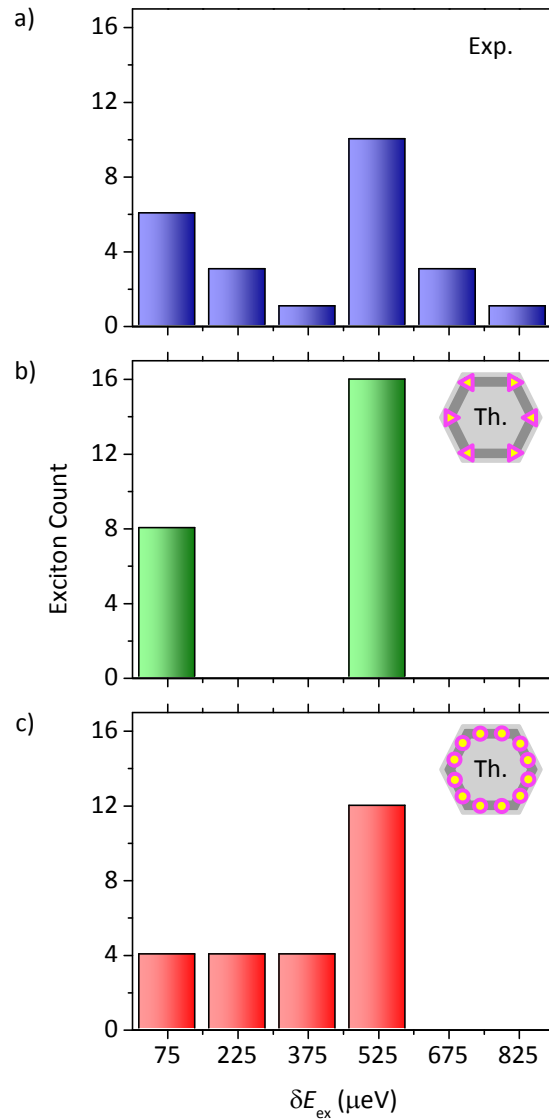
Figure D.1 | **Distributions of energy shifts.** (a) Experimental distribution of energy shifts for QDs emitting within a 30-meV spectral range and located at the same position along the NW length. (b) Model distribution for QDs located at the apexes of the NW shell. (c) Model distribution for QDs uniformly distributed along the shell perimeter. The two model distributions are normalized to the total exciton count of the experimental analysis.

Acknowledgments

Coming to the conclusion of my Ph.D. experience, I would like to acknowledge first of all the people that give me the honor of taking part to my Ph.D. defense committee. Thank you Dr. Heike Riel for having quickly accepted my invitation and for having saved your time to review my thesis. Thank you Prof. Richard Warburton for chairing my defense. Most of all, thank you Richard for allowing me to use your facility and to work with your group with my apparently visionary project, for sharing your deep insights into the experiment design and analysis and also for the many pleasant moments of humor and relax.

Naturally I would like to acknowledge the agencies that have funded my Ph.D., namely the Swiss National Science Foundation (SNSF) and the Kanton Aargau.

Going back with memory to my early days at the University of Basel, I cannot forget how the lab first appeared to me: nothing more than a big empty space with a large pit in the middle, and a funny bright yellow concrete pavement. The main working instrument, however, was already in its full productive capacity: the talent and great enthusiasm of my Ph.D. advisor, Prof. Martino Poggio. Later in the following months, the first hardware started arriving, mainly the precious ^{3}He cryostat, which we had to struggle to clean and test and make its vacuum chamber completely oil-free. My colleague Phani Peddibhotla was already there, devoting most of his time to programming the control software, which later everybody in the lab would have taken advantage of. Martino's excitement to build up a new enterprise from scratch and his excellent organization and expertise were contagious to everyone approaching to him. He has been for the first generation of his students much more than just a Ph.D. advisor. We have sort of grown up together in these years: from the drinks to celebrate the first achievements in the lab, to the wonderful party for his wedding, and the bib for his child. Thank you Martino for sharing all these things with us. I have learned working in science, analyzing problems in every detail, and communicating results with a decent level of (American) English mainly from you. The hard core of the Poggio Group was completed when also Dennis Weber and Dr. Fei Xue joined later in the same year. I found in them a valuable

support for sharing my learning process in clean-room fabrication, besides very good company for life outside the lab. Thanks to his expertise, Fei gave a crucial input to build up the lab, and was always for me source of important technical advices. Dennis, having started his Ph.D. parallel to me, has shared with me most of the events that have characterized my staying in Basel and has strongly contributed to creating an enjoyable and stimulating working environment. Thank you Dennis for being always available to answer my questions and help me solving any trouble with my PC.

After having acquired some experience in the lab, I started supervising a younger promising student, which later joined the group: Andrea Mehlin. I hope I was able to give her good advices and support; for sure crucial has been the support she has given me, with her methodical organization and passion for what she does, and for sharing time after work to recover from the discomfort that often accompanies work in a lab. Dr. Hari Solanki has later joined the group, providing the lab with his enormous experience in clean-room processing of sophisticated devices. I would like to acknowledge and highlight the hard work of Benedikt Herzog, who has been able, as a Master's student, to design and set up a very useful experimental system operating at room temperature. I am grateful also to all the other components of the Poggio group for their scientific contribution and for keeping our group always compact and jovial: thank you Arne for your good computer maintenance and very helpful advices, Nicola for the nice animation of the experimental data, and thank you Davide, Floris, Denis, and Marcus.

During my Ph.D. I've been working on several projects which required the important contribution of many people inside and out of the Department of Physics. I would like to acknowledge in particular the group of Prof. Dominik Zumbühl, and expecially Dr. Charulata Barge and Dr. Florian Dettwiler, for introducing me and providing support in the local clean-room. Thanks to the group of Prof. Christian Schönenberger, and in particular to Jörg Gramich for his infinite patience in assisting at the SEM. Thanks to the group of Prof. Ernst Meyer, and in particular to Dr. Marcin Kisiel for useful discussions about mechanical dissipation and friction. Thank you Prof. Patrick Maletinsky and Dr. Jean Teissier for very useful hints during our journal clubs and for introducing me to the elaborated world of finite element simulations. And again, thanks to the group of Prof. Richard Warburton, and in particular to Gunter Wüst, who has introduced me to photoluminescence spectroscopy, to Dr. Mathieu Munsch, who has provided important insights and has carefully reviewed my second manuscript, to Dr. Adreas Kuhlmann for important suggestions, to Jonathan Prechtel, Lukas Greuter, and Dr. Sebastian Starosielec for technical assistance. I am very grateful also to the machine shop and to the electronics shop of the Department, in the name of their directors Sascha Martin and Michael Steinacher: without their con-

tribution and expertise many of the experiments in our lab would have not been successful. It is merit of Dominik Sifrig if everybody in the Department gets liquid helium delivered on time, often also on short notice. I would like to thank the administrative personnel of the Department: Germaine Weaver, Barbara Kammermann, and Astrid Kalt for always being nice and helpful, and in particular Audrey Fischer, for her fruitful advices coming from her rich experience. Outside of the Department, I had the honor and pleasure to collaborate with Prof. David Awschalom and Dr. Shawn Mack, Prof. Alex Holleitner and Marcus Stallhofer, Prof. Klaus Ensslin and Dr. Sarah Hellmüller, and finally with the group of Prof. Anna Fontcuberta i Morral, and in particular with her student Yannik Fontana. Anna and Yannik have given the input and provided the material for the opto-mechanics experiment with self-assembled nanowires. Besides this, they have contributed with their ideas and positive spirit to enjoy also the free time during conferences.

Especially during the last part of my Ph.D., a person in particular has strongly contributed to a fruitful completion of my work. *Dankeschön* Andrea for supporting me, being patient while waiting for me, and never doubting of my capabilities. Thank you for reviewing my thesis, for criticizing my figures, and following me always, *"wherever I go"*.

Last but not least, I want to say *Grazie* to my family, for believing in me and being there for me, always.

Basel, August 22, 2014

Michele Montinaro

References

[1] Binnig, G., Quate, C. F. and Gerber, C. Atomic force microscope. *Physical Review Letters* **56**, 930–933 (1986).

[2] Bordag, M., Mohideen, U. and Mostepanenko, V. M. New developments in the Casimir effect. *Physics Reports* **353**, 1–205 (2001).

[3] Rugar, D., Budakian, R., Mamin, H. J. and Chui, B. W. Single spin detection by magnetic resonance force microscopy. *Nature* **430**, 329–332 (2004).

[4] Chaste, J., Eichler, A., Moser, J., Ceballos, G., Rurali, R. and Bachtold, A. A nanomechanical mass sensor with yoctogram resolution. *Nature Nanotechnology* **7**, 301–304 (2012).

[5] Teufel, J. D., Donner, T., Castellanos-Beltran, M. A., Harlow, J. W. and Lehnert, K. W. Nanomechanical motion measured with an imprecision below that at the standard quantum limit. *Nature Nanotechnology* **4**, 820–823 (2009).

[6] Anetsberger, G., Gavartin, E., Arcizet, O., Unterreithmeier, Q. P., Weig, E. M., Gorodetsky, M. L., Kotthaus, J. P. and Kippenberg, T. J. Measuring nanomechanical motion with an imprecision below the standard quantum limit. *Physical Review A* **82**, 061804 (2010).

[7] Clerk, A. A., Devoret, M. H., Girvin, S. M., Marquardt, F. and Schoelkopf, R. J. Introduction to quantum noise, measurement, and amplification. *Reviews of Modern Physics* **82**, 1155–1208 (2010).

[8] Smullin, S. J., Geraci, A. A., Weld, D. M., Chiaverini, J., Holmes, S. and Kapitulnik, A. Constraints on Yukawa-type deviations from Newtonian gravity at 20 microns. *Physical Review D* **72**, 122001 (2005).

[9] Whitcomb, S. E. Ground-based gravitational-wave detection: now and future. *Classical and Quantum Gravity* **25**, 114013 (2008).

[10] Bose, S., Jacobs, K. and Knight, P. L. Scheme to probe the decoherence of a macroscopic object. *Physical Review A* **59**, 3204–3210 (1999).

[11] Treutlein, P. Optomechanics: A strained couple. *Nature Nanotechnology* **9**, 99–100 (2014).

[12] Teufel, J. D., Donner, T., Li, D., Harlow, J. W., Allman, M. S., Cicak, K., Sirois, A. J., Whittaker, J. D., Lehnert, K. W. and Simmonds, R. W. Sideband cooling of micromechanical motion to the quantum ground state. *Nature* **475**, 359–363 (2011).

[13] Chan, J., Alegre, T. P. M., Safavi-Naeini, A. H., Hill, J. T., Krause, A., Gröblacher, S., Aspelmeyer, M. and Painter, O. Laser cooling of a nanomechanical oscillator into its quantum ground state. *Nature* **478**, 89–92 (2011).

[14] Verhagen, E., Deléglise, S., Weis, S., Schliesser, A. and Kippenberg, T. J. Quantum-coherent coupling of a mechanical oscillator to an optical cavity mode. *Nature* **482**, 63–67 (2012).

[15] O'Connell, A. D., Hofheinz, M., Ansmann, M., Bialczak, R. C., Lenander, M., Lucero, E., Neeley, M., Sank, D., Wang, H., Weides, M., Wenner, J., Martinis, J. M. and Cleland, A. N. Quantum ground state and single-phonon control of a mechanical resonator. *Nature* **464**, 697–703 (2010).

[16] Braginsky, V. B., Vorontsov, Y. I. and Thorne, K. S. Quantum nondemolition measurements. *Science* **209**, 547–557 (1980).

[17] Auffèves, A. and Richard, M. Optical driving of macroscopic mechanical motion by a single two-level system. *Physical Review A* **90**, 023818 (2014).

[18] Poot, M. and van der Zant, H. S. J. Mechanical systems in the quantum regime. *Physics Reports* **511**, 273–335 (2012).

[19] Rabl, P., Kolkowitz, S. J., Koppens, F. H. L., Harris, J. G. E., Zoller, P. and Lukin, M. D. A quantum spin transducer based on nanoelectromechanical resonator arrays. *Nature Physics* **6**, 602–608 (2010).

[20] Kolkowitz, S., Bleszynski Jayich, A. C., Unterreithmeier, Q. P., Bennett, S. D., Rabl, P., Harris, J. G. E. and Lukin, M. D. Coherent sensing of a mechanical resonator with a single-spin qubit. *Science* **335**, 1603–1606 (2012).

[21] McGee, S. A., Meiser, D., Regal, C. A., Lehnert, K. W. and Holland, M. J. Mechanical resonators for storage and transfer of electrical and optical quantum states. *Physical Review A* **87**, 053818 (2013).

[22] Palomaki, T. A., Harlow, J. W., Teufel, J. D., Simmonds, R. W. and Lehnert, K. W. Coherent state transfer between itinerant microwave fields and a mechanical oscillator. *Nature* **495**, 210–214 (2013).

[23] Bochmann, J., Vainsencher, A., Awschalom, D. D. and Cleland, A. N. Nanomechanical coupling between microwave and optical photons. *Nature Physics* **9**, 712–716 (2013).

[24] Armour, A. D., Blencowe, M. P. and Schwab, K. C. Entanglement and decoherence of a micromechanical resonator via coupling to a cooper-pair box. *Physical Review Letters* **88**, 148301 (2002).

[25] Camerer, S., Korppi, M., Jöckel, A., Hunger, D., Hänsch, T. W. and Treutlein, P. Realization of an optomechanical interface between ultracold atoms and a membrane. *Physical Review Letters* **107**, 223001 (2011).

[26] Bennett, S. D., Cockins, L., Miyahara, Y., Grütter, P. and Clerk, A. A. Strong electromechanical coupling of an atomic force microscope cantilever to a quantum dot. *Physical Review Letters* **104**, 017203 (2010).

[27] Yeo, I., de Assis, P.-L., Gloppe, A., Dupont-Ferrier, E., Verlot, P., Malik, N. S., Dupuy, E., Claudon, J., Gérard, J.-M., Auffèves, A., Nogues, G., Seidelin, S., Poizat, J.-P., Arcizet, O. and Richard, M. Strain-mediated coupling in a quantum dot-mechanical oscillator hybrid system. *Nature Nanotechnology* **9**, 106–110 (2014).

[28] Arcizet, O., Jacques, V., Siria, A., Poncharal, P., Vincent, P. and Seidelin, S. A single nitrogen-vacancy defect coupled to a nanomechanical oscillator. *Nature Physics* **7**, 879–883 (2011).

[29] Teissier, J., Barfuss, A., Appel, P., Neu, E. and Maletinsky, P. Strain coupling of a nitrogen-vacancy center spin to a diamond mechanical oscillator. *Physical Review Letters* **113**, 020503 (2014).

[30] Ovartchaiyapong, P., Lee, K. W., Myers, B. A. and Bleszynski Jayich, A. C. Dynamic strain-mediated coupling of a single diamond spin to a mechanical resonator. *Nature Communications* **5** (2014).

[31] Gröblacher, S., Hammerer, K., Vanner, M. R. and Aspelmeyer, M. Observation of strong coupling between a micromechanical resonator and an optical cavity field. *Nature* **460**, 724–727 (2009).

[32] Poggio, M., Degen, C. L., Mamin, H. J. and Rugar, D. Feedback cooling of a cantilever's fundamental mode below 5 mK. *Physical Review Letters* **99**, 017201 (2007).

[33] Montinaro, M., Mehlin, A., Solanki, H. S., Peddibhotla, P., Mack, S., Awschalom, D. D. and Poggio, M. Feedback cooling of cantilever motion using a quantum point contact transducer. *Applied Physics Letters* **101**, 133104 (2012).

[34] Montinaro, M., Wüst, G., Munsch, M., Fontana, Y., Russo-Averchi, E., Heiss, M., Fontcuberta i Morral, A., Warburton, R. J. and Poggio, M. Quantum dot opto-mechanics in a fully self-assembled nanowire. *Nano Letters* **14**, 4454–4460 (2014).

[35] Wilson-Rae, I., Zoller, P. and Imamoḡlu, A. Laser cooling of a nanomechanical resonator mode to its quantum ground state. *Physical Review Letters* **92**, 075507 (2004).

[36] Heiss, M., Fontana, Y., Gustafsson, A., Wüst, G., Magen, C., O'Regan, D. D., Luo, J. W., Ketterer, B., Conesa-Boj, S., Kuhlmann, A. V., Houel, J., Russo-Averchi, E., Morante, J. R., Cantoni, M., Marzari, N., Arbiol, J., Zunger, A., Warburton, R. J. and Fontcuberta i Morral, A. Self-assembled quantum dots in a nanowire system for quantum photonics. *Nature Materials* **12**, 439–444 (2013).

[37] Treutlein, P., Genes, C., Hammerer, K., Poggio, M. and Rabl, P. Hybrid mechanical systems. In Aspelmeyer, M., Kippenberg, T. J. and Marquardt, F. (eds.) *Cavity Optomechanics*, Quantum Science and Technology, 327–351 (Springer Berlin Heidelberg, 2014). http://link.springer.com/chapter/10.1007/978-3-642-55312-7_14.

[38] Han, S. M., Benaroya, H. and Wei, T. Dynamics of transversely vibrating beams using four engineering theories. *Journal of Sound and Vibration* **225**, 935–988 (1999).

[39] Truesdell, C. A. *The rational mechanics of flexible or elastic bodies: 1638-1788. Introduction to: Leonhardi Euleri opera omnia vol. X et XI seriei secundae* (Venditioni exponunt Orell Füssli, Turici, Zürich, 1960).

[40] Cleland, A. N. *Foundations of nanomechanics* (Springer-Verlag, 2003).

[41] Hauer, B. D., Doolin, C., Beach, K. S. D. and Davis, J. P. A general procedure for thermomechanical calibration of nano/micro-mechanical resonators. *Annals of Physics* **339**, 181–207 (2013).

[42] Wikipedia. Cauchy stress tensor – Wikipedia, the free encyclopedia (2014). http://en.wikipedia.org/wiki/Cauchy_stress_tensor.

[43] Gercek, H. Poisson's ratio values for rocks. *International Journal of Rock Mechanics and Mining Sciences* **44**, 1–13 (2007).

[44] Signorello, G. *Uniaxial Stress Effects in Zincblende and Wurtzite GaAs Nanowires: an Optical Spectroscopy Study.* Ph.D. thesis, University of Basel (2013).

[45] Weber, D. P. *Dynamic Cantilever Magnetometry of Individual Ferromagnetic Nanotubes.* Ph.D. thesis, University of Basel (2014).

[46] Brantley, W. A. Calculated elastic constants for stress problems associated with semiconductor devices. *Journal of Applied Physics* **44**, 534–535 (1973).

[47] Signorello, G., Karg, S., Björk, M. T., Gotsmann, B. and Riel, H. Tuning the light emission from GaAs nanowires over 290 meV with uniaxial strain. *Nano Letters* **13**, 917–924 (2013).

[48] Fermi, E. *Thermodynamics* (Courier Dover Publications, 1956).

[49] Clausius, R. On a mechanical theorem applicable to heat. *Philosophical Magazine, Ser. 4* **40**, 122–127 (1870).

[50] Heisenberg, W. Über den anschaulichen inhalt der quantentheoretischen kinematik und mechanik. *Zeitschrift für Physik* **43**, 172–198 (1927).

[51] Drake, A. D. and Leiner, D. C. Fiberoptic interferometer for remote subangstrom vibration measurement. *Review of Scientific Instruments* **55**, 162–165 (1984).

[52] Rugar, D., Mamin, H. J., Erlandsson, R., Stern, J. E. and Terris, B. D. Force microscope using a fiberoptic displacement sensor. *Review of Scientific Instruments* **59**, 2337–2340 (1988).

[53] Rugar, D., Mamin, H. J. and Guethner, P. Improved fiberoptic interferometer for atomic force microscopy. *Applied Physics Letters* **55**, 2588–2590 (1989).

[54] Poggio, M., Jura, M. P., Degen, C. L., Topinka, M. A., Mamin, H. J., Goldhaber-Gordon, D. and Rugar, D. An off-board quantum point contact as a sensitive detector of cantilever motion. *Nature Physics* **4**, 635–638 (2008).

[55] Bruland, K. J., Garbini, J. L., Dougherty, W. M., Chao, S. H., Jensen, S. E. and Sidles, J. A. Thermal tuning of a fiber-optic interferometer for maximum sensitivity. *Review of Scientific Instruments* **70**, 3542–3544 (1999).

[56] Braakman, F. R., Cadeddu, D., Tütüncüoglu, G., Matteini, F., Rüffer, D., Fontcuberta i Morral, A. and Poggio, M. Nonlinear motion and mechanical mixing in as-grown GaAs nanowires. *arXiv:1406.5961* (2014).

[57] Weber, D. P., Rüffer, D., Buchter, A., Xue, F., Russo-Averchi, E., Huber, R., Berberich, P., Arbiol, J., Fontcuberta i Morral, A., Grundler, D. and Poggio, M. Cantilever magnetometry of individual Ni nanotubes. *Nano Letters* **12**, 6139–6144 (2012).

[58] Buchter, A., Nagel, J., Rüffer, D., Xue, F., Weber, D. P., Kieler, O. F., Weimann, T., Kohlmann, J., Zorin, A. B., Russo-Averchi, E., Huber, R., Berberich, P., Fontcuberta i Morral, A., Kemmler, M., Kleiner, R., Koelle, D., Grundler, D. and Poggio, M. Reversal mechanism of an individual Ni nanotube simultaneously studied by torque and SQUID magnetometry. *Physical Review Letters* **111**, 067202 (2013).

[59] Degen, C. L., Poggio, M., Mamin, H. J., Rettner, C. T. and Rugar, D. Nanoscale magnetic resonance imaging. *Proceedings of the National Academy of Sciences* **106**, 1313–1317 (2009).

[60] Xue, F., Peddibhotla, P., Montinaro, M., Weber, D. P. and Poggio, M. A geometry for optimizing nanoscale magnetic resonance force microscopy. *Applied Physics Letters* **98**, 163103 (2011).

[61] Herzog, B. E., Cadeddu, D., Xue, F., Peddibhotla, P. and Poggio, M. Boundary between the thermal and statistical polarization regimes in a nuclear spin ensemble. *arXiv:1406.6869* (2014).

[62] Peddibhotla, P. *Magnetic Resonance Force Microscopy: Harnessing Nuclear Spin Fluctuations*. Ph.D. thesis, University of Basel (2013).

[63] Svelto, O. *Principles of Lasers* (Springer, 2010).

[64] Bleszynski-Jayich, A. C., Shanks, W. E. and Harris, J. G. E. Noise thermometry and electron thermometry of a sample-on-cantilever system below 1Kelvin. *Applied Physics Letters* **92**, 013123 (2008).

[65] Mamin, H. J. and Rugar, D. Sub-attonewton force detection at millikelvin temperatures. *Applied Physics Letters* **79**, 3358–3360 (2001).

[66] Arcizet, O., Cohadon, P.-F., Briant, T., Pinard, M., Heidmann, A., Mackowski, J.-M., Michel, C., Pinard, L., Franais, O. and Rousseau, L. High-sensitivity optical monitoring of a micromechanical resonator with a quantum-limited optomechanical sensor. *Physical Review Letters* **97**, 133601 (2006).

[67] Caniard, T., Briant, T., Cohadon, P.-F., Pinard, M. and Heidmann, A. Ultrasensitive optical measurement of thermal and quantum noises. *Optics and Spectroscopy* **103**, 225–230 (2007).

[68] Nichol, J. M., Hemesath, E. R., Lauhon, L. J. and Budakian, R. Displacement detection of silicon nanowires by polarization-enhanced fiber-optic interferometry. *Applied Physics Letters* **93**, 193110 (2008).

[69] Knobel, R. G. and Cleland, A. N. Nanometre-scale displacement sensing using a single electron transistor. *Nature* **424**, 291–293 (2003).

[70] Naik, A., Buu, O., LaHaye, M. D., Armour, A. D., Clerk, A. A., Blencowe, M. P. and Schwab, K. C. Cooling a nanomechanical resonator with quantum back-action. *Nature* **443**, 193–196 (2006).

[71] LaHaye, M. D., Buu, O., Camarota, B. and Schwab, K. C. Approaching the quantum limit of a nanomechanical resonator. *Science* **304**, 74–77 (2004).

[72] Flowers-Jacobs, N. E., Schmidt, D. R. and Lehnert, K. W. Intrinsic noise properties of atomic point contact displacement detectors. *Physical Review Letters* **98**, 096804 (2007).

[73] van Wees, B. J., van Houten, H., Beenakker, C. W. J., Williamson, J. G., Kouwenhoven, L. P., van der Marel, D. and Foxon, C. T. Quantized conductance of point contacts in a two-dimensional electron gas. *Physical Review Letters* **60**, 848–850 (1988).

[74] Wharam, D. A., Thornton, T. J., Newbury, R., Pepper, M., Ahmed, H., Frost, J. E. F., Hasko, D. G., Peacock, D. C., Ritchie, D. A. and Jones, G. a. C. One-dimensional transport and the quantisation of the ballistic resistance. *Journal of Physics C: Solid State Physics* **21**, L209 (1988).

[75] Field, M., Smith, C. G., Pepper, M., Ritchie, D. A., Frost, J. E. F., Jones, G. A. C. and Hasko, D. G. Measurements of coulomb blockade with a noninvasive voltage probe. *Physical Review Letters* **70**, 1311–1314 (1993).

[76] Buks, E., Schuster, R., Heiblum, M., Mahalu, D. and Umansky, V. Dephasing in electron interference by a which-path detector. *Nature* **391**, 871–874 (1998).

[77] Sprinzak, D., Buks, E., Heiblum, M. and Shtrikman, H. Controlled dephasing of electrons via a phase sensitive detector. *Physical Review Letters* **84**, 5820–5823 (2000).

[78] Topinka, M. A., LeRoy, B. J., Shaw, S. E. J., Heller, E. J., Westervelt, R. M., Maranowski, K. D. and Gossard, A. C. Imaging coherent electron flow from a quantum point contact. *Science* **289**, 2323–2326 (2000).

[79] Topinka, M. A., LeRoy, B. J., Westervelt, R. M., Shaw, S. E. J., Fleischmann, R., Heller, E. J., Maranowski, K. D. and Gossard, A. C. Coherent branched flow in a two-dimensional electron gas. *Nature* **410**, 183–186 (2001).

[80] Stettenheim, J., Thalakulam, M., Pan, F., Bal, M., Ji, Z., Xue, W., Pfeiffer, L., West, K. W., Blencowe, M. P. and Rimberg, A. J. A macroscopic mechanical resonator driven by mesoscopic electrical backaction. *Nature* **466**, 86–90 (2010).

[81] Cleland, A. N., Aldridge, J. S., Driscoll, D. C. and Gossard, A. C. Nanomechanical displacement sensing using a quantum point contact. *Applied Physics Letters* **81**, 1699–1701 (2002).

[82] Vinante, A., Kirste, A., Haan, A. d., Usenko, O., Wijts, G., Jeffrey, E., Sonin, P., Bouwmeester, D. and Oosterkamp, T. H. High sensitivity SQUID-detection and feedback-cooling of an ultrasoft microcantilever. *Applied Physics Letters* **101**, 123101 (2012).

[83] Datta, S. *Electronic Transport in Mesoscopic Systems* (Cambridge University Press, 1997).

[84] van Wees, B. J., Kouwenhoven, L. P., Willems, E. M. M., Harmans, C. J. P. M., Mooij, J. E., van Houten, H., Beenakker, C. W. J., Williamson, J. G. and Foxon, C. T. Quantum ballistic and adiabatic electron transport studied with quantum point contacts. *Physical Review B* **43**, 12431–12453 (1991).

[85] Rössler, C., Baer, S., Wiljes, E. d., Ardelt, P.-L., Ihn, T., Ensslin, K., Reichl, C. and Wegscheider, W. Transport properties of clean quantum point contacts. *New Journal of Physics* **13**, 113006 (2011).

[86] Glazman, L., Lesovik, G., Khmelǹitskii, D. and Shekhter, R. Reflectionless quantum transport and fundamental ballistic-resistance steps in microscopic constrictions. *JETP Letters* **48**, 238 (1988).

[87] Glazman, L. I. and Khaetskii, A. V. Quantum conductance of a lateral microconstraint in a magnetic field. *Journal of Physics: Condensed Matter* **1**, 5005 (1989).

[88] *Nanostructured Systems* (Academic Press, 1992). Chapter 2: Quantum point contacts.

[89] Baca, A. G. and Ashby, C. I. H. *Fabrication of GaAs Devices* (IET, 2005). Chapter 6: Ohmic contacts.

[90] Cronenwett, S. *Coherence, Charging and Spin Effects in Quantum Dots and Point Contacts*. Ph.D. thesis, Stanford University (2001).

[91] Clerk, A. A., Girvin, S. M. and Stone, A. D. Quantum-limited measurement and information in mesoscopic detectors. *Physical Review B* **67**, 165324 (2003).

[92] Clerk, A. A. Quantum-limited position detection and amplification: A linear response perspective. *Physical Review B* **70**, 245306 (2004).

[93] Kozinsky, I., Postma, H. W. C., Bargatin, I. and Roukes, M. L. Tuning nonlinearity, dynamic range, and frequency of nanomechanical resonators. *Applied Physics Letters* **88**, 253101 (2006).

[94] Arcizet, O., Cohadon, P.-F., Briant, T., Pinard, M. and Heidmann, A. Radiation-pressure cooling and optomechanical instability of a micromirror. *Nature* **444**, 71–74 (2006).

[95] Nichol, J. M., Hemesath, E. R., Lauhon, L. J. and Budakian, R. Controlling the nonlinearity of silicon nanowire resonators using active feedback. *Applied Physics Letters* **95**, 123116 (2009).

[96] Valeille, A., Muraki, K. and Hirayama, Y. Highly reproducible fabrication of back-gated GaAs/AlGaAs heterostructures using AuGeNi ohmic contacts with initial Ni layer. *Applied Physics Letters* **92**, 152106–152106–3 (2008).

[97] Lin, H.-C., Senanayake, S., Cheng, K.-Y., Hong, M., Kwo, J., Yang, B. and Mannaerts, J. Optimization of AuGe-Ni-Au ohmic contacts for GaAs MOSFETs. *IEEE Transactions on Electron Devices* **50**, 880–885 (2003).

[98] Abhilash, T. S., Kumar, C. R. and Rajaram, G. Influence of nickel layer thickness on the magnetic properties and contact resistance of AuGe/Ni/Au ohmic contacts to GaAs/AlGaAs heterostructures. *Journal of Physics D: Applied Physics* **42**, 125104 (2009).

[99] Mehlin, A. *A Quantum Point Contact as Sensitive Sensor of Cantilever Motion.* Master's thesis, University of Basel (2012).

[100] Garbini, J. L., Bruland, K. J., Dougherty, W. M. and Sidles, J. A. Optimal control of force microscope cantilevers. i. controller design. *Journal of Applied Physics* **80**, 1951–1958 (1996).

[101] Bruland, K. J., Garbini, J. L., Dougherty, W. M. and Sidles, J. A. Optimal control of force microscope cantilevers. II. magnetic coupling implementation. *Journal of Applied Physics* **80**, 1959–1964 (1996).

[102] Buchler, B. C., Gray, M. B., Shaddock, D. A., Ralph, T. C. and Mc-Clelland, D. E. Suppression of classic and quantum radiation pressure noise by electro-optic feedback. *Optics Letters* **24**, 259–261 (1999).

[103] Bushev, P., Rotter, D., Wilson, A., Dubin, F., Becher, C., Eschner, J., Blatt, R., Steixner, V., Rabl, P. and Zoller, P. Feedback cooling of a single trapped ion. *Physical Review Letters* **96**, 043003 (2006).

[104] Lee, K. H., McRae, T. G., Harris, G. I., Knittel, J. and Bowen, W. P. Cooling and control of a cavity optoelectromechanical system. *Physical Review Letters* **104**, 123604 (2010).

[105] Stipe, B. C., Mamin, H. J., Stowe, T. D., Kenny, T. W. and Rugar, D. Noncontact friction and force fluctuations between closely spaced bodies. *Physical Review Letters* **87**, 096801 (2001).

[106] Horcas, I., Fernndez, R., Gmez-Rodrguez, J. M., Colchero, J., Gmez-Herrero, J. and Baro, A. M. WSXM: a software for scanning probe microscopy and a tool for nanotechnology. *Review of Scientific Instruments* **78**, 013705 (2007).

[107] Solanki, H. S., Sengupta, S., Dubey, S., Singh, V., Dhara, S., Kumar, A., Bhattacharya, A., Ramakrishnan, S., Clerk, A. A. and Deshmukh, M. M. High Q electromechanics with InAs nanowire quantum dots. *Applied Physics Letters* **99**, 213104 (2011).

[108] Fuhrer, A., Dorn, A., Lüscher, S., Heinzel, T., Ensslin, K., Wegscheider, W. and Bichler, M. Electronic properties of nanostructures defined in Ga[Al]As heterostructures by local oxidation. *Superlattices and Microstructures* **31**, 19–42 (2002).

[109] Bauer, F., Heyder, J., Schubert, E., Borowsky, D., Taubert, D., Bruog-
nolo, B., Schuh, D., Wegscheider, W., von Delft, J. and Ludwig, S. Mi-
croscopic origin of the '0.7-anomaly' in quantum point contacts. *Nature*
501, 73–78 (2013).

[110] Fischer, S. F., Apetrii, G., Kunze, U., Schuh, D. and Abstreiter, G.
Energy spectroscopy of controlled coupled quantum-wire states. *Nature
Physics* **2**, 91–96 (2006).

[111] Hof, K.-D., Kaiser, F. J., Stallhofer, M., Schuh, D., Wegscheider, W.,
Hanggi, P., Kohler, S., Kotthaus, J. P. and Holleitner, A. W. Spatially
resolved ballistic optoelectronic transport measured by quantized pho-
tocurrent spectroscopy. *Nano Letters* **10**, 3836–3840 (2010).

[112] Pfund, A., Shorubalko, I., Leturcq, R. and Ensslin, K. Top-gate defined
double quantum dots in InAs nanowires. *Applied Physics Letters* **89**,
252106 (2006).

[113] Larsson, M. *Electron Transport in Quantum Dots Defined in Low-
dimensional Semiconductor Structures*. Ph.D. thesis, Lund University
(2011).

[114] Solanki, H. S. *Semiconducting Nanowire Electromechanics*. Ph.D. the-
sis, Tata Institute of Fundamental Research (2011).

[115] Fontana, Y., Corfdir, P., Van Hattem, B., Russo-Averchi, E., Heiss, M.,
Sonderegger, S., Magen, C., Arbiol, J., Phillips, R. T. and Fontcuberta i
Morral, A. Exciton footprint of self-assembled AlGaAs quantum dots
in core-shell nanowires. *arXiv:1406.0163* (2014).

[116] Weiß, M., Kinzel, J. B., Schülein, F. J. R., Heigl, M., Rudolph, D.,
Morkötter, S., Döblinger, M., Bichler, M., Abstreiter, G., Finley, J. J.,
Koblmüller, G., Wixforth, A. and Krenner, H. J. Dynamic acoustic
control of individual optically active quantum dot-like emission centers
in heterostructure nanowires. *Nano Letters* **14**, 2256–2264 (2014).

[117] Uccelli, E., Arbiol, J., Magen, C., Krogstrup, P., Russo-Averchi, E.,
Heiss, M., Mugny, G., Morier-Genoud, F., Nygård, J., Morante, J. R.
and Fontcuberta i Morral, A. Three-dimensional multiple-order twin-
ning of self-catalyzed GaAs nanowires on si substrates. *Nano Letters*
11, 3827–3832 (2011).

[118] Russo-Averchi, E., Heiss, M., Michelet, L., Krogstrup, P., Nygård, J.,
Magen, C., Morante, J. R., Uccelli, E., Arbiol, J. and Fontcuberta i

Morral, A. Suppression of three dimensional twinning for a 100% yield of vertical GaAs nanowires on silicon. *Nanoscale* **4**, 1486–1490 (2012).

[119] Heigoldt, M., Arbiol, J., Spirkoska, D., Rebled, J. M., Conesa-Boj, S., Abstreiter, G., Peiró, F., Morante, J. R. and Fontcuberta i Morral, A. Long range epitaxial growth of prismatic heterostructures on the facets of catalyst-free GaAs nanowires. *Journal of Material Chemistry* **19**, 840 (2009).

[120] Högele, A., Seidl, S., Kroner, M., Karrai, K., Schulhauser, C., Sqalli, O., Scrimgeour, J. and Warburton, R. J. Fiber-based confocal microscope for cryogenic spectroscopy. *Review of Scientific Instruments* **79**, 023709 (2008).

[121] Bryant, G. W., Zieliński, M., Malkova, N., Sims, J., Jaskólski, W. and Aizpurua, J. Controlling the optics of quantum dots with nanomechanical strain. *Physical Review B* **84**, 235412 (2011).

[122] Jöns, K. D., Hafenbrak, R., Singh, R., Ding, F., Plumhof, J. D., Rastelli, A., Schmidt, O. G., Bester, G. and Michler, P. Dependence of the redshifted and blueshifted photoluminescence spectra of single $In_xGa_{1-x}As$/GaAs quantum dots on the applied uniaxial stress. *Physical Review Letters* **107**, 217402 (2011).

[123] Chandrasekhar, M. and Pollak, F. H. Effects of uniaxial stress on the electroreflectance spectrum of ge and GaAs. *Physical Review B* **15**, 2127–2144 (1977).

[124] Van de Walle, C. G. Band lineups and deformation potentials in the model-solid theory. *Physical Review B* **39**, 1871–1883 (1989).

[125] McFarlane, J., Dalgarno, P. A., Gerardot, B. D., Hadfield, R. H., Warburton, R. J., Karrai, K., Badolato, A. and Petroff, P. M. Gigahertz bandwidth electrical control over a dark exciton-based memory bit in a single quantum dot. *Applied Physics Letters* **94**, 093113 (2009).

[126] Bar-Gill, N., Pham, L. M., Jarmola, A., Budker, D. and Walsworth, R. L. Solid-state electronic spin coherence time approaching one second. *Nature Communications* **4**, 1743 (2013).

[127] Houel, J., Prechtel, J. H., Kuhlmann, A. V., Brunner, D., Kuklewicz, C. E., Gerardot, B. D., Stoltz, N. G., Petroff, P. M. and Warburton, R. J. High resolution coherent population trapping on a single hole spin in a semiconductor quantum dot. *Physical Review Letters* **112**, 107401 (2014).

[128] Kuhlmann, A. V., Houel, J., Ludwig, A., Greuter, L., Reuter, D., Wieck, A. D., Poggio, M. and Warburton, R. J. Charge noise and spin noise in a semiconductor quantum device. *Nature Physics* **9**, 570–575 (2013).

[129] Clerk, A. A., Marquardt, F. and Jacobs, K. Back-action evasion and squeezing of a mechanical resonator using a cavity detector. *New Journal of Physics* **10**, 095010 (2008).

[130] Hammerer, K., Aspelmeyer, M., Polzik, E. S. and Zoller, P. Establishing einstein-poldosky-rosen channels between nanomechanics and atomic ensembles. *Physical Review Letters* **102**, 020501 (2009).

[131] Rast, S., Gysin, U., Ruff, P., Gerber, C., Meyer, E. and Lee, D. W. Force microscopy experiments with ultrasensitive cantilevers. *Nanotechnology* **17**, S189 (2006).

[132] Restrepo, J., Ciuti, C. and Favero, I. Single-polariton optomechanics. *Physical Review Letters* **112**, 013601 (2014).

[133] Kyriienko, O., Liew, T. and Shelykh, I. Optomechanics with cavity polaritons: Dissipative coupling and unconventional bistability. *Physical Review Letters* **112**, 076402 (2014).

[134] Dantan, A., Nair, B., Pupillo, G. and Genes, C. Hybrid cavity mechanics with doped systems. *arXiv:1406.7100* (2014).

[135] Bariani, F., Singh, S., Buchmann, L. F., Vengalattore, M. and Meystre, P. Hybrid optomechanical cooling by atomic λ systems. *arXiv:1407.1073* (2014).

[136] Haroche, S. and Raimond, J. M. *Exploring the Quantum: Atoms, Cavities, and Photons* (Oxford University Press, Oxford, New York, 2006).

[137] Favero, I., Stapfner, S., Hunger, D., Paulitschke, P., Reichel, J., Lorenz, H., Weig, E. M. and Karrai, K. Fluctuating nanomechanical system in a high finesse optical microcavity. *Optics Express* **17**, 12813–12820 (2009).

[138] Flowers-Jacobs, N. E., Hoch, S. W., Sankey, J. C., Kashkanova, A., Jayich, A. M., Deutsch, C., Reichel, J. and Harris, J. G. E. Fiber-cavity-based optomechanical device. *Applied Physics Letters* **101**, 221109 (2012).

[139] Carr, D. W. and Craighead, H. G. Fabrication of nanoelectromechanical systems in single crystal silicon using silicon on insulator substrates and electron beam lithography. *Journal of Vacuum Science & Technology B* **15**, 2760–2763 (1997).

[140] Belov, M., Quitoriano, N. J., Sharma, S., Hiebert, W. K., Kamins, T. I. and Evoy, S. Mechanical resonance of clamped silicon nanowires measured by optical interferometry. *Journal of Applied Physics* **103**, 074304 (2008).

[141] Treacy, M. M. J., Ebbesen, T. W. and Gibson, J. M. Exceptionally high young's modulus observed for individual carbon nanotubes. *Nature* **381**, 678–680 (1996).

[142] Montague, J. R., Dalberth, M., Gray, J. M., Seghete, D., Bertness, K. A., George, S. M., Bright, V. M., Rogers, C. T. and Sanford, N. A. Analysis of high-q, gallium nitride nanowire resonators in response to deposited thin films. *Sensors and Actuators A* **165**, 59–65 (2011).

[143] Hoch, S. W., Montague, J. R., Bright, V. M., Rogers, C. T., Bertness, K. A., Teufel, J. D. and Lehnert, K. W. Non-contact and all-electrical method for monitoring the motion of semiconducting nanowires. *Applied Physics Letters* **99**, 053101 (2011).

Curriculum Vitae

Michele Montinaro

University of Basel
Department of Physics
Klingelbergstrasse 82
CH-4056 Basel, Switzerland

m.montinaro@unibas.ch
+41 (0)61 267 37 33
https://www.linkedin.com/
in/michelemontinaro

Personal Information

Birth: 11/11/1983 in Scorrano (LE), Italy.
Citizenship: Italian.
Languages: Italian (native), English (business proficiency), German (B1/B2).

Experience

- May 2009 – Present.
  Research and Teaching Assistant.
  Department of Physics, University of Basel, Switzerland.
  Group of Prof. M. Poggio.
  Main Tasks: Setting up a state-of-the-art laboratory, including selecting and installing equipment, planning fabrication processes, programming control software, and assembling complex apparatuses. Cleanroom processing of mesoscopic devices; electrical, optical and mechanical characterization at cryogenic temperatures and high magnetic fields; finite elements simulations; data analysis; supervision of undergraduate students; organization of tutorials; participation in international conferences and graduate schools; preparation of manuscripts, posters and oral presentations.

- January 2008 – January 2009.
  Research Fellow.
  NEST Laboratory – Scuola Normale Superiore, Pisa, Italy.
  Group of Prof. A. Tredicucci.

Main Tasks: Design and development of a novel space-resolved spectroscopic technique in the near-field, in the THz frequency domain; FDTD simulations of the apparatus; clean-room fabrication.

Education

- May 2009 – September 2014.
  Ph.D. in Physics – 6.0/6.0 summa cum laude.
  University of Basel, Switzerland.
  Thesis: Coupling of Nanomechanical Resonators to Controllable Quantum Systems.
  Advisor: Prof. M. Poggio. *External Reviewer:* Dr. H. Riel.

- October 2005 – January 2009.
  M.Sc. in Physics – 110/110 summa cum laude.
  University of Pisa, Italy.
  Thesis: THz Differential Scanning Microscope.
  Advisors: Prof. F. Beltram, Dr. P. Pingue.
  Laboratory: NEST – Scuola Normale Superiore, Pisa, Italy.

- October 2002 – September 2005.
  B.Sc. in Physics – 110/110 summa cum laude.
  University of Pisa, Italy.
  Thesis: Cr/Au for Gating an AlGaAs/GaAs Microstructure.
  European project of a single-photon source for quantum cryptography.
  Advisors: Prof. F. Beltram, Dr. V. Piazza.
  Laboratory: NEST – Scuola Normale Superiore, Pisa, Italy.

Publications and Presentations

Publications

2014 | **Quantum dot opto-mechanics in a fully self-assembled nano-wire**
Montinaro, M., Wüst, G., Munsch, M., Fontana, Y., Russo-Averchi, E., Heiss, M., Fontcuberta i Morral, A., Warburton, R. J., and Poggio, M. *Nano Letters* **14**, 4454 (2014).

2012 | **Feedback cooling of cantilever motion using a quantum point contact transducer**
Montinaro, M., Mehlin, A., Solanki, H. S., Peddibhotla, P., Mack, S., Awschalom, D. D., and Poggio, M. *Applied Physics Letters* **101**, 133104 (2012).

2011 | **A geometry for optimizing nanoscale magnetic resonance force microscopy**
Xue, F., Peddibhotla, P., Montinaro, M., Weber, D. P., and Poggio, M. *Applied Physics Letters* **98**, 163103 (2011).

2009 | **Differential near-field scanning optical microscopy with THz quantum cascade laser sources**
Degl'Innocenti, R., Montinaro, M., Xu, J., Piazza, V., Pingue, P., Tredicucci, A., Beltram, F., Beere, H. E., Ritchie, D. A. *Optics Express* **17**, 23785 (2009). Also selected for the *Virtual Journal for Biomedical Optics* **5** (2010).

Oral Presentations

2014 | **Quantum dot opto-mechanics in a fully self-assembled nano-wire**, Condensed Matter in Paris, France.

Quantum dot opto-mechanics in a fully self-assembled nano-wire, International Conference on the Physics of Semiconductors (ICPS), Austin, USA.

Invited Talk: **Quantum dot opto-mechanics in a fully self-assembled nanowire**, NCCR-QSIT General Meeting, Arosa, Switzerland.

2013 | *Invited Talk:* **Displacement detection and feedback cooling of a nanomechanical resonator**, i-net Nano Event: "NextNanoStars", Basel, Switzerland.

2012 | *Invited Talk:* **Feedback cooling of cantilever motion using a quantum point contact transducer**, NCCR-QSIT Lunch Seminar, ETH Zürich, Switzerland.
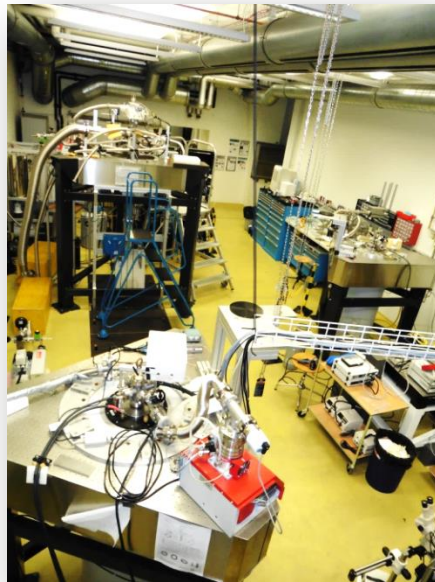
Detection of cantilever thermal motion and feedback cooling using a quantum point contact, Annual Meeting of the Swiss Physical Society, ETH Zürich, Switzerland. Proceedings on *SPS Communications* **37** (2012).

Detection of cantilever thermal motion and feedback cooling using a quantum point contact, March Meeting of the American Physical Society, Boston, USA. Proceedings on the *Bulletin of the American Physical Society* **57** (2012).

Ph.D. kick off   Ph.D. kick out